# Properties of defects and dopants in wide gap semiconductors: Theory and computations

Final Report (the third year)

Period covered: August 1st, 2005 – July 31st, 2008

# Prepared by

Professor Dr. Sukit Limpijumnong (P.I.)
Suranaree University of Technology,
Nakhon Ratchasima 30000
sukit@sut.ac.th

For the

Thailand Research Fund (TRF)
Contract # BRG4880015

# Executive summary

We have focused our attentions on wide gap oxide materials (especially ZnO) and diluted nitrides. We collaborate closely with forefront experimentalists and theorists in the USA, Europe and Asia, leading to numbers of high-quality joint publications in additional to publications that are produced solely within Thailand. We have significantly made progress in our proposed research and surpassed our original milestones in various topics. Out of a total of fifteen ISI publications, four [P1][P2][P3][P4] are in the foremost physics journal - Physical Review Letters (JIF = 7.07), and the other three [P5][P6][P7] are in the top applied physics journal – Applied Physics Letters (JIF = 3.98). Important findings that we have accomplished include: a) in collaboration with Prof. Van de Walle's group at UC Santa Barbara, we found the novel model of Si-N complex in GaAs in the form of split-interstitial which is different from what have been previously proposed by other computations. b) In collaboration with Prof. Min Zhou and his students at Georgia Tech (who perform large-scale molecular dynamics simulation) we predicts a new phases (HX and BCT-4) of ZnO nanowire under high tension.[P2][P10] c) We explain the clustering of nitrogen in some samples of GaAs:N. The fact that N in GaAs can be clustered together is puzzling because calculations found it to cause a high strain and high energy. However, we found that H, which exists everywhere during growth, makes it more preferable for N to cluster together.[P3] d) We provide theoretical support to experimentalists at US Air Force Lab. Together, we have identified Zn-interstitial to be an important donor in ZnO. Zn interstitial can strongly passivate nitrogen acceptor, impeding the progress of p-ZnO research [P4]. e) We have developed an approach to simulate the x-ray absorption near edge structures and successfully used to identify impurity defects in semiconductors and ceramics [P5][P7]. Regarding the computer hardware development, we have successfully tested and built a state-of-the-art computation server containing 4-CPU in one case.

Regarding the important outputs, we have:

- a) Published fifteen (15) ISI articles [P1]- [P15] in highly regarded international journals, including four Physical Review Letters (JIF = 7.07) and three Applied Physics Letters (JIF = 3.98).
- b) *International*:

Delivered two (3) <u>invited talks</u> at two international conferences [C1]-[C3]. Delivered three (6) <u>invited seminars</u> in USA [C4]-[C7] and China [C8][C9].

c) Domestic (Thailand):

Delivered the plenary talk at the Siam Physics Congress [C10].

Delivered four (4) invited talks at major conferences [C13]-[C16].

Delivered two (4) invited seminars/workshops [C11][C12][C17][C18].

# **Annual Research Activities**

#### **Objectives**

The goal of this program is to significantly enhance our understanding of point defects in wide gap binary semiconductors focusing on group III-V and II-VI. Throughout the program, we will, from time to time, update the tentative list of relevant defects (and material) under study to ensure timely and impact of this work as the world's interests shifted. The knowledge learning from this program will provide the foundation for increased control of impurities and defect incorporation. This is essential for improved performance of electronic and optoelectronic devices. It will also guide the experimentalists to focus only on reducing the active defects as well as explain the available experimental data. Since the topic of *p*-type dopants in ZnO is of great interest world-wide, we will also pay large attentions in investigating defects in ZnO. We believe that our shoulder-to-shoulder collaboration with leading experimentalists in the field will highly aid in the chance of success *p*-type ZnO fabrications.

#### Computational codes

We performed our studies using a first-principles calculation approach, based on density-functional theory and *ab initio* (ultrasoft) pseudopotentials. We have purchased a license to access to a popular ultrasoft pseudopotential code called VASP [R1], which is very efficient in terms of computational demands and has been tested to work very well in various systems including semiconductors and wide bandgap semiconductors. For calculations of hyperfine parameters and similar properties where the electron density near atomic cores is needed, we use the all electrons (AE) calculations based on Augmented Plane Wave method (APW) as implemented in the WIEN2k codes [R2] that is much more demanding in terms of computational resources. Most calculations were carried out on our Linux clusters, initially made possible by prior TRF Basic Research Grant funding [R3] and subsequently expanded using other source of funding. The details of the parameters and approximations used in the calculations are slightly varied depending on the specific material. Further specific computational details can be found in each attached publications.

# Novel phase of ZnO nanowire under tension

This work is based on our Wurtzite – Rocksalt phase transformation in ZnO (Ref. [R4]). While our previous work was limited to hydrostatic pressure, this work is focus on a uniaxial pressure on a finite size (nanoscale) crystal. This work is in collaboration with a mechanical engineering group at Georgia Institute of Technology (USA). Together, we predict a previously unknown phase transformation from wurtzite to a graphite-like (P63/mmc) hexagonal structure in [0110] -oriented ZnO nanowires under uniaxial tensile loading. Molecular dynamics simulations and first principles calculations show that this structure corresponds to a distinct minimum in the enthalpy surfaces of ZnO for such loading conditions. This transformation is reversible with a low level of hysteretic dissipation of 0.155 J/m3 and, along with elastic stretching, endows the nanowires with the ability to recover pseudoelastic strains up to 15%. This work is published in Physical Review Letters [P2], and more detailed results including temperature and nanowire-size dependences are published in Philosophical Magazine [P12], further details can be found in the attached manuscripts. Furthermore, we have discovered a previously unknown body-centered-tetragonal structure for ZnO. This structure results from a phase transformation from wurtzite in [0001]-oriented nanorods during uniaxial tensile loading and is the most stable phase for ZnO when stress is above 7 GPa. This stress-induced phase transformation has important implications for the electronic, piezoelectric, mechanical, and thermal responses of ZnO. A crystalline structure-load triaxiality map is developed to summarize the relationship between structure and loading. We have published this result in **Physical Review B** [P10]. Combining a graphite-like phase (HX) and a body-centered-tetragonal phase (BCT-4) transformations that were observed in [01-10]- and [0001]-oriented nanowires respectively (under uniaxial tensile loading) as well as the natural state of wurtzite (WZ) and the rocksalt (RS) phase which exists under hydrostatic pressure loading, a load triaxiality map is developed to summarize the new understanding. Equilibrium critical stress for each of the transformations is obtained and summarized in Mechanics Research Communications [P15]. We have extended the study to cover a wider variety of materials, including GaN, AlN, InN, SiC, and CdSe. This study allows us to find the tendency of transformation and the stability of the materials in the three phases (WZ, RS, and HX) as the ionicity of the material varied. The long manuscript covering all these materials is published in **Physical Review B** [P9].

# Identification of native donor (Zn-interstitial) in ZnO

This work is in collaboration with experimentalists in USA (Wright state univ. & Wright Patterson Air Force Base). While our experimental collaborators suspect that their one of their observed donors might related to  $Zn_I$ , which has been overlooked by most researchers. This is because recent calculations [R5] have found that native defects such as the O vacancy  $V_O$  and  $Z_I$  interstitial  $Z_I$  have high formation energies in n-type  $Z_I$ O and, thus, are not important donors, especially in comparison to impurities such as H. In contrast, we use both theory and experiment to show that, under N ambient, the complex  $Z_{I}$ -N<sub>O</sub> is a stronger candidate than H or any other known impurity for a 30 meV donor commonly found in bulk  $Z_I$ O grown from the vapor phase. Since the  $Z_I$  vacancy is also the dominant acceptor in such material, we must conclude that native defects are important donors and acceptors in  $Z_I$ O. This work is **published in Physical Review Letters** [P4], further details can be found in the attached manuscript.

#### Identification of impurity donors in ZnO

This work summarizes our recent success in theory-experiment collaboration with experimentalists at National Renewable Energy Lab. (USA). ZnO samples were characterized by various measurement techniques. The measured results when use in conjunction with our calculations, we together were able to identified several impurities donors in ZnO when one tries to dope it *p*-type. Based on first principles calculations, we investigate two probable types of deactivation mechanisms that hinder current efforts of doping ZnO p-type. (i) Passivation by Hydrogen. H prefers to bind with N<sub>O</sub> at the antibonding site and form N<sub>O</sub>-H complexes with a binding energy of about 1 eV. [R7] (ii) Passivation by the formation of substitutional diatomic molecules (SDM). Carbon impurities and excess N strongly prefer to passivate NO and form low-energy SDM on the Oxygen site, (NC)<sub>O</sub> or (N<sub>2</sub>)<sub>O</sub>, both of which are donors with several-eV binding

energies [R8]. Our calculated vibrational frequencies of  $N_0$ –H complexes and SDMs are consistent with the frequencies recently observed by IR measurement [R9] on N-doped ZnO, which is not p-type. This work is **published in Physica B** [P14], further details can be found in the attached manuscript.

#### Identification of Li acceptor in ZnO

An experiment on Li-doped in ZnO has been carried out at Zhejiang University (China). We provided theoretical support regarding an interpretation of their characterizations. Together, we have investigated photoluminescence from reproducible Li-doped p-type ZnO thin films prepared by dc reactive magnetron sputtering. The Li<sub>Zn</sub> acceptor state, with an energy level located at 150 meV above the valence band maximum, is identified from free-to-neutral-acceptor transitions. Another deeper acceptor state located at 250 meV emerges with the increased Li concentration. A broad emission centered at 2.96 eV is attributed to a donor-acceptor pair recombination involving zinc vacancy. In addition, two chemical bonding states of Li, evident in x-ray photoelectron spectroscopy, are probably associated with the two acceptor states observed. This work is **published in Applied Physics Letters** [P5], further details can be found in the attached manuscript.

# Hydrogen as a cause of nitrogen clustering in diluted nitride

Diluted nitrides, such as GaAs and GaP with a few percents of nitrogen, have intriguing properties. Although GaN has a larger bandgap than GaAs, adding a few percent of N to GaAs causes the GaAs bandgap to sharply reduce, not increase! This behavior has been attributed to the strain caused by large mismatch in size between N and As. If hydrogen is added to relief the strain, both lattice parameter and bandgap of GaAs:N return back to those of bulk GaAs values [R10]. First-principles calculation reveals multi-N clusters to be the ground states for hydrogenated N in dilute III-V nitrides. While hydrogenation of a single N, forming  $H_2^*(N)$ , can relax the large strain induced by the size-mismatched N, formation of the clusters will relax the strain even more effectively. This suppresses the formation of  $H_2^*(N)$ , the existence of which has recently been debated. More

importantly, postgrowth dehydrogenation of the N-H clusters provides an explanation to the observed metastable bare N clusters in GaAsN grown by gas-source molecular beam epitaxy or metal-organic chemical vapor deposition. This work is **published in Physical Review Letters** [P3], further details can be found in the attached manuscript.

# Gr IV-nitrogen complexes in diluted nitride

Because diluted nitrides of GaAs and GaP, i.e. GaAs or GaP with a few percents of nitrogen, have intriguing properties, it attracted wide attentions. Using first-principles calculations we investigate two cases of complexes between Group-IV dopant and isovalent N in this diluted nitride systems. (1) We investigated the mutual passivation of shallow donor Si and isovalent N in GaAs. Instead of the recently proposed pairing of Si and N on adjacent substitutional sites (Si<sub>Ga</sub>-N<sub>As</sub>) [R11][R12], we find that N changes the behavior of Si in dilute nitride alloys in a more dramatic way. N and Si combine into a deep-acceptor split interstitial, where Si and N share an As site [(Si-N)As], with a significantly lower formation energy than that of the Si<sub>Ga</sub>-N<sub>As</sub> pair in n-type GaAs and dilute GaAsN alloys. The formation of (Si-N)<sub>As</sub> explains the GaAs band-gap recovery and the appearance of a photoluminescence peak at ~0.8 eV. This work is **published in** Physical Review Letters [P1], further details can be found in the attached manuscript. (2) We investigated a complex between carbon and nitrogen (forming a C-N molecule) in GaAs and GaP by using first-principles density functional pseudopotential calculations. The formation energy calculations show that the molecule favors substituting for an anion site (As or P) over being an interstitial under all equilibrium growth conditions. Under ptype conditions, the molecule exhibits the characteristic triple bonding and acts as a donor. When the Fermi level is higher (n type), the molecule acts as an acceptor by accepting electrons into its antibonding states and exhibits double or single bonding. The bond length and vibrational frequencies for each configuration are calculated and compared favorably to those in recent experiments [R13]. This work is published in **Physical Review B** [P8], further details can be found in the attached manuscript.

#### Identification of arsenic complexes in ZnO

We have previously predicted that arsenic (As) and other large group V elements prefer to occupy Zn sites and forming a complex with two Zn vacancies in ZnO [R15], rather than simply substitute for O as widely believed. Recently, Vaithianathan *et al.* [R16] measured x-ray absorption near-edge structure (XANES) of As-doped ZnO and analyzed it as evidence for  $As_O$  acceptors, in contradiction to our previous prediction. However, upon carrying out first principles calculations, we found that the simulated XANES spectrum for  $As_O$  is very different from that observed (so Vaithianathan's assignment might not be correct). Instead, the simulated spectrum for  $As_{Zn}$ -2 $V_{Zn}$  defect complex, which we have previously predicted to be an acceptor, is far more consistent with the XANES data. The combination of our study, with Vaithianathan's XANES might be, until now, the strongest support for the  $As_{Zn}$ -2 $V_{Zn}$  model. This work is **published in Applied Physics Letters** [P7], further details can be found in the attached manuscript.

# Identification Mn impurity in Pb(Ti,Zr)O<sub>3</sub>

We have attempted to identify the preferred site of manganese (Mn) in  $Pb(Ti,Zr)O_3$ , *aka* PZT, ceramic. A first principles study of an Mn impurity in  $PbTiO_3$  and  $PbZrO_3$  has been carried out to determine its favorable location and its electronic and magnetic properties. We find that it is energetically favorable for the Mn atom to substitute for Ti/Zr (as opposed to substituting for Pb, O, or residing in an interstitial position) under all equilibrium crystal growth conditions. The Mn defect mainly occurs as neutral-charge Mn-substitute-Ti/Zr, which has a total electron spin of 3/2. When no other impurities are present, a small concentration of charged Mn impurities that also form tends to make the sample slightly p-type (n-type) in oxygen-rich (poor) equilibrium growth conditions. This part of the work is **published in Journal of Applied Physics** [P11], further details can be found in the attached manuscript.

To confirm the prediction (based on energetic) that Mn prefers to occupy the Ti site in PZT, we have performed the synchrotron x-ray absorption spectroscopy (XAS) experiments on Mn-doped PbZr<sub>1-x</sub>Ti<sub>x</sub>O<sub>3</sub> samples (PZT) and compared with calculations. The measurements can be divided into two regions, the near-edge region called "X-ray

Absorption Near Edge Structure" (XANES) and the higher energy region called "Extended X-Ray Absorption Fine Structure" (EXAFS). For the EXAFS region, it is found that the Fourier transforms of EXAFS structures from several samples are similar and agree well with the model of Mn substituting on the Ti/Zr site (i.e. the B site of the perovskite ABO<sub>3</sub> structure). It confirms that Mn predominantly substituted for Ti/Zr in the range of Mn concentration under study which is 0.2 - 2.0 Mol%. This work is published in Ceramic Internationals [P13], further details can be found in the attached manuscript. For the XANES region, first principles XANES simulations are carried out. The features of the measured Mn K-edge XANES are consistent with the first principles XANES of Mn on the Ti/Zr site and inconsistent with Mn on other sites. The clear agreement between measured and first-principles-theoretical XANES spectra reported here is by far the strongest evidence of Mn substituting for Ti/Zr in PZT. This work illustrates that a first-principles-supercell framework, which is popularly used to study impurities in crystals, can be used in conjunction with XANES measurement in order to identify an impurity structure with a high degree of confidence. This approach may thus be broadly applicable to study impurities in other crystals. This work is published in **Applied Physics Letters** [P5], further details can be found in the attached manuscript.

# References

- [R1] http://cms.mpi.univie.ac.at/vasp/
- [R2] http://www.wien2k.at/
- [R3] Basic Research Grant #4680003
- [R4] S. Limpijumnong and S. Jungthawan, Phys. Rev. B 70, 054104 (2004).
- [R5] A.F. Kohan *et al.*, Phys. Rev. B **61**, 15019 (2000)
- [R6] F. Oba et al., J. Appl. Phys. 90, 824 (2001).
- [R7] X. Li et al., Appl. Phys. Lett. 86, 122107 (2005).
- [R8] S. Limpijumnong, X. Li, S.-H. Wei, and S.B. Zhang, Appl. Phys. Lett. **86**, 211910 (2005).
- [R9] B.M. Keyes, L.M. Gedvilas, X. Li, T.J. Coutts, J. Cryst. Growth 281, 297 (2005).
- [R10] M.-H. Du, S. Limpijumnong, and S.B. Zhang, Phys. Rev. B 72, 073202 (2000).
- [R11] K. M. Yu et al., Nat. Mater. 1, 185 (2002).
- [R12] J. Li et al., Phys. Rev. Lett. 96, 035505 (2006).
- [R13] W. Ulrici and B. Clerjaud, Phys. Rev. B 72, 045203 (2005).
- [R14] G. Chen, I. Miotkowski, S. Rodriguez, and A.K. Ramdas, Phys. Rev. Lett. **96**, 035508 (2006).
- [R15] S. Limpijumnong, S.B. Zhang, S-H. Wei, and C. H. Park, Phys. Rev. Lett. **92**, 155504 (2004).
- [R16] V. Vaithianathan, B-T. Lee, C-H. Chang, K. Asokan, and S.S. Kim, Appl. Phys. Lett. **88**, 112103 (2006).

# Related Activities: (">" highlights the important activities)

# <u>Publications</u> (attached)

- [P1] A. Janotti, <u>P. Reunchan, S. Limpijumnong</u>, and C. G. Van de Walle "Mutual Passivation of Electrically Active and Isovalent Impurities in Dilute Nitrides"
  - Physical Review Letters 100, 045505 (2008). [Journal Impact Factor = 7.07].
- [P2] A.J. Kulkarni, M. Zhou, <u>Kanoknan Sarasamak and Sukit Limpijumnong</u>
   "Novel phase transformation in ZnO nanowires under tensile loading"
   Physical Review Letters 97, 105502 (2006). [JIF = 7.07].
- [P3] M.-H. Du, <u>Sukit Limpijumnong</u>, and S. B. Zhang
   "Hydrogen-Mediated Nitrogen Clustering in Dilute III-V Nitrides"
   ▶ Physical Review Letters 97, 075503 (2006) [JIF = 7.07].
- [P4] D.C. Look, G.C. Farlow, <u>P. Reunchan, S. Limpijumnong</u>, S.B. Zhang, and K. Nordlund "Evidence for Native-Defect Donors in n-Type ZnO"
  - ► Physical Review Letters 95, 225502 (2005) [JIF = 7.07].
- [P5] <u>Sukit Limpijumnong</u>, S. Rujirawat, A. Boonchun, M.F. Smith, and B. Cherdhirunkorn "Identification of Mn site in Pb(Zr,Ti)O<sub>3</sub> by synchrotron x-ray absorption nearedge structure: Theory and Experiment"
  - ► Applied Physics Letters 90, 103113 (2007) [JIF = 3.98].
- [P6] Y.J. Zeng, Z.Z. Ye, J.G. Lu, W.Z. Xu, L.P. Zhu, B.H. Zhao, and <u>Sukit Limpijumnong</u> "Identification of acceptor states in Li-doped p-type ZnO thin films"
  - ► Applied Physics Letters 89, 042106 (2006) [JIF = 3.98].
- [P7] <u>Sukit Limpijumnong</u>, M.F. Smith, and S. B. Zhang "Characterization of As-doped, p-type ZnO by x-ray absorption near-edge structure spectroscopy: Theory"
  - ► <u>Applied Physics Letters</u> 89, 222113 (2006) [JIF = 3.98].
- [P8] Sukit Limpijumnong, P. Reunchan, A. Janotti, and C. G. Van de Walle "Carbon-nitrogen molecules in GaAs and GaP"
  Physical Review B 77, 195209 (2008). [JIF = 3.11].

- [P9] K. Sarasamak, A. J. Kulkarni, M. Zhou, and <u>S. Limpijumnong</u> "Stability of wurtzite, unbuckled wurtzite, and rocksalt phases of SiC, GaN, InN, ZnO, and CdSe under loading of different triaxialities"
  <u>Physical Review B</u> 77, 024104 (2008). [JIF = 3.11].
- [P10] J. Wang, A.J. Kulkarni, <u>K. Sarasamak, S. Limpijumnong</u>, F.J. Ke, and M. Zhou "Molecular dynamics and density functional studies of a body-centered-tetragonal polymorph of ZnO"

**Physical Review B** 76, 172103 (2007). [JIF = 3.11].

- [P11] A. Boonchun, M.F. Smith, B. Cherdhirunkorn, and <u>Sukit Limpijumnong</u> "First principles study of Mn impurities in PbTiO<sub>3</sub> and PbZrO<sub>3</sub>" **Journal of Applied Physics 101**, 043521 (2007) [**JIF = 2.32**].
- [P12] A.J. Kulkarni, K. Sarasamak, <u>Sukit Limpijumnong</u>, and M. Zhou "Characterization of novel pseudoelastic behavior of zinc oxide nanowires" <u>Philosophical Magazine</u> 87, 2117 (2007) [JIF = 1.35].
- [P13] <u>B. Cherdhirunkorn, M.F. Smith, S. Limpijumnong, and D.A. Hall</u>
  "EXAFS study on the site preference of Mn in perovskite structure of PZT ceramics"

  <u>Ceramic Internationals</u> 34, 727 (2008). [JIF = 1.13].
- [P14] <u>Sukit Limpijumnong</u>, X. Li, S.-H. Wei, and S.B. Zhang "Probing deactivations in Nitrogen doped ZnO by vibrational signatures: A first principles study" **Physica B 376-377**, 686 (2006) [JIF = **0.87**].
- [P15] A.J. Kulkarni, K. Sarasamak, J. Wang, F.J. Ke, S. Limpijumnong, M. Zhou "Effect of load triaxiality on polymorphic transitions in zinc oxide"

  Mechanics Research Communications 35, 73 (2008). [JIF = 0.79].]

#### Presentations

#### International

- [C1] Sukit Limpijumnong presented an Invited Talk on "Probing microscopic impurity defect configurations from synchrotron x-ray absorption near edge structures" at the International Conference on Materials for Advanced Technologies (ICMAT 2007); Symp. O, Suntec, Singapore (July 1-6, 2007).
- [C2] Sukit Limpijumnong presented an Invited Talk on "Hydrogen in dilute nitrides: theory" at the Gordon Research Conference 2006: Defects in Semiconductors, Colby-Sawyer College, New London, New Hampshire, USA (July 2-7, 2006), and co-authoring another poster

Sukit Limpijumnong, M.F. Smith, S.-H. Wei, and <u>S.B. Zhang</u> on "*Recent Theory of Impurities and Defects in Zinc Oxide*".

- [C3] Sukit Limpijumnong presented an Invited Talk on "First principles study of defects in ZnO" at the 8<sup>th</sup> Asian Workshop on First-principles Electronics Structure Calculations (AWFESC) 2005, Fudan University, Shanghai, China (Oct 31 Nov. 2, 2005)
- [C4] <u>Sukit Limpijumnong</u> presented an **invited colloquia** at the **Bourns College of Engineering, UC Riverside, CA, USA**, entitled "First Principles Study Of Defects In ZnO" (Nov 20, 2006).
- [C5] <u>Sukit Limpijumnong</u> presented an **invited seminar** at the **Nitride Seminar Serie**, **Material Department**, UC **Santa Barbara**, CA, USA, entitled "Hydrogen in III-nitride and diluted nitride: First principles calculations" (Oct 5, 2006).
- [C6] <u>Sukit Limpijumnong</u> presented an **invited joint Materials Council/Structural Mechanics Seminar** at **Georgia Institute of Technology, Atlanta, GA, USA**, entitled: "First principles study of defects in ZnO" (April 12, 2006).
- [C7] <u>Sukit Limpijumnong</u> presented a talk at the ZnO Workshop, National Renewable Energy Lab., Golden, CO, USA, entitled: "Identification of the deactivated nitrogen in ZnO by vibrational frequencies" (October 12, 2005).
- [C8] <u>Sukit Limpijumnong</u> presented an **invited seminar at the Laboratory of New-Structured Materials, Zhejiang University, Hangzhou, China**, entitled: "Ab-

- initio calculations of the wurtzite-to-rocksalt homogeneous transformation in ZnO" (November 3, 2005).
- [C9] <u>Sukit Limpijumnong</u> presented an **invited seminar at the Dept. of Materials Science & Engineering, Zhejiang University, Hangzhou, China**, entitled:

  "First principles study of defects in ZnO" (November 4, 2005).

Domestic (Thailand)

- [C10] Sukit Limpijumnong presented the Plenary Talk on "Verifying defect structures by first principles calculations" at the Siam Physics Congress [SPC 2007] (Mar 22 –24, 2007).
- [C11] <u>Sukit Limpijumnong</u> presented an <u>Invited Talk</u> on "Computational condensed matter physics at the nanoscale: Defect structures and nanowires" at the NSTDA Annual Conference [NAC 2007] (Mar 29-30, 2007).
- [C12] <u>Sukit Limpijumnong</u> presented an <u>Invited Talk</u> on "Deciphering the structures of defects by matching first principles results with experiments" at the Workshop on *Ab-initio* Simulation of Nanostructures by NECTEC (June 4-6, 2007).
- [C13] Sukit Limpijumnong presented an Invited Talk on "Detecting deactivated N in ZnO by vibrational signatures" at the STT 31 (Oct 18 –20, 2005)
- [C14] Sukit Limpijumnong presented an Invited Talk on "Computational Physics: First principles study of solids" at the Siam Physics Congress [SPC 2006] (Mar 23 –25, 2006)
- [C15] ► Sukit Limpijumnong presented an Invited Talk on "First principles study of defects in ZnO" at the RGJ-Ph.D. Congress VII (Apr. 20 –22, 2006)
- [C16] Sukit Limpijumnong presented an Invited Talk on "Local structures of impurity defects from XANES" at the CHE-USDC Congress I (Sept. 5 7, 2008)
- [C17] <u>Sukit Limpijumnong</u> presented an invited talk on "*Detecting deactivated Nitrogen in ZnO by vibrational signatures*" at the 2<sup>nd</sup> Siam photon science camp (Oct 24 28, 2005).
- [C18] <u>Sukit Limpijumnong</u> presented an invited seminar at the Department of Physics, Chiangmai Univ. (Jan. 27, 2006) "First principles study of defects in ZnO".

#### **Collaborations**

#### International

- 1. Drs. S.B. Zhang, S-H. Wei and K. Kim (theory), *National Renewable Energy Lab.*, *Golden, CO, USA*.
- 2. Prof. Dr. W.R.L. Lambrecht (theory), Case Western Reserve Univ., OH, USA.
- 3. Prof. Dr. C.G. Van de Walle (theory), UC Santa Barbara, CA, USA.
- 4. Prof. Dr. Weimin Chen (experiment), Linköpin University, Sweden.
- 5. Drs. X. Li and C. Perkins (experiment), *National Renewable Energy Lab.*, *Golden, CO, USA*.
- 6. Drs. Cole Litton and David C. Look (experiment), Wright-Patterson Air Force Base, Dayton, Ohio, USA
- 7. Prof. Dr. Matthew D. McCluskey (experiment), Department of Physics and Institute for Shock Physics, Washington State University, Pullman, WA, USA
- 8. Prof. Dr. Zhizhen Ye and Prof. Dr. JianZhong Jiang (experiment), *Zhejiang University, Zhejiang University, Hangzhou, P.R. China*
- 9. Prof. Dr. Min Zhou (theory), *The Woodruff School of Mechanical Engineering, Georgia Institute of Technology, Atlanta, GA, USA*

#### Domestic (Thailand)

- 10. Assoc. Prof. Dr. Sanong Ekgasit, Chula, Bangkok, Thailand.
- 11. Dr. Rungnapa Tongpool, MTEC, Bangkok, Thailand.
- 12. Dr. Benya Cherdhirunkorn, Thamasart U., Bangkok, Thailand.

# Honors/Awards during the period of the program

- Sukit Limpijumnong is promoted to the rank of "Full Professor" at Suranaree University of Technology.
- Sukit Limpijumnong is appointed as "<u>TWAS Young Affiliate for 2007-2012</u>"
   from the Third Word Academy of Science (TWAS) Regional Office for East and South-East Asia, Beijing, China
- Sukit Limpijumnong is appointed as "<u>APCTP General Council Member for</u> <u>2008-2010</u>" from the Asia Pacific Center for Theoretical Physics (APCTP), POSTECH, Pohang, South Korea
- Sukit Limpijumnong is awarded "2004 TWAS Prize for Young Scientists in <u>Thailand</u>" from the Third Word Academy of Science (TWAS) and the National Research Council of Thailand (NRCT)
- Sukit Limpijumnong is awarded "2005 Thailand Young Scientist Award" from the Foundation for the Promotion of Science and Technology under the Patronage of His Majesty the King
- Sukit Limpijumnong is awarded "<u>2005 Corbett Prize for Young Scientists</u>" from the 23<sup>rd</sup> International Conf. of Defects in Semiconductors (ICDS-23)
- Sukit Limpijumnong is awarded "2006 SUT Outstanding Researcher Award"
   from Suranaree University of Technology (SUT)
- Sukit Limpijumnong and Sirichok Jungthawan are awarded "2005 NRCT <u>Research Award</u>" in mathematics and physical science from the National Research Council of Thailand (NRCT)
- o Invited Speaker at International conference/Workshop:
  - The International Conference on Materials for Advanced Technologies, ICMAT 2007 (Singapore)
  - The 8<sup>th</sup> Asian Workshop on First-principles Electronics Structure Calculations 2005 (China)
  - The Gordon Research Conference 2006: Defects in semiconductors (USA)

# Appendix

(Publications in ISI journals)

# Mutual Passivation of Electrically Active and Isovalent Impurities in Dilute Nitrides

A. Janotti, P. Reunchan, 2 S. Limpijumnong, 2 and C. G. Van de Walle

<sup>1</sup>Materials Department, University of California, Santa Barbara, California 93106-5050, USA
<sup>2</sup>School of Physics, Suranaree University of Technology and National Synchrotron Research Center, Nakhon Ratchasima, Thailand (Received 24 July 2007; published 30 January 2008)

Using first-principles calculations we investigate the mutual passivation of shallow donor Si and isovalent N in dilute GaAsN alloys. Instead of the recently proposed pairing of Si and N on adjacent substitutional sites ( $Si_{Ga}$ - $N_{As}$ ) [K. M. Yu *et al.*, Nat. Mater. 1, 185 (2002); J. Li *et al.*, Phys. Rev. Lett. 96, 035505 (2006)] we find that N changes the behavior of Si in dilute nitride alloys in a more dramatic way. N and Si combine into a deep-acceptor split interstitial, where Si and N share an As site [(Si-N)<sub>As</sub>], with a significantly lower formation energy than that of the  $Si_{Ga}$ - $N_{As}$  pair in *n*-type GaAs and dilute GaAsN alloys. The formation of (Si-N)<sub>As</sub> explains the GaAs band-gap recovery and the appearance of a photoluminescence peak at  $\sim$ 0.8 eV. This model can also be extended to Ge-doped GaAsN alloys, and correctly predicts the absence of mutual passivation in the case of column-VI dopants.

DOI: 10.1103/PhysRevLett.100.045505

PACS numbers: 61.72.-y, 71.55.Eq

Alloys of highly mismatched semiconductors offer unique opportunities for band-structure engineering. For example, when a small fraction of As atoms in GaAs is replaced by N to form GaAsN alloys, the band gap changes rapidly with increasing N concentration, decreasing by as much as 180 meV per atomic percent of N [1–4]. This behavior is markedly different from that of conventional alloys [5]: one would expect the band gap of  $GaAs_{1-x}N_x$  to *increase* from its value in GaAs (1.5 eV) towards its value in GaN (3.4 eV) as the N content increases. This unusual behavior is of interest not only from a fundamental perspective, but also because of its significant potential in device applications [6].

As for any semiconductor, doping is essential for controlling the electrical conductivity in  $GaAs_{1-x}N_x$  alloys. While the physics of n-type and p-type doping in the parent compounds GaAs and GaN is well established, doping in GaAs<sub>1-x</sub>N<sub>x</sub> is much less explored. Recent reports indicate that the interaction between extrinsic dopants and N in GaAs<sub>1-x</sub>N<sub>x</sub> alloys can lead to entirely new phenomena [7-10]. Yu et al. [7] reported that when  $GaAs_{1-x}N_x$  is doped with Si, the interaction between Si and N leads to a "mutual passivation," characterized by an increase in the band gap and an elimination of the electrical activity of the Si donor. It was observed that rapid thermal annealing of Si-doped dilute (In)GaAsN alloys at temperatures above 800 °C leads to a drastic increase in the electrical resistivity, accompanied by an increase in the band gap up to a value corresponding to the net "active" N, roughly equal to the total N concentration minus the Si concentration [7–9]. Simultaneously, a peak at  $\sim 0.8$  eV appeared in the photoluminescence spectra [7,8]. Similar effects were observed for Ge-doped, but not for S- or Sedoped  $GaAs_{1-x}N_x$  [9]. It was postulated that substitutional  $Si_{Ga}$  and  $Ge_{Ga}$  form strong bonds with  $N_{As}$  and lead to deep donor levels, eliminating the shallow-donor character of Si and Ge in  $GaAs_{1-r}N_r$  alloys. On the other hand,  $S_{As}$  and Se<sub>As</sub> are (at best) second-nearest neighbors of N<sub>As</sub> and not

directly bonded to  $N_{As}$ ; therefore they would not suffer from the passivation effect [7–9].

First-principles calculations by Li et al. suggested that the Si<sub>Ga</sub>-N<sub>As</sub> complex [Fig. 1(a)] indeed induces a deep donor level in the band gap [11]; it was predicted that in the impurity limit this state would be located at 0.23 eV below the GaAs conduction-band minimum (CMB) [11]. Li et al. also reported a binding energy of 0.26 eV for the Si<sub>Ga</sub>-N<sub>As</sub> pair in the neutral charge state [11]. However, this proposed model exhibits some serious problems and discrepancies with experiment. First, a binding energy of 0.26 eV is too small to explain the formation of a high concentration of Si<sub>Ga</sub>-N<sub>As</sub> pairs at temperatures above 800 °C. At these temperatures, we estimate that less than 40% of the Si atoms would be bonded to  $N_{As}$  in  $Si_{Ga}$ - $N_{As}$  pairs. Second, as will be shown later, their binding energy of 0.26 eV is overestimated. With a corrected binding energy, the number of complexes formed would be much smaller, in contrast to the experimental results [7-9]. Finally, the Si<sub>Ga</sub>-N<sub>As</sub> pair does not explain the appearance of a deeplevel luminescence at  $\sim 0.8$  eV above the valence-band maximum (VBM) as observed in the experiments of Yu et al. [7,9].

In this Letter we show that isovalent N changes the microscopic behavior of Si donors in dilute GaAsN alloys

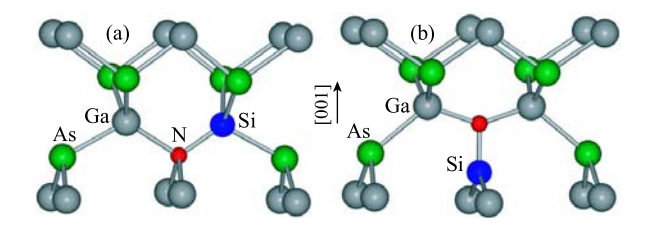


FIG. 1 (color online). Local structure of (a)  $(Si_{Ga}-N_{As})^+$  and (b)  $(Si-N)_{As}^-$ . In the  $Si_{Ga}-N_{As}$  configuration,  $Si_{Ga}$  is a nearest neighbor of  $N_{As}$ ; in the  $(Si-N)_{As}$  configuration,  $Si_{Ga}$  and N share an As site.

in a more dramatic way. Based on first-principles densityfunctional calculations we find that Si combines with N into stable (Si-N)<sub>As</sub> split interstitials that act as compensating centers in n-type GaAsN. The (Si-N)<sub>As</sub> split interstitial is a deep acceptor with a formation energy that is significantly lower than that of Si<sub>Ga</sub>-N<sub>As</sub> in n-type GaAsN. The calculated acceptor level is located at 0.89 eV above the valence-band maximum. This explains the appearance of the photoluminescence peak that accompanies the mutual passivation effect. The formation of (Si-N)<sub>As</sub> split interstitials also leads to a blueshift in the band gap by reducing the nitrogen concentration that effectively participates in the band-gap reduction in GaAsN alloys. The formation of (Si-N)<sub>As</sub> split interstitials in annealed Si-doped GaAs<sub>1-x</sub>N<sub>x</sub> therefore leads to highly resistive alloys with a band gap governed by the net active N, in full agreement with experimental results. Our results for the electronic structure and the frequency of the local vibrational mode of the Si-N split interstitial provide a guide for further experiments on mutual passivation effects in highly mismatched semiconductor alloys.

Our calculations are based on density-functional theory (DFT) within the local density approximation (LDA) and pseudopotentials as implemented in the VASP code [12-15]. We use a plane-wave basis set with a cutoff of 400 eV. GaAsN alloys with different N concentrations were simulated by supercells containing 64, 128, or 216 atoms, in which one As was replaced by one N; this corresponds to a N content of 3.1%, 1.6%, or 0.9%, respectively. Integrations over the Brillouin zone were performed using a 2 ×  $2 \times 2$  grid of Monkhorst-Pack special k points for the 64atom supercell, and  $1 \times 1 \times 1$  grids for 128- and 216-atom supercells. These calculations allow us to analyze trends with band gap in alloys with different nitrogen concentrations. In order to address the DFT-LDA underestimation of the band gap, we performed calculations with two different pseudopotentials: one in which the Ga 3d electrons are explicitly included as valence states, the other with Ga 3d electrons frozen in the core. The two situations produce very similar results for structure and energetics, but the "d in the core" potential results in a band gap that is larger by 0.15 eV.

The behavior of Si in GaAs is well established. Si predominantly occupies Ga sites and is a hydrogenic shallow donor; i.e., its extra valence electron is loosely bound and can be thermally excited to the GaAs conduction band. In GaAsN, the formation energy of  $\mathrm{Si}_{\mathrm{Ga}}^+$  is given by

$$E^{f}(Si_{Ga}^{+}) = E_{tot}(Si_{Ga}^{+}) - E_{tot}(GaAsN) - \mu_{Si} + \mu_{Ga} + E_{F},$$
(1)

where  $E_{\rm tot}({\rm Si}_{\rm Ga}^+)$  is the total energy of a GaAsN supercell with one Ga replaced by one Si atom,  $E_{\rm tot}({\rm GaAsN})$  is the total energy of GaAsN in the same supercell, and  $\mu_{\rm Si}$  and  $\mu_{\rm Ga}$  are the Si and Ga chemical potentials. For Si,  $\mu_{\rm Si}$  is simply the total energy per atom in a Si crystal,  $E_{\rm tot}({\rm Si})$ .  $\mu_{\rm Ga}$ , on the other hand, can vary from  $\mu_{\rm Ga} = E_{\rm tot}({\rm Ga})$  (the

total energy per atom in a Ga crystal) under Ga-rich conditions to  $\mu_{\rm Ga}=E_{\rm tot}({\rm Ga})+\Delta H_f({\rm GaAsN})$  (Ga-poor conditions), where  $\Delta H_f({\rm GaAsN})$  is the calculated formation enthalpy of the GaAsN alloys [16].  $E_F$  is the Fermi-level position, which is commonly referenced to the valence-band maximum. Our calculated formation energy is shown in Fig. 2.

The binding energy of  $Si_{Ga}$ - $N_{As}$  with respect to the isolated species  $Si_{Ga}$  and  $N_{As}$  is defined as

$$E_b = E^f(\operatorname{Si}_{Ga}) + E^f(\operatorname{N}_{As}) - E^f(\operatorname{Si}_{Ga}-\operatorname{N}_{As}), \qquad (2)$$

resulting in a positive  $E_b$  if the complex is lower in energy than the isolated species. If we assume both Si<sub>Ga</sub> and Si<sub>Ga</sub>-N<sub>As</sub> to be in the *positive* charge state, then the calculated binding energy is actually negative: the configuration where  $Si_{Ga}^+$  is far away from  $N_{As}$  has an energy that is lower than that of Si<sub>Ga</sub>-N<sub>As</sub> by 0.04 eV. This value differs from the result of Li et al. [11], who found a binding energy of 0.26 eV. Li et al. [11] assumed that Si<sub>Ga</sub> and Si<sub>Ga</sub>-N<sub>As</sub> would be in the neutral charge state; for the shallow donor Si<sub>Ga</sub> this implies placing an electron in a shallow level close to the conduction-band minimum (CBM). Li et al. [11] used the value of the GaAs CBM in their derivation. While it is true that for purposes of defining the binding energy Si<sub>Ga</sub> should be far from the N<sub>As</sub>, it should be clear that in an alloy such as GaAsN the CBM is shifted down throughout the material. Therefore the formation energy of  $Si_{Ga}^0$  should be determined using the GaAsN CBM, which is considerably lower than that of GaAs. If we strictly follow the procedure of Li *et al.*, we find  $E_b = 0.27$  eV, virtually identical to their value; however, if we properly reference the formation energy of the neutral charge state to the CBM of the GaAsN alloy, the calculated binding energy is lowered to 0.11 eV. This low value (along with the negative value we obtained for the binding energy of

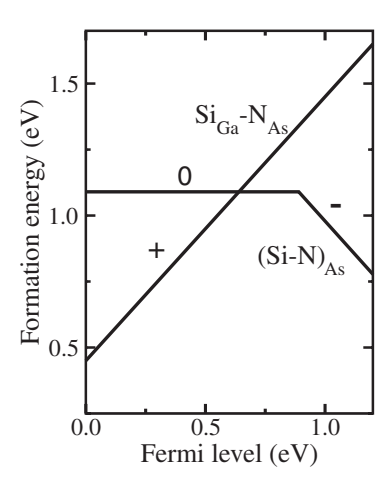


FIG. 2. Formation energy as a function of Fermi-level position for  $Si_{Ga}$ - $N_{As}$  and  $(Si-N)_{As}$  in GaAsN, under Ga-rich conditions. The Fermi level varies from 0 to 1.25 eV, which corresponds to the band gap of GaAsN alloys with a N concentration of about 1% [7].

the positive charge state) indicates that there is only a very weak driving force for  $Si_{Ga}$  and  $N_{As}$  to form  $Si_{Ga}$ - $N_{As}$  pairs. The assumption in previous work [7–9] that  $Si_{Ga}$  and  $N_{As}$  would form a bond that is significantly stronger than the  $Ga_{Ga}$ - $N_{As}$  bond is clearly unjustified.

A much more likely bonding configuration is found in our proposed  $(Si-N)_{As}$  split-interstitial complex. The formation energy of  $(Si-N)_{As}$  in charge state q is given by

$$E^{f}[(\text{Si-N})_{\text{As}}^{q}] = E_{\text{tot}}[(\text{Si-N})_{\text{As}}^{q}] - E_{\text{tot}}(\text{GaAsN}) - \mu_{\text{Si}} + qE_{F}.$$
(3)

Figure 2 shows that the split interstitial can occur in the neutral and negative charge states, with a transition level  $\varepsilon(0/-)$  at 0.89 eV above the VBM. (Si-N)<sub>As</sub> thus acts as a deep acceptor and is stable in the negative charge state for  $E_F > 0.89$  eV.

In the (Si-N)<sub>As</sub> configuration, Si and N are both threefold coordinated in planar geometries: Si is bonded to N and two Ga atoms, and N is bonded to Si and two other Ga atoms; the surrounding Ga atoms are all fourfold coordinated as shown in Fig. 1(b). In the neutral charge state the Si-N bond length is 1.65 Å. The N-Ga and Si-Ga bond lengths are 1.89 and 2.33 Å, and these Ga atoms are displaced outward from their nominal lattice sites by distances corresponding to 1.0% and 8.5% of the equilibrium Ga-As bond length. This is a small perturbation when compared to inward displacements of 16% for the Ga atoms surrounding an isolated N in GaAsN alloys, or 12% for the three Ga atoms surrounding the N in the Si<sub>Ga</sub>-N<sub>As</sub> pair. Note that we did not impose any symmetry constraints in the relaxation of the Si-N configurations.

The electronic structure of the (Si-N)<sub>As</sub> split interstitial can be understood based on electron counting: the removal of an As atom leaves four Ga dangling bonds with a total of three electrons. The (Si-N)<sub>As</sub> pair contributes nine valence electrons, leading to a combined total of 12 electrons. Eight of these are accommodated in two N-Ga and two Si-Ga bonds. Two electrons are accommodated in a Si-N  $\sigma$ bond, and we are left with two electrons. The  $p_z$  orbitals on N and Si are oriented in mutually perpendicular directions, preventing the formation of a  $\pi$  bond. However, they still combine into a doubly occupied bonding state located near the VBM, and an empty antibonding state at 0.95 eV above the VBM. Since N is more electronegative than Si, the bonding state has more nitrogen character and the antibonding state more Si character, as shown in Fig. 3. Moreover, we observe that the band gap of GaAs is restored upon formation of the (Si-N)<sub>As</sub> split interstitial. In our supercell, the next available Kohn-Sham state above the antibonding state is in the GaAs conduction band. Therefore the formation of the (Si-N)<sub>As</sub> complex removes the effect of N on the band gap, but at the expense of forming a deep level.

The antibonding state at 0.95 eV (averaged over the special k points) above the VBM can in principle accept up to two electrons, corresponding to negative (-) and

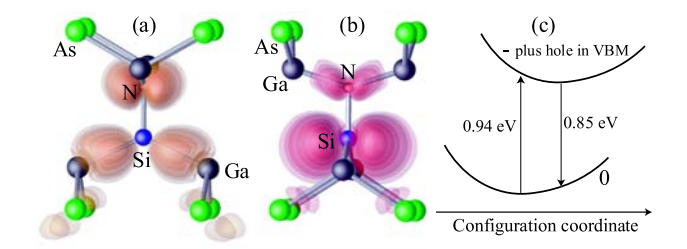


FIG. 3 (color online). Charge density isosurfaces of the (a) bonding and (b) antibonding states associated with (Si-N)<sub>As</sub>. The structure in (b) has been rotated with respect to (a) to better visualize the localization of the states. (c) Calculated configuration coordinate diagram for (Si-N)<sub>As</sub> indicating energies at which absorption and luminescence occur.

doubly negative (2-) charge states of  $(Si-N)_{As}$ . We find the  $\varepsilon(-/2-)$  transition level at 1.25 eV above the VBM, which places it above the CBM of the GaAsN alloy. In the – and 2– charge states we observe a small increase in the Si-N bond length (1.68 Å) compared to the value in the neutral configuration (1.65 Å). The Ga atoms are displaced outward from their nominal lattice sites by 0.8% and 6.8% of the equilibrium Ga-As bond length.

Figure 2 also shows that the formation energy of  $(Si-N)_{As}$  is lower than that of the  $Si_{Ga}-N_{As}$  pair for Fermi-level positions above 0.6 eV. Even under extreme Ga-poor conditions the formation energy of  $(Si-N)_{As}$  remains lower than that of  $Si_{Ga}^+-N_{As}$  when  $E_F$  is near the CBM (as is the case in the experiments [8]). In this case the formation energy of negatively charged  $(Si-N)_{As}$  is 0.4 eV lower than that of positively charged  $Si_{Ga}-N_{As}$ .  $(Si-N)_{As}$  acts as a compensating acceptor in GaAsN, and charge neutrality requires that the net electron concentration is the difference between the  $Si_{Ga}^+$  and  $(Si-N)_{As}^-$  concentrations. Since the electron concentration is much smaller than the total Si concentration after annealing at 800 °C or above [8], we conclude that the final concentrations of  $Si_{Ga}$  and  $(Si-N)_{As}^-$  must be very close.

The formation of  $(Si-N)_{As}$  split interstitials can also explain the peak at  $\sim 0.8$  eV in the photoluminescence spectra [7,9]. The exciting photons create electron-hole pairs. In the presence of holes in the valence band, negatively charged  $(Si-N)_{As}$  complexes can convert to neutral by emitting a photon at 0.85 eV, as shown in Fig. 3(c). We note that the position of this peak is essentially independent of the nitrogen concentration, and also not sensitive to the DFT-LDA underestimation of the gap, as checked by performing calculations with different pseudopotentials that produce different gaps.

Now we consider why the formation of  $(Si-N)_{As}$  in Sidoped GaAsN requires annealing at temperatures above 800 °C. Dilute GaAsN alloys are typically grown at relatively low temperatures (T < 500 °C) to prevent N segregation. Si can be introduced during this low-temperature growth or by ion implantation; either way, the resulting  $Si_{Ga}$  donors are unable to find their lowest-energy configu-

ration [in (Si-N)<sub>As</sub> complexes] during this nonequilibrium incorporation process. Annealing at temperatures above 800 °C allows Si atoms to diffuse (mediated by Ga vacancies [17]) and find their equilibrium configuration, while the N atoms are locked into the lattice since their diffusion requires much higher temperatures [18]. At 800 °C the mean free path of Si is long enough for Si atoms to encounter N atoms [7–9]. Si<sub>Ga</sub> then combines with N<sub>As</sub> into stable (Si-N)<sub>As</sub> split interstitials. This process involves the emission of a Ga vacancy, but since Ga vacancies are mobile at these temperatures their concentration will rapidly return to the equilibrium concentration.

Germanium is also an important candidate for n-type doping in dilute GaAsN alloys. We find that Ge also combines with N into stable  $(Ge-N)_{As}$  split interstitials that have lower formation energy than  $Ge_{Ga}$ - $N_{As}$  pairs. The formation of  $(Ge-N)_{As}$  also explains the mutual passivation between Ge and N in Ge-doped GaAsN alloys as observed by Wu  $et\ al.$  [8]. A detailed discussion of the results for Ge-doped GaAsN will be published elsewhere. Our results indicate that the formation of  $(Si-N)_{As}$  or  $(Ge-N)_{As}$  split interstitials is also likely to occur in other III–V based dilute nitride alloys, such as InGaAsN, GaPN, and InGaPN alloys.

In addition, our model nicely explains why column-VI dopants (such as S and Se) behave differently. In this case,  $(S-N)_{As}$  and  $(Se-N)_{As}$  split interstitials are less stable than the isolated  $S_{As}$  or  $Se_{As}$  donor configurations. The reason is that the column-VI donors have two more electrons than column-IV donors, and hence the antibonding state formed from  $p_z$  orbitals is occupied by two electrons in the  $(S-N)_{As}$  or  $(Se-N)_{As}$  split interstitial. This causes the formation energies of these complexes to be significantly higher [e.g.,  $(Se-N)_{As}$  is more than 1 eV higher in energy than isolated  $Se_{As}$ ], rendering them unstable with respect to the isolated species. Therefore S- or Se-doped GaAsN does not suffer from the mutual passivation effect.

Finally, we also calculated the local vibrational mode associated with the  $(\text{Si-N})_{As}$  split interstitial. The calculations were performed by displacing the Si and N atoms in the three Cartesian directions and diagonalizing the force-constant matrix as described in Ref. [19]. Since the masses of N and Si are much smaller than the mass of the Ga atoms, we find that considering the displacements of Si and N alone is a good approximation. The calculated frequency of the Si-N stretch mode of  $(\text{Si-N})_{As}$  is 935 cm<sup>-1</sup> in the neutral charge state and 884 cm<sup>-1</sup> in the negative charge state. These frequencies are much higher than the Si-N stretch frequency of 563 cm<sup>-1</sup> associated with the  $\text{Si-N}_{Ga}$ -N<sub>As</sub> pair. These predicted vibrational frequencies can therefore serve as a guide for experimental identifica-

tion of the Si-N complex associated with the mutual passivation effect.

This work was supported in part by the MRSEC Program of the National Science Foundation under Grant No. DMR05-20415, by the NSF IMI Program under Grant No. DMR 04-09848, and by the UCSB Solid State Lighting and Display Center. It also made use of the CNSI Computing Facility under NSF Grant No. CHE-0321368. S.L. and P.R. thank the Thailand Research Fund (Grants No. BRG4880015 and No. PHD/0203/2546) and the California NanoSystems Institute for its hospitality.

- [1] M. Weyers *et al.*, Jpn. J. Appl. Phys., Part 2 **31**, L853 (1992).
- [2] J. Neugebauer and C. G. Van de Walle, Phys. Rev. B 51, 10568 (1995).
- [3] S.-H. Wei and A. Zunger, Phys. Rev. Lett. **76**, 664 (1996).
- [4] W. Shan et al., Phys. Rev. Lett. 82, 1221 (1999).
- [5] J. C. Woolley, in *Compound Semiconductors*, edited by R. K. Willardson and H. L. Goering (Reinhold, New York, 1962), p. 3.
- [6] Special issue on III-N-V Semiconductor Alloys, edited by J. W. Ager III and W. Walukiewicz [Semicond. Sci. Technol. 17, 8 (2002)].
- [7] K. M. Yu, W. Walukiewicz, J. Wu, D.E. Mars, D.R. Chamberlin, M. A. Scarpula, O.D. Dubon, and J. F. Geisz, Nat. Mater. 1, 185 (2002).
- [8] J. Wu, K. M. Yu, W. Walukiewicz, G. He, E. E. Haller, D. E. Mars, and D. R. Chamberlin, Phys. Rev. B 68, 195202 (2003).
- [9] K. M. Yu, W. Walukiewicz, J. Wu, W. Shan, J. W. Beeman, M. A. Scarpula, O. D. Dubon, M. C. Ridgway, D. E. Mars, and D. R. Chamberlin, Appl. Phys. Lett. 83, 2844 (2003).
- [10] Y. G. Hong, A. Nishikawa, and C. W. Tu, Appl. Phys. Lett. 83, 5446 (2003).
- [11] J. Li, P. Carrier, and S.-H. Wei, S.-S. Li, and J.-B. Xia, Phys. Rev. Lett. 96, 035505 (2006).
- [12] P. Hohenberg and W. Kohn, Phys. Rev. 136, B864 (1964);
   W. Kohn and L. J. Sham, Phys. Rev. 140, A1133 (1965).
- [13] P.E. Blöchl, Phys. Rev. B 50, 17953 (1994); G. Kresse and J. Joubert, Phys. Rev. B 59, 1758 (1999).
- [14] D. Vanderbilt, Phys. Rev. B 32, 8412 (1985).
- [15] G. Kresse and J. Furthmüller, Phys. Rev. B **54**, 11169 (1996); G. Kresse and J. Furthmüller, Comput. Mater. Sci. **6**, 15 (1996).
- [16] C. G. Van de Walle and J. Neugebauer, J. Appl. Phys. 95, 3851 (2004).
- [17] A. Janotti, S.-H. Wei, S. B. Zhang, and S. Kurtz, and C. G. Van de Walle, Phys. Rev. B 67, 161201 (2003).
- [18] G. Bosker, N. A. Stolwijk, J. Thordson, U. Sodervall, and T. G. Andersson, Phys. Rev. Lett. 81, 3443 (1998).
- [19] A. Janotti, S. B. Zhang, and S.-H. Wei, Phys. Rev. Lett. 88, 125506 (2002).

# Novel Phase Transformation in ZnO Nanowires under Tensile Loading

Ambarish J. Kulkarni, Min Zhou, 1,\* Kanoknan Sarasamak, and Sukit Limpijumnong

<sup>1</sup>The George W. Woodruff School of Mechanical Engineering, Georgia Institute of Technology, Atlanta, Georgia 30332-0405, USA <sup>2</sup>School of Physics, Suranaree University of Technology and National Synchrotron Research Center, Nakhon Ratchasima, Thailand (Received 18 April 2006; revised manuscript received 18 June 2006; published 7 September 2006)

We predict a previously unknown phase transformation from wurtzite to a graphitelike  $(P6_3/mmc)$  hexagonal structure in  $[01\bar{1}0]$ -oriented ZnO nanowires under uniaxial tensile loading. Molecular dynamics simulations and first principles calculations show that this structure corresponds to a distinct minimum on the enthalpy surfaces of ZnO for such loading conditions. This transformation is reversible with a low level of hysteretic dissipation of  $0.16 \text{ J/m}^3$  and, along with elastic stretching, endows the nanowires with the ability to recover pseudoelastic strains up to 15%.

DOI: 10.1103/PhysRevLett.97.105502

The assumption of crystal structures by a material reflects a complex interplay of intrinsic factors such as composition, band structure, valence electrons, bonding states, and structural symmetry and extrinsic factors such as temperature and loading. A change in any of these factors may trigger a transformation to a different structure, giving rise to polymorphism which is especially pronounced in compounds such as ZnO whose electronic bonding states show significant dependence on applied loading [1]. There are three hitherto well-known polymorphs of ZnO, including wurtzite (WZ, P63mc space group), zinc blende (ZB,  $F\bar{4}3m$ ) and rock salt (RS,  $Fm\bar{3}m$ ) [2]. WZ is the most stable and commonly observed phase under ambient pressure. ZB can be obtained only on cubic surfaces under specific growth conditions. RS is the result of a transformation from WZ at pressures between 8-10 GPa [1,3–8]. This pressure-induced reversible transformation has received significant consideration primarily because hydrostatic compression is the most likely mode of loading for bulk ZnO. Recent work on GaN, MgO, and ZnO thin films has revealed a previously unknown unbuckled structure resulting from extensive surface reconstructions to suppress surface polarity [9-12]. So far, the existence of polymorphs other than WZ, ZB, and RS at various loading

Recent synthesis of quasi-1D nanostructures such as ZnO nanowires, nanobelts, and nanorods necessitates understanding of the response of ZnO to uniaxial tensile loading [13–15]. Since these nanostructures are single-crystalline and nearly defect-free, they are endowed with high strengths and the ability to undergo large deformations without failure. Also, their high surface-to-volume ratios enhance atomic mobility and promote phase transformations under loading along certain crystalline directions.

triaxialities has not been extensively studied.

Here, we report a novel phase transformation from WZ to an unbuckled wurtzite phase (hexagonal, hereafter denoted as HX) within the  $P6_3/mmc$  space group during uniaxial tensile loading of  $[01\bar{1}0]$ -oriented ZnO nanowires [Fig. 1(a)]. This structure bears both resemblance to and distinction from the layered structure (LY) [9-12]; see

PACS numbers: 61.50.Ks, 61.46.-w, 62.25.+g, 64.70.Nd

Fig. 1(c) which compares charge density distributions on the  $(11\bar{2}0)$  planes of WZ, HX, and LY. The resemblance is in crystallography and the distinction is in coordination. Specifically, a strong bond along the [0001] axis is seen in HX which occurs throughout the solid wires. In contrast, this interplanar bond is absent in LY, which extends only a few layers from the surface beneath which the structure is predominantly WZ. Therefore, despite the similar geomet-

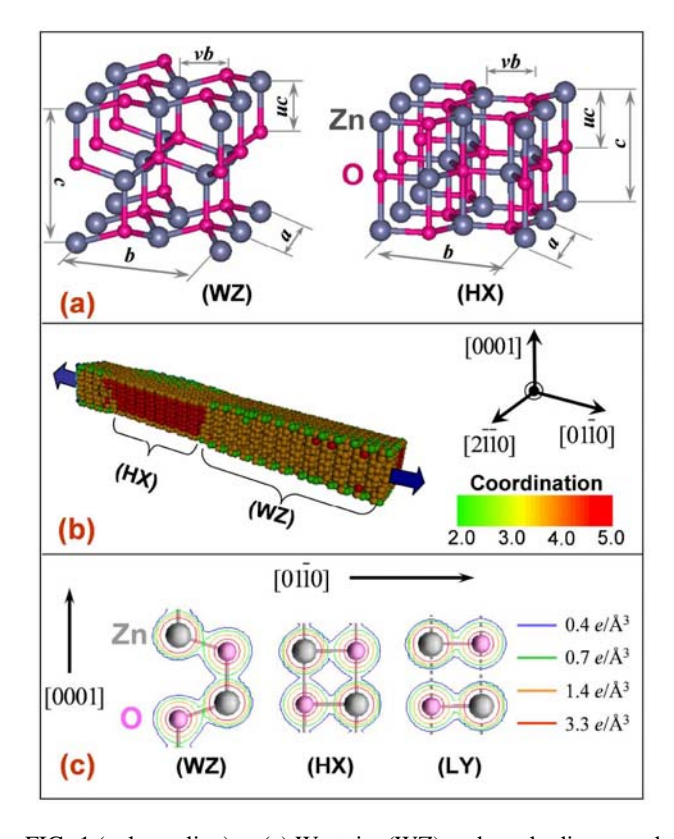


FIG. 1 (color online). (a) Wurtzite (WZ) and newly discovered hexagonal (HX) crystal structures, (b) nanowire with HX and WZ phases [transformation in progress under tensile loading (point *C* in Fig. 2 with a strain of 5.9%)]; and (c) charge density plots on the (1120) planes of WZ, HX, and the layered structure (LY) reported in Refs. [9,10].

ric symmetries, HX has a higher coordination number (5) than LY (3). A similar HX phase has been reported as the natural state of boron nitride (h-BN) [16]. It has also been predicted as a metastable state of GaN during the WZ  $\rightarrow$  RS transformation at high pressures [17] and as a stable phase of MgO under hydrostatic tensile loading [18].

The deformation analysis here uses a quasistatic loading scheme within the molecular dynamics (MD) framework ([19]) and a Buckingham potential with charge interactions [20,21]. The parameters of the potential are the same as those in Ref. [22] and have been shown to accurately predict the lattice, elastic, and dielectric constants along with surface and defect properties of ZnO [20,22,23]. The nanowire considered has an initial WZ structure with  $[01\bar{1}0]$  growth orientation and  $(21\bar{1}0)$  and (0001) lateral surfaces. The lateral dimensions are  $21.22 \times 18.95$ ,  $31.02 \times 29.42$ , or  $40.81 \times 39.89$  Å. Under applied tensile stress  $(\sigma_b)$  along the wire axis, gradual transformation into the HX phase occurs. Figure 1(b) shows a partially transformed  $21.22 \times 18.95$  Å wire containing both WZ and HX phases. To ascertain the relative energetic favorability of the two phases under loading, their enthalpies are independently determined using first principles calculations which are based on the density functional theory (DFT) as implemented in the VASP code [24], with local density approximation and ultrasoft pseudopotentials Computational parameters such as energy cutoff and sampling k points are the same as those in Ref. [7] which focused on the WZ -> RS transformation of ZnO and yielded lattice parameters, bulk modulus, and equilibrium transformation pressure that are in good agreement with experiments. For comparison, the emergence of HX as a stable phase under compressive loading  $(\sigma_c)$  along the [0001] axis is also shown.

We first characterize crystallographic changes associated with the transformation. As shown for the WZ lattice in Fig. 1(a), three parameters (a, c, and u) are typically used to define hexagonal structures, with uc denoting the offset between the Zn and O basal planes. Additional parameters b and v, with vb being the offset between Zn and O atoms along the  $[01\bar{1}0]$  axis, are introduced to

delineate the difference between the HX and RS structures [7,17]. a, b, and c are the dimensions of the hexagonal unit cell along the  $[2\overline{11}0]$ ,  $[01\overline{1}0]$ , and [0001] directions, respectively. Table I lists the lattice constants for WZ, HX, and RS structures. Note that the parameters for relaxed wires deviate slightly from the values for ideal bulk WZ due to surface effects [19,26]. For HX, c = 4.35 Å and u = 0.50 are similar to those for RS; whereas a = 3.34 Å and v = 0.32 are similar to those for WZ. Since v remains unchanged, HX has the same hexagonal symmetry around the c axis as WZ. During the transformation, u changes from its initial value of 0.38 for WZ to a value of 0.5 for HX (Table I), implying the flattening of the buckled wurtzite basal plane (Zn and O atoms becoming coplanar). As a result, Zn atoms are at equal distances from O atoms along the [0001] axis and the structure acquires the additional symmetry of a mirror plane perpendicular to the [0001] axis. This process occurs while the orientation of the basal plane remains invariant. The in-plane coordination of the HX structure is threefold and the full 3D coordination is fivefold (as compared to the fourfold in WZ). The formation of additional bonds (therefore the increase in coordination) along the [0001] axis can also be seen in the charge density distributions on (1120) planes in Fig. 1(c). Obviously, an additional bond is formed between the Zn atom initially at the top left and the O atom initially at the bottom in the WZ structure. However, the charge density map for LY observed in [9,10] does not display such a strong intraplane molecular bond and the layers therein are only held together by Coulombic forces between Zn and O ions. Consequently, LY has a threefold in-plane coordination. The unusual fivefold coordination and uniform charge distribution around the atoms in HX and its crystallographic similarity to RS suggest that the WZ → HX transformation observed here progresses toward an ionic bonding state with a higher coordination.

Figure 2 shows the tensile stress-strain  $(\sigma - \varepsilon)$  response of a nanowire with a  $21.22 \times 18.95$  Å cross-section at 100 K. While only data for a particular wire size and temperature is shown here, the transformation and the characteristics of the  $\sigma - \varepsilon$  relation are the same for wires with lateral dimen-

TABLE I. Lattice parameters for WZ, HX, and RS under different loading conditions. Select values are highlighted in boldface for easy comparison across different structures.

			WZ		НХ			RS	
Parameters	$\begin{array}{c} \text{DFT} \\ \sigma_b = 0 \text{ GPa} \end{array}$	$AP^{a}$ $\sigma_{b} = 0 \text{ GPa}$	$EXP^{b}$ $\sigma_{b} = 0 \text{ GPa}$	$DFT$ $\sigma_b = 10 \text{ GPa}$	DFT $\sigma_c = -6 \text{ GPa}$	$AP^{a}$ $\sigma_{b} = 10 \text{ GPa}$	$DFT$ $\sigma_b = 10 \text{ GPa}$	DFT $\sigma_c = -6 \text{ GPa}$	
a(Å)	3.20	3.22	3.25	3.12	3.28	3.34	3.29	3.49	4.16
b(Å)	5.54	5.66	5.63	5.93	5.68	6.24	6.42	6.03	4.16
v	0.33	0.32	0.33	0.33	0.34	0.32	0.32	0.33	0.50
c(Å)	5.15	5.30	5.21	5.00	4.92	4.35	4.18	4.18	4.16
и	0.38	0.41	0.38	0.39	0.39	0.50	0.50	0.50	0.50
b/a	1.73	1.76	1.73	1.90	1.73	1.87	1.95	1.73	1.00
c/a	1.61	1.65	1.60	1.60	1.50	1.30	1.27	1.20	1.00

<sup>&</sup>lt;sup>a</sup>Analytical Potential

<sup>&</sup>lt;sup>b</sup>Experiment [22]

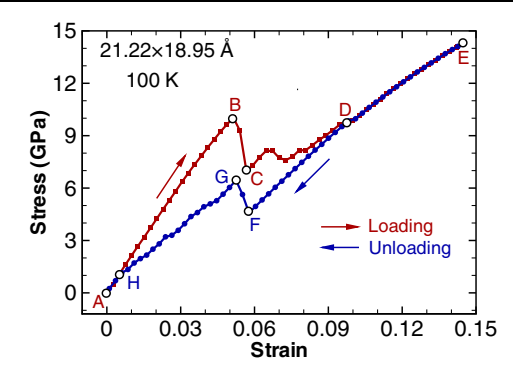


FIG. 2 (color online). Tensile stress-strain response of a  $21.22 \times 18.95$  Å nanowire at 100 K during loading-unloading. The hysteresis loop is relatively small.

sions between 18-40 Å and temperatures between 100-1200 K [27]. The region between A and B corresponds to elastic stretching of the WZ structure. Loading beyond B results in a stress drop from 10.02 to 6.98 GPa  $(B \rightarrow C)$  at  $\varepsilon = 5.14\%$ . This softening behavior corresponds to the nucleation of the HX phase. At this stage, u shows a precipitous change to 0.5 and the Zn and O basal planes become coplanar. As the deformation progresses, the transformed region sweeps through the entire wire length ( $C \rightarrow$ D) and the transformation completes at  $\varepsilon = 9.71\%$  ( $\sigma =$ 9.65 GPa). Further deformation occurs through the elastic stretching of the transformed structure (HX) and ultimate fracture occurs at  $\varepsilon = 16\%$  ( $\sigma = 15.29$  GPa, not shown) through cleavage along  $\{\bar{1}2\bar{1}0\}$  planes. Unloading from any strain prior to the initiation of failure, e.g., point E with  $\varepsilon = 14.5\%$ , is first associated with the recovery of the elastic deformation within the HX structure  $(E \rightarrow F)$ . A reverse transformation from HX to WZ  $(F \rightarrow G \rightarrow H)$ initiates at  $\varepsilon = 5.77\%$  ( $\sigma = 4.59$  GPa, point F) and completes at  $\varepsilon = 0.6\%$  ( $\sigma = 1.15$  GPa, point H). Unloading beyond H occurs through elastic deformation within the WZ structure  $(H \rightarrow A)$ . Strains up to 14.5% can be recovered, highlighting a very unusual aspect of the behavior of ZnO which normally is quite brittle. Obviously, the large recoverable strains observed here are associated with a unique structural transformation process which occurs only in [0110] nanowires under uniaxial tensile loading. The energy dissipation associated with the stress-strain hysteresis loop is  $\sim 0.16 \text{ J/m}^3$ , much lower than that for the WZ  $\rightarrow$  RS transformation in bulk (~1.38 J/m<sup>3</sup> with a maximum recoverable volumetric strain of 17% in compression) [3]. This low level of energy dissipation limits heat generation and heat-related damage, making the nanowires better suited for service under conditions of cyclic loading and large strains. It is important to point out that nanowires with other growth directions (e.g., [0001]) do not show such a phase transformation and are relatively brittle with failure strains not more than  $\sim$ 7%.

To identify stable crystalline structures under uniaxial tensile loading along the  $[01\bar{1}0]$  direction, we obtained their enthalpy as a function of c/a and b/a for specific

values of stress using DFT calculations. Since the transformation proceeds with the Zn and O basal planes becoming coplanar and a corresponding reduction in c, we also explored the stability of the HX phase under compression along the [0001] axis. The enthalpy per unit cell (2 Zn-O pairs) under applied loading is given by

$$H(c/a, b/a) = E(c, b, a, u, v) - f_i q_i,$$
 (1)

where E is the internal energy,  $f_iq_i$  (summation not implied) is the external work, and  $f_i$  is the uniaxial force per unit cell. For tension along the b axis, i = b,  $f_b = \sigma_b \times (ac)$ , and  $q_b = b$ . For compression along the c axis, i = c,  $f_c = \sigma_c \times (ab)$ , and  $q_c = c$ . For each pair of c/a and b/a, u, v, and unit cell size a (thus the volume) are allowed to relax to minimize H. The minima of the H(c/a, b/a) surface so obtained correspond to stable crystal structures under the applied stress.

Figure 3 shows the enthalpy surfaces (eV/unit cell) for  $\sigma_b=7$ , 10, and 13 GPa (with  $\sigma_c=0$  GPa) and  $\sigma_c=-6$  GPa (with  $\sigma_b=0$  GPa). In each case, there are two minima. For the tensile loading, the first minimum ( $^bH_{\min}^{WZ}$ ) is in the vicinity of  $c/a\approx 1.6$  and  $b/a\approx 1.9$ ; for the compressive loading, the first minimum ( $^cH_{\min}^{WZ}$ ) is in the vicinity of  $c/a\approx 1.5$  and b/a=1.732; each corresponding to a WZ structure with lattice parameters slightly different from those at zero stress (Table I). The second minimum in each of these plots corresponds to the HX phase. For the tensile loading, the second minimum ( $^bH_{\min}^{HX}$ ) is in the vicinity of  $c/a\approx 1.3$  and  $b/a\approx 1.9$ ;

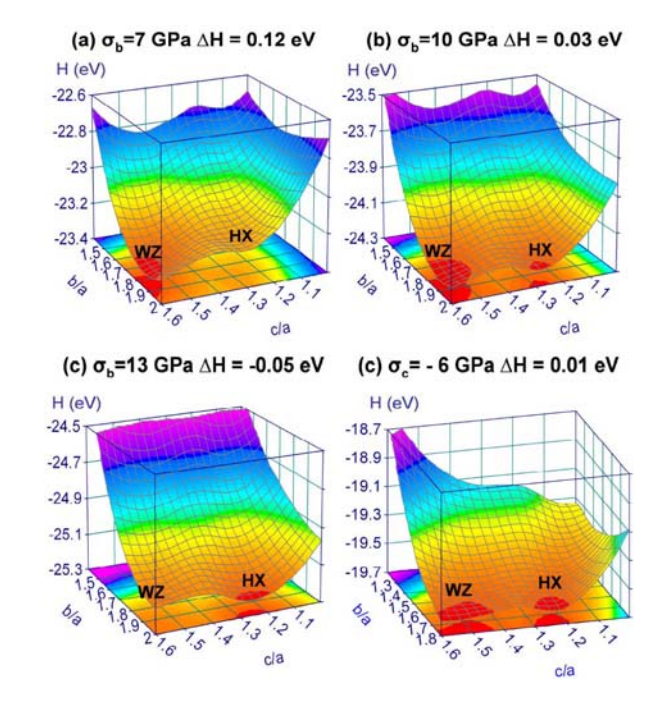


FIG. 3 (color online). Enthalpy surface maps from DFT calculations for uniaxial tensile stress of (a)  $\sigma_b = 7$  GPa, (b)  $\sigma_b = 10$  GPa and (c)  $\sigma_b = 13$  GPa along the b axis and uniaxial compressive stress of (d)  $\sigma_c = -6$  GPa along the c axis.

for the compressive loading, the second minimum ( $^cH_{\min}^{HX}$ ) is in the vicinity of  $c/a \approx 1.2$  and b/a = 1.732. The structure at  $^bH_{\min}^{HX}$  is that observed in the MD simulations discussed earlier. The difference in lattice parameters obtained from the two modes of loading stems from the fact that the ratio b/a is locked at 1.732 by structural symmetry under compression along the [0001] axis.

At a tensile stress of 7 GPa [Fig. 3(a)],  ${}^bH^{WZ}_{min}$  is much lower than  ${}^{b}H_{\min}^{HX}$  ( $\Delta H^{b} = {}^{b}H_{\min}^{HX} - {}^{b}H_{\min}^{HX} = 0.12 \text{ eV}$ ), hence, no transformation takes place. As the stress is increased to 10 GPa,  ${}^bH^{\rm HX}_{\rm min}$  and  ${}^bH^{\rm WZ}_{\rm min}$  become comparable  $(\Delta H^b = 0.03 \text{ eV})$  and consequently both WZ and HX are equally favored. At an applied stress of 13 GPa [Fig. 3(c)],  ${}^bH_{\min}^{\rm HX}$  is lower than  ${}^bH_{\min}^{\rm WZ}$  ( $\Delta H^b=-0.05$  eV), indicating that HX is more stable. The transformation barrier between the two phases of 0.06 eV (0.05 eV if calculated using the analytic potential) is quite low, compared with the barrier of  $\sim 0.15$  eV for the high pressure WZ  $\rightarrow$  RS transformation [7]. A similar behavior is observed under uniaxial compression along the [0001] direction. The WZ and HX enthalpy wells are comparable at  $\sigma_c = -6$  GPa [ $\Delta H^c =$ 0.01 eV, Fig. 3(d)]. At higher compressive stresses,  ${}^{c}H_{\min}^{HX}$ is lower than  ${}^{c}H_{\min}^{WZ}$ , indicating the relative favorability of HX under such conditions. As the magnitude of either  $\sigma_c$ or  $\sigma_b$  is increased above the corresponding equilibrium transition value, HX becomes more stable and the transformation barrier becomes even lower, resulting in an even higher driving force for transformation. In summary, the distinct minima in the vicinities of the HX and WZ structures on the enthalpy maps obtained through DFT calculations confirm what is discovered in MD calculations by pointing out that (1) HX is energetically favored over WZ above a critical applied tensile stress value of  $\sigma_b \approx$ 10 GPa along the  $[01\overline{1}0]$  direction or a critical compressive stress value of  $\sigma_c \approx -6$  GPa along the [0001] direction and (2) the barrier for the transformation decreases as applied stress increases.

HX can result from either uniaxial tension along the [0110] direction or uniaxial compression along the [0001] direction because both cause interatomic distances in Zn and O basal planes to increase, creating conditions favorable for the two types of atoms to be accommodated in a single plane. This process is similar to the fcc  $\rightarrow$  bcc Bain transformation [17]. Phenomenologically, the transformation can be explained by considering the effect of structural distortion on the nature of bonding. Specifically, under the external stresses discussed, lattice parameters change and the interatomic Coulombic interactions favor ionic states of bonding over covalent states of bonding [2]. For example, hydrostatic pressure can cause the progression of WZ (moderately ionic) toward RS (highly ionic), a s shown by both experiments and theoretical analyses [1,3-8]

Since HX and WZ can have very different properties, the stress-induced phase transformation may significantly alter the response of the nanowires. Examples include the modulation of piezoelectric constant, Seebeck coefficient, and thermal conductivity [28]. Such effects provide mechanisms for tuning the response of nanocomponents in a variety of nano-electro-mechanical systems through the application of mechanical input.

Support from NSF (No. CMS9984298), NSFC (No. 10528205), NANOTEC (No. NN49-024) and TRF (No. BRG4880015 and No. PHD/0264/2545) is acknowledged. Computations are carried out at the NAVO and ASC MSRCs.

\*To whom correspondence should be addressed.

Telephone: 404-894-3294.

Fax: 404-894-0186.

Email address: min.zhou@gatech.edu

- [1] C. H. Bates, W. B. White, and R. Roy, Science **137**, 993 (1962).
- [2] U. Ozgur et al., J. Appl. Phys. 98, 041301 (2005).
- [3] S. Desgreniers, Phys. Rev. B 58, 14102 (1998).
- [4] J. E. Jaffe and A. C. Hess, Phys. Rev. B 48, 7903 (1993).
- [5] J. E. Jaffe et al., Phys. Rev. B 62, 1660 (2000).
- [6] H. Karzel et al., Phys. Rev. B 53, 11425 (1996).
- [7] S. Limpijumnong and S. Jungthawan, Phys. Rev. B 70, 054104 (2004).
- [8] J. Serrano et al., Phys. Rev. B 69, 094306 (2004).
- [9] F. Claeyssens et al., J. Mater. Chem. 15, 139 (2005).
- [10] C.L. Freeman et al., Phys. Rev. Lett. 96, 066102 (2006).
- [11] J. Goniakowski, C. Noguera, and L. Giordano, Phys. Rev. Lett. 93, 215702 (2004).
- [12] R. B. Capaz, H. Lim, and J. D. Joannopoulos, Phys. Rev. B 51, 17755 (1995).
- [13] C. Q. Chen et al., Phys. Rev. Lett. 96, 075505 (2006).
- [14] S. X. Mao, M. Zhao, and Z. L. Wang, Appl. Phys. Lett. 83, 993 (2003).
- [15] Z. L. Wang, J. Phys. Condens. Matter 16, R829 (2004).
- [16] R. M. Wentzcovitch et al., Phys. Rev. B 38, 6191 (1988).
- [17] S. Limpijumnong and W. R. L. Lambrecht, Phys. Rev. Lett. 86, 91 (2001).
- [18] S. Limpijumnong and W. R. L. Lambrecht, Phys. Rev. B 63, 104103 (2001).
- [19] A. J. Kulkarni, M. Zhou, and F. J. Ke, Nanotechnology 16, 2749 (2005).
- [20] D. J. Binks and R. W. Grimes, J. Am. Ceram. Soc. 76, 2370 (1993).
- [21] D. Wolf et al., J. Chem. Phys. 110, 8254 (1999).
- [22] D.J. Binks, Ph.D. thesis, University of Surrey, Harwell, 1994.
- [23] R. W. Grimes, D. J. Binks, and A. B. Lidiard, Philos. Mag. A 72, 651 (1995).
- [24] G. Kresse and J. Furthmüller, Comput. Mater. Sci. 6, 15
- [25] D. Vanderbilt, Phys. Rev. B 41, 7892 (1990).
- [26] A. J. Kulkarni and M. Zhou, Acta Mechanica Sinica 22, 217 (2006).
- [27] A. J. Kulkarni et al. (unpublished).
- [28] A. J. Kulkarni and M. Zhou, Appl. Phys. Lett. 88, 141921 (2006).

# Hydrogen-Mediated Nitrogen Clustering in Dilute III-V Nitrides

Mao-Hua Du,<sup>1</sup> Sukit Limpijumnong,<sup>1,2</sup> and S. B. Zhang<sup>1</sup>

<sup>1</sup>National Renewable Energy Laboratory, Golden, Colorado 80401, USA

<sup>2</sup>National Synchrotron Research Center and School of Physics, Suranaree University of Technology, Nakhon Ratchasima, Thailand (Received 28 December 2005; published 15 August 2006)

First-principles calculation reveals multi-N clusters to be the ground states for hydrogenated N in dilute III-V nitrides. While hydrogenation of a single N, forming  $H_2^*(N)$ , can relax the large strain induced by the size-mismatched N, formation of the clusters will relax the strain even more effectively. This suppresses the formation of  $H_2^*(N)$ , the existence of which has recently been debated. More importantly, postgrowth dehydrogenation of the N-H clusters provides an explanation to the observed metastable bare N clusters in GaAsN grown by gas-source molecular beam epitaxy or metal-organic chemical vapor deposition.

DOI: 10.1103/PhysRevLett.97.075503 PACS numbers: 61.72.Vv, 71.55.Eq

The large size mismatch between a substitutional N and its larger isovalent host anion can profoundly alter the electronic properties of III-V semiconductors. At low to intermediate N concentration [N], where [N] is below the alloy limit of about 1 at. %, a series of bound and resonant states appears near the conduction band minimum (CBM) [1-3]. The appearance of the bound and resonant states was attributed to the formation of nitrogen clusters. Understanding the origin of the N-cluster-induced bound states in dilute nitrides is important, not only because they serve as efficient radiative recombination centers for excitons but also because they could act as free-carrier traps that reduce the efficiency of solar cells made on GaAsN. Kent and Zunger have performed large-scale empirical pseudopotential calculations for the bare N clusters [4]. They showed that, in most cases, it is the *nearest-neighbor* N clusters that produce the bound states inside the band gap, seen by photoluminescence measurements [1-3]. In particular, a family of the [110] N chains produces successively the deeper bound states as each additional N is added. In contrast, the non-nearest-neighbor N pairs usually give resonant states above the CBM.

In spite of the study in Ref. [4], the fundamental question concerning the formation of the N clusters remains unanswered. In fact, the [110] chains are highly strained in the chain direction. It is precisely this strain that causes the bound states to appear inside the band gap. As such, the [110] N chains are expected to be unstable compared with other forms of N clusters. Indeed, our first-principles calculations showed sizable negative binding energies (meaning repulsive) of -0.13, -0.22, and -0.31 eV per N, respectively, for the [110] N dimer, trimer, and tetramer.

In this Letter, we will show that the formation of highly strained N clusters may be due to an unexpected effect, i.e., hydrogenation. Our first-principles calculations show that hydrogen can assist the formation of the [110] N chain clusters in GaAsN, thereby completely reversing the above binding energy trend in bare N clusters. In particular, hydrogenated monomers such as  $H_2^*(N)$  will cluster into

the hydrogenated dimer, trimer, or tetramer with significant energy lowering from 0.35 to 0.5 eV per N. The reason is that hydrogenation can reduce the local strain near  $N_{As}$  and even more effectively for multi-N clusters. A detailed-balance study at a typical growth temperature of 420 °C shows that the hydrogenated N dimer  $H_2^{**}(2N)$  is the most abundant species under thermal equilibrium among the various hydrogenated N clusters, regardless of the H concentration. This explains for the first time why experiment has so far failed to detect the  $H_2^{**}(N)$  complex, which is the most stable hydrogenated N monomer [5].

Moreover, we expect that [H] should be significantly higher near the growth front than in the interior, resulting in a gradient in the H chemical potential,  $\mu_{\rm H}$ , being higher near the surface but lower inside, as revealed by recent experiments [6,7]. This, combined with our calculated energetics, suggests a dehydrogenation of the N clusters once the growth front has passed. Indeed, recent experiment showed that, upon rehydrogenation, the multi-N clusters are the ones first to be rehydrogenated [8]. Our proposal is in accordance with the fact that the highconcentration N is usually incorporated by gas-source molecular beam epitaxy (GSMBE) [3,9,10], metal-organic chemical vapor deposition (MOCVD) [1-3,11-14], or ion implantation [15,16]. The GSMBE or MOCVD involves a large number of hydrogen-containing molecules or radicals during the growth, whereas the ion implantation creates numerous vacancies. Binding N with vacancies can also reduce the large strain induced by the sizemismatched N. Thus, in contrast to the common role of hydrogen in semiconductors to passivate electronic states of impurities and defects [17] and the recovery of the band gap of GaAsN [18], our study here reveals the unexpected effect of H to assist the formation of the N clusters, which needs to be suppressed in order to use such large lattice-mismatched semiconductors for optoelectronic applications.

We performed calculations using the density functional theory within the local density approximation, as implemented in the Vienna *ab initio* simulation package [19]. Ultrasoft pseudopotentials were employed to treat the ion-electron interactions. A plane wave basis set was used for the wave function expansion with a kinetic energy cutoff of 348 eV. We mimic isolated N-H complexes by using a supercell approach. Unless otherwise specified, all the calculations were done using a 216-atom cubic cell with a calculated GaAs lattice constant of 5.593 Å [20]. A  $2 \times 2 \times 2$  grid was used for the *k*-point sampling, corresponding to 4 *k* points in the irreducible Brillouin zone. All the atoms were relaxed to minimize the Feynman-Hellmann forces to below 0.02 eV/Å.

Figure 1 shows the calculated structures for the three lowest-energy monomers  $\alpha\text{-H}_2{}^*(N),~\beta\text{-H}_2{}^*(N),~$  and  $\gamma\text{-H}_2{}^*(N).$  The  $\alpha\text{-H}_2{}^*$  is more stable than the  $\beta\text{-H}_2{}^*$  and  $\gamma\text{-H}_2{}^*$  by 0.16 and 0.04 eV per N, respectively. The  $\alpha\text{-}$  and  $\beta\text{-H}_2{}^*$  have been studied previously [5,21], but the  $\gamma\text{-H}_2{}^*$  has not. The calculated 0.04 eV/N energy difference between  $\alpha\text{-}$  and  $\gamma\text{-H}_2{}^*$  is rather small. Therefore, a slight elongation of the Ga-N bond (e.g., induced by the strain of a second nearby N) can make the latter more stable, as a larger Ga-N distance can better accommodate two bond-centered H.

We define the binding energy of a hydrogenated N cluster with respect to the hydrogenated ground-state monomer  $\alpha$ -H $_2^*$ (N) as

$$E_B = \{n_N E_{\text{tot}}[\alpha - H_2^*(N)] - E_{\text{tot}}[(n_N N)(n_H H)] + (n_H - 2n_N)(\mu_{H,\text{mol}} + \mu_H)\}/n_N,$$
(1)

where  $E_{\rm tot}$  is the total energy of the supercell,  $n_{\rm H}$  and  $n_{\rm N}$  are the numbers of H and N in the cluster, respectively, and  $\mu_{\rm H}$  is the chemical potential of the H, referenced to  $\mu_{\rm H,mol}$  (half of the total energy for an H<sub>2</sub> molecule in the vacuum). In such a definition, a positive sign in  $E_B$  corresponds to binding.

Hydrogenated monomers bind to each other via minimization of their local strains. Figure 1 shows that in  $\alpha$ -H<sub>2</sub>\*(N) all three Ga-N bonds are strained, whereas in  $\beta$ -H<sub>2</sub>\*(N) all three Ga-As bonds are strained. Therefore, it is energetically favored to cluster an  $\alpha$ -H<sub>2</sub>\*(N) and a  $\beta$ -H<sub>2</sub>\*(N) together antiparallell to form a hydrogenated N dimer (H<sub>2</sub>\*)<sub>2</sub>(2N), as shown in Fig. 2(a), because such clustering reduces the number of strained bonds by 2. As a result, the Ga(1)-N(1) bond length in (H<sub>2</sub>\*)<sub>2</sub>(2N),

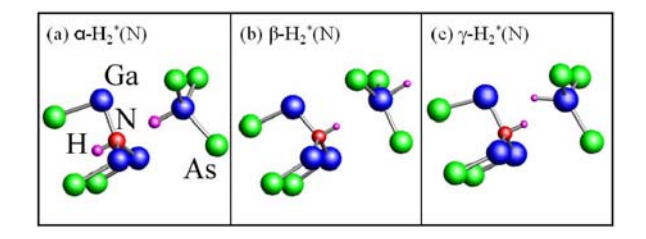


FIG. 1 (color online). Hydrogenated N monomers: (a)  $\alpha$ -H<sub>2</sub>\*(N), (b)  $\beta$ -H<sub>2</sub>\*(N), and (c)  $\gamma$ -H<sub>2</sub>\*(N).

 $d_{\text{Ga-N}} = 1.96 \,\text{Å}$ , is only 2% longer than that of bulk GaN,  $d_{\text{Ga-N}} = 1.92 \,\text{Å}$ . No other Ga-N bond ( $d_{\text{Ga-N}} = 2.03 \,\text{Å}$ ) has been weakened in the process; therefore, formation of the  $(\text{H}_2^*)_2(2\text{N})$  is favored by  $E_B = 0.22 \,\text{eV}$  per N.

One can further eliminate the two Ga-bonded H in Fig. 2(a) to form a strained Ga-Ga bond, as we recently showed that the Ga-H bond is generally weak [22]. This leads to our second hydrogenated N dimer  $H_2^{\ **}(2N)$  in Fig. 2(b), which resembles somewhat the  $H_2^{**}$  in Si [23]. However, while the formation of H<sub>2</sub>\*\* from an H<sub>2</sub>\* in Si and GaAs is always endothermic, the formation of the  $H_2^{**}(2N)$  from two  $\alpha$ - $H_2^{*}(N)$  in GaAsN is surprisingly exothermic with  $E_B = 0.35$  eV per N. Hence, at  $\mu_H = 0$ ,  $H_2^{**}(2N)$  is also more stable than  $(H_2^*)_2(2N)$  by 0.15 eV per N. At first glance, this is surprising, because the formation of a weak Ga-Ga bond is usually not favored. However, by forming this bond, two weak Ga-H bonds are eliminated, and the two released H can also form a strong bond to become a free H<sub>2</sub> molecule. In addition, the formation of the Ga-Ga bond reduces the space at the N(1)site in Fig. 2(b), which is desirable for smaller atoms such as nitrogen. We find that the Ga-N bonds around the N(1) atom in  $H_2^{**}(2N)$ ,  $d_{Ga-N} = 1.96$  and 2.01 Å, are significantly less strained than those in  $\alpha$ -H<sub>2</sub>\*(N). If one replaces the N(1) by an As, for example, such a strain reduction would be impossible, and the resulting structure is 1.26 eV higher in energy than the  $\alpha$ -H<sub>2</sub>\*(N). On the other hand, replacing N(2) by As costs only 0.41 eV with respect to the  $\alpha$ -H<sub>2</sub>\*(N). The calculated H vibrational modes for  $H_2^{**}(2N)$  are 3240 and 3203 cm<sup>-1</sup>.

From the N dimers in Fig. 2, there are two open-ended paths to build larger clusters. In path 1, one adds additional  $H_2^*(N)$  units to  $(H_2^*)_2(2N)$  to form  $(H_2^*)_3(3N)$ ,  $(H_2^*)_4(4N)$ , etc., to longer  $(H_2^*)_n(nN)$  chains. In path 2, one adds one  $H_2^*(N)$  to  $H_2^{**}(2N)$ , to form  $H_2^*H_2^{**}(3N)$ 

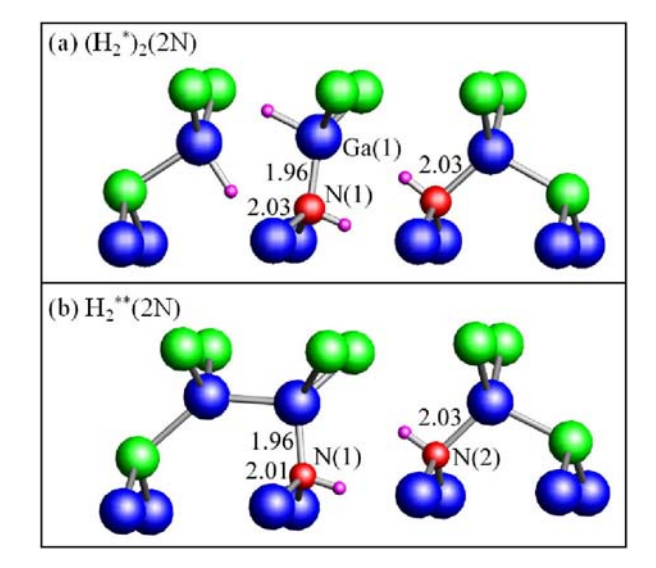


FIG. 2 (color online). Hydrogenated N dimers: (a)  $({\rm H_2}^*)_2(2{\rm N})$  and (b)  ${\rm H_2}^{**}(2{\rm N})$ .

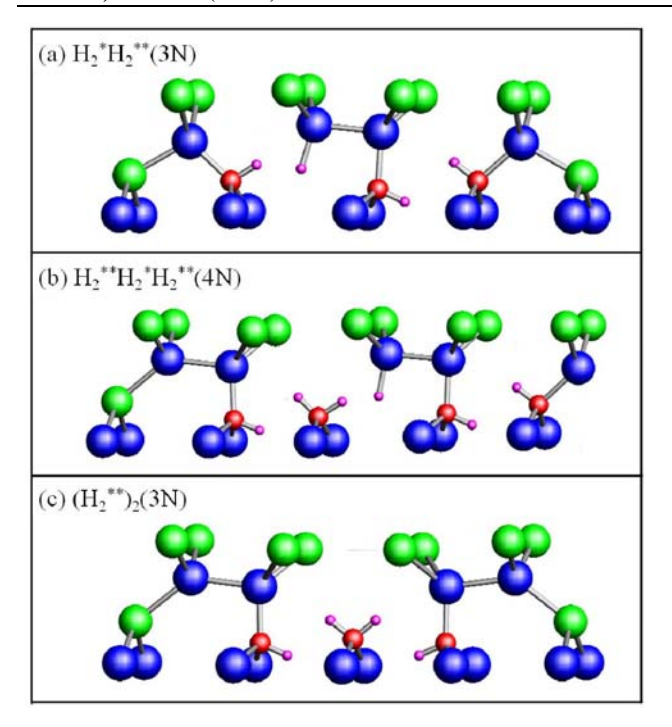


FIG. 3 (color online). Hydrogenated N clusters: (a)  $H_2*H_2**(3N)$ , (b)  $H_2**H_2**(4N)$ , and (c)  $(H_2**)_2(3N)$ .

[Fig. 3(a)], another  $H_2^{**}(N)$  to the  $H_2^{*}H_2^{**}(3N)$  to form  $H_2^{**}H_2^{**}(4N)$  [Fig. 3(b)], and eventually to a periodic [110] chain with  $H_2^{*}H_2^{**}$  as the basic unit. Note that one can alter the chain sequence in path 2 by inserting  $H_2^{**}H_2^{**}$  twins, in which two consecutive  $H_2^{**}$  share one common N. Figure 3(c) shows the core of the twin as  $(H_2^{**})_2(3N)$ . Interestingly, hydrogen in GaAsN can exist only as chains, not as the platelets seen in Si [24]. This is because the N atoms associated with the platelet would cause too much in-plane strain. The calculated  $E_B$  for the various clusters are shown in Fig. 4: In path 1, all the  $E_B$  are independent of  $\mu_H$ . In path 2, while the relative  $E_B$  within the path is still independent of  $\mu_H$ , the absolute  $E_B$  will

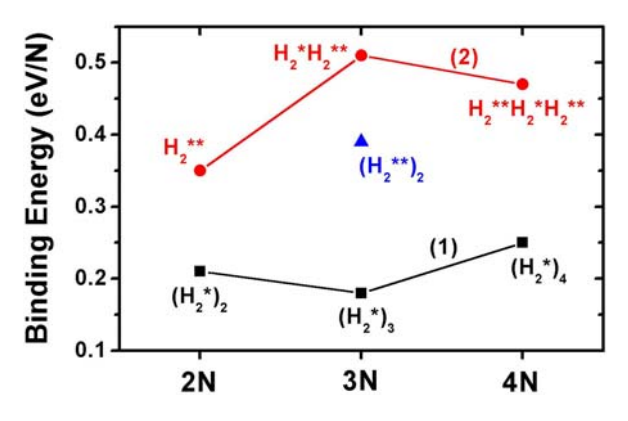


FIG. 4 (color online). Binding energy of the various N-H clusters with respect to  $\alpha$ -H $_2^*$ (N), calculated using Eq. (1). For path 2,  $\mu_{\rm H}$  is set to zero.

increase if  $\mu_{\rm H}$  < 0. Note that, in all the cases, N clusters are fully passivated by H without any electronic state in the band gap.

To determine the relative concentrations of the N-H complexes, we have performed a detailed-balance calculation. We used a typical experimental N concentration, 1 at. % at  $T=420\,^{\circ}\mathrm{C}$ , and the binding energies in Fig. 4 to calculate the concentrations for the various N-H complexes as a function of [H], shown in Fig. 5. Note that  $\mathrm{H_2}^{***}$  and  $\mathrm{H_2}^{**}\mathrm{H_2}^{***}$  (the basic building unit in path 2) dominate over the entire [H] range. On the other hand, the concentration of the  $\mathrm{H_2}^{**}$  is never significant.

Figure 5 is a thermal equilibrium picture. Its validity thus depends on the diffusivity of N at growth temperature, which for GaAsN varies between 420 and 650 °C [3]. Anion diffusion usually takes place either via an anion vacancy  $(V_{As})$  mechanism or an anion interstitial kickout mechanism. Assuming the former, we have calculated the barriers for  $V_{\rm As}$  diffusion and for the hopping of an N to its nearest neighbor  $V_{\rm As}$  to be 2.0 and 2.45 eV, respectively. These results suggest an appreciable N diffusion at  $T \ge$ 700 °C. In the presence of hydrogen, however, these diffusion barriers are considerably lowered. For example, in H<sub>2</sub>\*, where one of the four Ga-N bonds is cut, our calculations show the energy barrier for displacing N to the nearest neighbor  $V_{\rm As}$  is reduced by 0.54 eV to 1.9 eV. A recent study on  $V_N$  diffusion in GaN also showed a similar reduction of the barrier by 0.58 eV by hydrogen [25]. It is possible that the interstitial kickout mechanism can result

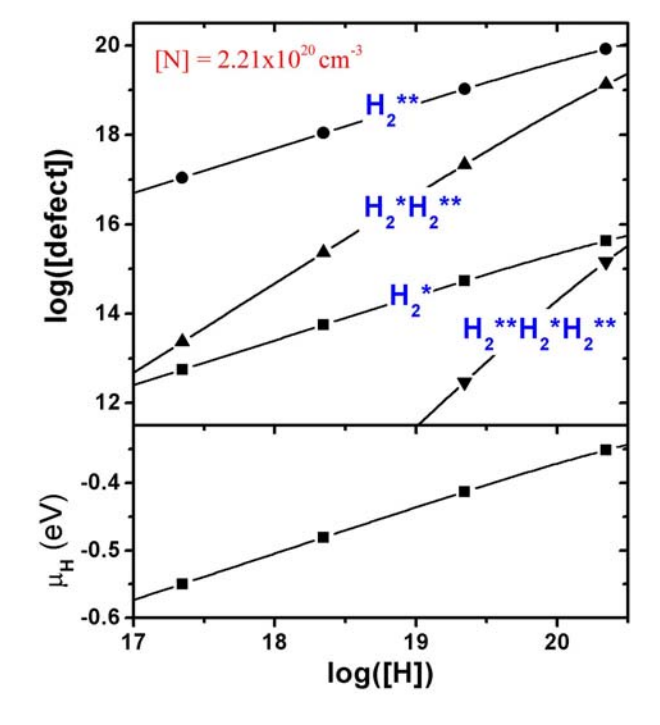


FIG. 5 (color online). (Top) Concentration of the various N-H clusters and (bottom) system H chemical potential under thermal equilibrium as a function of the hydrogen concentration H at the conditions of [N] =  $2.21 \times 10^{20}$  cm<sup>-3</sup> and T = 420 °C.

in even lower barriers. In other words, H-assisted N diffusion is highly likely over the growth temperature range.

In the GSMBE or MOCVD growth of GaAsN using the H-rich ligands, it is typical that there is a high [H] (and, hence, high  $\mu_{\rm H}$ ) at the growth front, but lower [H] (and, hence, lower  $\mu_{\rm H}$ ) in the interior of the sample [6,7]. This suggests that the presence of nearest-neighbor N clusters in dilute III-V nitrides could be a consequence of postgrowth H desorption from the multi-N-H complexes. Figure 5 shows that, as [H] decreases, the number of hydrogenated N clusters also decreases [26]. Because the barrier to further dissociate substitutional fourfold-coordinated N atoms from the clusters is significantly larger than that of the onefold-coordinated H, bare N clusters are left behind. Our model suggests that these freeze-in N clusters should be more prone to rehydrogenation than isolated N<sub>As</sub>. Indeed, recent experiments showed that, upon rehydrogenation of GaAsN, it is the N clusters that first disappear in the photoluminescence spectra [8].

In summary, first-principles study reveals the rich structures of a ground-state cluster phase of the N-H complexes in dilute III-V nitrides grown under the H-rich environment. We find that the relaxation of the nitrogen-induced strain is responsible for the stability of the clusters. The dominance of the cluster phase may explain the absence of IR modes from the most stable monomer  $\mathrm{H_2}^*(\mathrm{N})$ . Furthermore, we suggest that a postgrowth dehydrogenation of the N-H clusters provides an energetic origin for the observation of metastable N clusters in GaAsN, whose presence could be harmful to the optoelectronic properties of GaAsN.

This work was supported by the U.S. DOE/BES and DOE/EERE under Contract No. DE-AC36-99GO10337 and by the NERSC for MPP time. The work in Thailand was supported by the Thailand Research Fund under Contract No. BRG4880015 and by the AFOSR/AOARD under Contract No. FA5209-05-P-0309.

- X. Liu, M.-E. Pistol, and L. Samuelson, Phys. Rev. B 42, 7504 (1990).
- [2] X. Liu, M.-E. Pistol, and L. Samuelson, Appl. Phys. Lett. 56, 1451 (1990).
- [3] Y. Zhang, A. Mascarenhas, J. F. Geisz, H. P. Xin, and C. W. Tu, Phys. Rev. B 63, 085205 (2001).
- [4] P. R. C. Kent and A. Zunger, Phys. Rev. B 64, 115208 (2001).
- [5] A. Janotti, S.B. Zhang, Su-Huai Wei, and C.G. Van de Walle, Phys. Rev. Lett. 89, 086403 (2002).
- [6] H. P. Xin, C. W. Tu, and M. Geva, Appl. Phys. Lett. 75, 1416 (1999).
- [7] H. P. Xin, C. W. Tu, and M. Geva, J. Vac. Sci. Technol. B 18, 1476 (2000).

- [8] A. Polimeni, G. Baldassarri Höger von Högersthal, F. Masia, A. Frova, M. Capizzi, S. Sanna, V. Fiorentini, P. J. Klar, and W. Stolz, Phys. Rev. B 69, 041201(R) (2004).
- [9] S. Francoeur, S.A. Nikishin, C. Jin, Y. Qiu, and H. Temkin, Appl. Phys. Lett. 75, 1538 (1999).
- [10] I. A. Buyanova, G. Pozina, P. N. Hai, N. Q. Thinh, J. P. Bergman, W. M. Chen, H. P. Xin, and C. W. Tu, Appl. Phys. Lett. 77, 2325 (2000).
- [11] T. Makimoto, H. Saito, T. Nishida, and N. Kobayashi, Appl. Phys. Lett. 70, 2984 (1997).
- [12] R. Schwabe, W. Seifert, F. Bugge, R. Bindemann, V.F. Agekyan, and S. V. Pogarev, Solid State Commun. 55, 167 (1985).
- [13] T. Makimoto, H. Saito, and N. Kobayashi, Jpn. J. Appl. Phys. 36, 1694 (1997).
- [14] J. F. Geisz, D. J. Friedman, J. M. Olson, S. R. Kurtz, and B. M. Keyes, J. Cryst. Growth 195, 401 (1998).
- [15] T. Shima, Y. Makita, S. Kimura, T. Iida, H. Sanpei, M. Yamaguchi, K. Kuto, K. Tanaka, N. Kobayashi, A. Sandhu, and Y. Hoshino, Nucl. Instrum. Methods Phys. Res., Sect. B 127/128, 437 (1997).
- [16] T. Shima, Y. Makita, S. Kimura, H. Sanpei, Y. Fukuzawa, A. Sandhu, and Y. Nakamura, Appl. Phys. Lett. 74, 2675 (1999).
- [17] Hydrogen in Semiconductors, edited by N.H. Nickel, M.D. McCluskey, and S.B. Zhang (Materials Research Society, Warrendale, PA, 2004).
- [18] A. Polimeni, G.B.H. von Hogersthal, M. Bissiri, M. Capizzi, A. Frova, M. Fischer, M. Reinhardt, and A. Forchel, Semicond. Sci. Technol. 17, 797 (2002).
- [19] G. Kresse and J. Furthmüller, Phys. Rev. B 54, 11169 (1996).
- [20] We have tested directly the cell-size effect on the 2N cluster H<sub>2</sub>\*\*\*(2N) by using 64- and 216-atom cells. When the larger 216-atom cell is used, N binding energy increases by only 0.07 eV. Hence, for clusters of such sizes, the 216-atom cell is large enough. We have also studied the effect due to lattice constant relaxation for the 4N cluster but not the cell-size effect directly, because a 64-atom cell would be too small but any cell significantly larger than the 216-atom one is beyond our current computational capability. Here changes in the formation and binding energies due to the lattice constant relaxation are 0.06 and 0.03 eV/N, respectively. Both tests suggest that cell-size effects are small and can hence be ignored.
- [21] A. A. Bonapasta, F. Filippone, and P. Giannozzi, Phys. Rev. B 68, 115202 (2003).
- [22] M.-H. Du, S. Limpijumnong, and S. B. Zhang, Phys. Rev. B 72, 073202 (2005).
- [23] D. J. Chadi, Appl. Phys. Lett. 83, 3710 (2003).
- [24] S. B. Zhang and W. B. Jackson, Phys. Rev. B 43, R12 142 (1991).
- [25] R.R. Wixom and A.F. Wright, Appl. Phys. Lett. 87, 201901 (2005).
- [26] Dehydrogenation of  $H_2^{**}(2N)$  raises the question of whether one can experimentally detect it by the current spectroscopic methods.

# Evidence for Native-Defect Donors in *n*-Type ZnO

D. C. Look, <sup>1,2</sup> G. C. Farlow, <sup>1</sup> Pakpoom Reunchan, <sup>3</sup> Sukit Limpijumnong, <sup>3,4</sup> S. B. Zhang, <sup>4</sup> and K. Nordlund <sup>5</sup>

<sup>1</sup>Semiconductor Research Center, Wright State University, Dayton, Ohio 45435, USA

<sup>2</sup>Materials and Manufacturing Directorate, Air Force Research Laboratory, Wright-Patterson Air Force Base, Ohio 45433, USA

<sup>3</sup>School of Physics, Suranaree University of Technology and National Synchrotron Research Center, Nakhon Ratchasima, Thailand

<sup>4</sup>National Renewal Energy Laboratory, Golden, Colorado 80401, USA

<sup>5</sup>Accelerator Laboratory, University of Helsinki, FIN-00014, Helsinki, Finland

(Received 5 August 2005; published 21 November 2005)

Recent theory has found that native defects such as the O vacancy  $V_{\rm O}$  and Zn interstitial Zn<sub>I</sub> have high formation energies in n-type ZnO and, thus, are not important donors, especially in comparison to impurities such as H. In contrast, we use both theory and experiment to show that, under N ambient, the complex Zn<sub>I</sub>-N<sub>O</sub> is a stronger candidate than H or any other known impurity for a 30 meV donor commonly found in bulk ZnO grown from the vapor phase. Since the Zn vacancy is also the dominant acceptor in such material, we must conclude that native defects are important donors and acceptors in ZnO.

DOI: 10.1103/PhysRevLett.95.225502

Semiconducting ZnO has generated great interest in the past decade because of advances in bulk and epitaxial growth that have opened the door for new photonic and electronic applications, such as UV light emitting diodes and transparent transistors [1,2]. Previous research had established that ZnO was always n-type and that the dominant donors were usually shallow with activation energies of between 30 and 60 meV [3,4]. Because it was also known that the crystal growth was typically Zn-rich, the dominant donor was almost always identified as either the O vacancy  $V_{\rm O}$  or the Zn interstitial Zn<sub>I</sub> [5,6]. This model was strongly challenged in the year 2000 when Kohan et al. showed theoretically that both  $V_{\rm O}$  and  ${\rm Zn}_I$  have high formation energies in *n*-type ZnO and that, furthermore, both are deep, not shallow, donors [7]. More recent theory has concluded that  $Zn_I$  is actually a shallow donor, rather than deep [8,9], as has also been suggested by electronirradiation experiments [6]; however, its high formation energy would still limit its participation in the conductivity of *n*-type material. Also in the year 2000, the defect-donor model was further challenged by Van de Walle's theoretical result that H is always a donor in ZnO, that it is easily ionized, and that it has a low enough formation energy to be abundant; thus, Van de Walle suggested that it was likely to be a dominant background donor in ZnO materials that were exposed to H during growth [10]. This proposal has been amenable to testing, because H-containing, highquality, bulk ZnO, grown by a seeded chemical vapor transport (SCVT) technology, has been commercially available for the past few years. For the most part, these tests have confirmed that a shallow donor due to H exists in SCVT ZnO and can contribute significantly to the conductivity [11–16]. This fact, coupled with the theoretical evidence of high formation energies for the native donors [7], has led to a prevailing opinion that native donors do not play a significant role in the conductivity of as-grown ZnO. In contrast, we will offer evidence here that native donors

can contribute significantly to conduction in ZnO but as complexes, rather than isolated elements.

PACS numbers: 61.72.Ji, 71.55.Gs, 72.20.Fr, 78.55.Et

The main sample used in this study was a 5 mm  $\times$ 5 mm × 0.42 mm piece cut from a wafer grown by the SCVT technique at ZN Technology, Inc. [17]. Material of this type is of very high quality, with peak electron mobility >2000 cm<sup>2</sup>/V s, 300 K carrier concentration in the 10<sup>16</sup> cm<sup>-3</sup> range, and photoluminescence (PL) linewidths under 0.5 meV, as shown in Figs. 1 and 2 [4]. The sample was first annealed at 715 °C, in order to release most of the H [14,15], then was irradiated with high-energy electrons to create point defects, and finally was annealed again at temperatures from 200-500 °C, in order to investigate the annihilation of the point defects. As seen in Fig. 1, several sharp PL lines appear in the region 3.357-3.365 eV, and these spectral features are usually assigned to transitions of excitons bound to neutral donors ( $D^0X$  transitions), in which the donor remains in its ground state (n = 1) during the transition. Some of these lines have been tentatively identified; for example, the lines at 3.35964 eV ( $I_8$  or  $I_{8a}$  in

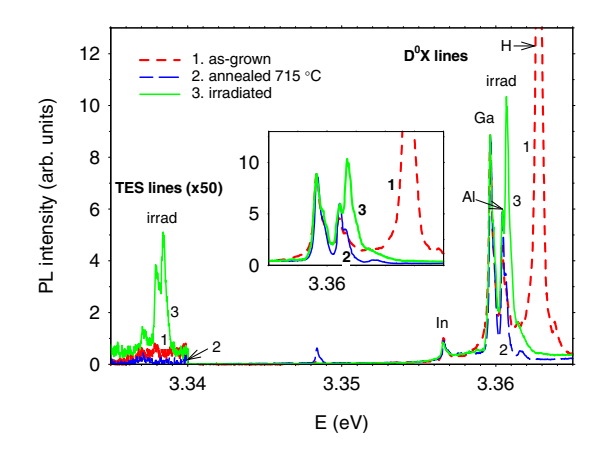


FIG. 1 (color online). 4-K photoluminescence spectra for ZnO sample. The inset shows the  $D^0X$  lines in greater detail.

the literature) and 3.36042 eV ( $I_6$  or  $I_{6a}$ ) have been assigned to  $\mbox{Ga}_{\mbox{Z}\mbox{n}}$  and  $\mbox{Al}_{\mbox{Gn}},$  respectively. (See Ref. [18] for an excellent review of PL in ZnO.) All of the spectra presented in this work are normalized to the  $I_8$  line, because it is relatively isolated and also not expected to change significantly as a result of annealing or irradiation treatments. However, the most dominant PL line in this particular sample before annealing is the  $D^0X$  line at 3.36270 eV  $(I_4)$ , now almost universally assigned to interstitial H [16,18]. This identification results at least partially from annealing experiments, because  $I_4$  disappears for anneals above 600 °C, in good correlation with the effusion of H from the sample [14-16,19]. Our sample behaves in the same way, as evidenced by the strong reduction of  $I_{4}$  after an anneal of 715 °C (curve 2 in Fig. 1). Not shown in Fig. 1 is a two-electron satellite (TES) replica of  $I_4$ , appearing at 3.32961 eV. A TES transition is one in which the donor is left in an excited n = 2 state after the collapse of the exciton. If the donor associated with  $I_4$  follows a hydrogenic model, then the ground-state (n = 1) energy of this donor should be given by 4/3(3.36270 - 3.32961) =44.1 meV. Other TES transitions, also not shown, are seen near 3.32 eV and may be associated with  $I_6$  and  $I_8$ [18]. If so, then the hydrogenic model would predict ground-state energies of 53-55 meV for these donors, presumably associated with Ga<sub>Zn</sub> and Al<sub>Zn</sub>. Thus, the donors identified from PL are H, at 44 meV, and Ga<sub>Zn</sub> and  $Al_{Zn}$ , at about 55 meV.

To create point defects, we have used the Van de Graaff electron accelerator at Wright State University. The sample was irradiated on the Zn face (0001) with 1 MeV electrons three separate times, making a total fluence of  $3 \times$ 10<sup>17</sup> cm<sup>-2</sup>. The PL spectrum after the third irradiation is presented as curve 3 in Fig. 1. A new sharp defect line at 3.36070 eV, which we will designate as  $I_D$ , is generated by the irradiation. Concomitantly, a triplet feature, comprised of energies 3.33711, 3.33793, and 3.33840 eV, is also generated. These we will designate  $I_{D,TES1}$ ,  $I_{D,TES2}$ , and  $I_{D,TES3}$ . This triplet has an intensity about 100 times less than that of  $I_D$ , and this reduction is about the same as that observed for the TES line of H compared with its parent line,  $I_4$ . Thus, the defect triplet at 3.338 eV clearly is related to  $I_D$ , and, if the hydrogenic model holds, the associated energy is  $4/3(3.3607 - 3.3379) \approx 30.4 \text{ meV}$ . This value is less than that predicted from an empirical version of Haynes' rule presented in Ref. [18]. However, that version was developed for simple, isolated impurities, Al, Ga, In, and H, and there is no reason to expect that it should hold for a defect-related complex. Both  $I_D$  and its TES triplet are greatly reduced for anneals greater than 500 °C (not shown), evidently due to defect recombination. It is important to note at this point that the as-grown sample, represented by curve 1 in Fig. 1, has two small lines at the energies of  $I_{D,TES1}$  and  $I_{D,TES2}$ , respectively, and possibly also a line in the  $I_D$  region, although obscured by  $I_6$ . This is our first indication that the as-grown sample contains defect-related donors.

We next discuss the temperature-dependent mobility  $\mu$  and carrier concentration n, shown in Fig. 2. To avoid clutter, we show curves representing only four stages in the evolution of this sample: (1) as-grown; (2) annealed at 715 °C for 1/2 hour in flowing  $N_2$  gas; (3) irradiated with 1 MeV electrons, in three equal stages up to a total fluence of  $3 \times 10^{17}$  cm<sup>-2</sup>; and (4) annealed at 400 °C, following previous anneals beginning at 200 °C. It should be noted that a final anneal at 500 °C (not shown) eliminated almost all of the irradiation damage and basically returned the  $\mu$  and n curves to those of stage 2. [Note that a return to the  $\mu$  and n curves of stage 1 (as-grown) is of course impossible, because the H content was lost in stage 2, the first 715 °C anneal.]

The mobility data (inset in Fig. 2) were fitted to an accurate charge-carrier scattering theory, described elsewhere [20], and the only fitting parameter was the acceptor concentration  $N_A$ . The carrier concentration data of Fig. 2 were then fitted to the charge-balance equation:

$$n + N_A = \sum_{i} \frac{N_{Di}}{1 + n/\phi_{Di}},\tag{1}$$

where the subscript i denotes a particular donor and where  $\phi_{Di}$  is a function of T and  $E_{Di}$ , the donor energy [cf. Eq. (8) of Ref. [20]]. The fitting parameters in Eq. (1) are the donor concentrations  $(N_{Di}$ 's), donor energies  $(E_{Di}$ 's), and acceptor concentration  $N_A$ . Excellent fits to the n vs 1/T data in Fig. 2 were obtained by also including a degenerate surface layer in the analysis [20,21].

The PL results discussed above determined the energies of three different donors, calculated from their respective TES lines: 55 meV, possibly associated with  $Ga_{Zn}$  and/or  $Al_{Zn}$ ; 44 meV, associated with H; and 30 meV, produced by irradiation and thus associated with a defect. Indeed, the 30 and 44 meV energies turn out to be good fitting parameters for two of the three donors required to fit our Hall-effect data, but the third donor is best fitted with about 75 meV, rather than 55 meV. The carrier concentration fits are

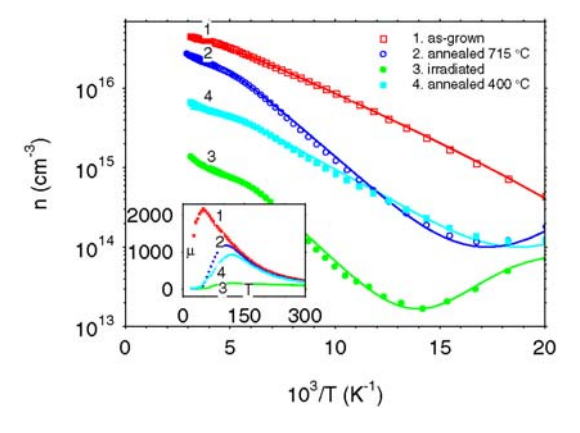


FIG. 2 (color online). Temperature-dependent carrier concentration for ZnO sample. The solid lines are theoretical fits. The inset shows the experimental mobility curves after the same four treatments.

shown as solid lines in Fig. 2, and the fitting parameters are given in Table I. Two major conclusions are evident from the results: (1) the 44 meV H level essentially disappears during the 715 °C anneal, in agreement with the PL data; and (2) a 30 meV level is produced by irradiation but also exists in the as-grown sample and the sample annealed at 715 °C. It should be emphasized that the choice of 30 meV as a Hall fitting parameter is not dependent on the fact that the PL analysis also found a donor at 30 meV. Indeed, a donor of this energy has been found previously by a number of groups to give good fits to ZnO Hall-effect data [3,4,6]. To help identify this 30 meV donor, we appeal to theory.

First of all, we calculate the expected 1 MeV-electron-bombardment production rates of Zn and O Frenkel pairs from molecular dynamics simulations [22]. The threshold energies were calculated by giving a randomly chosen O or Zn atom a recoil energy in a random direction in an experimentally controlled angular window of 15 degrees around the desired (0001) direction. The interatomic interaction model for the ZnO system will be published elsewhere [23], but the potential development principles are described in Ref. [24]. To account for the experimental situation with a beam acceptance angle, the threshold was determined as the average over the direction-specific thresholds obtained within the 15° angular window.

For Zn-face (0001) irradiation at 300 K, the threshold for O displacement is 44 eV, and that for Zn displacement, 34 eV. We then apply the McKinley-Feshbach relativistic cross-section formula [25] to give effective production rates of 0.18 cm<sup>-1</sup> for O displacement and 0.30 cm<sup>-1</sup> for Zn displacement. Thus, we would expect that our fluence of  $3 \times 10^{17}$  cm<sup>-2</sup> would produce  $O_I$  and  $V_O$  concentrations of about  $5 \times 10^{16}$  cm<sup>-3</sup> and  $Z_{n_I}$  and  $V_{Z_n}$  concentrations of about  $9 \times 10^{16}$  cm<sup>-3</sup>. Either of these numbers is consistent with the observed 30 meV donor concentration of about  $2 \times 10^{17}$  cm<sup>-3</sup> in the irradiated sample (see Table I), because the value  $2 \times 10^{17}$  cm<sup>-3</sup> is actually an upper limit. That is, the mobility after such a heavy irradiation is almost certainly reduced by electrical inhomogeneity, and, thus, it is artificially low, leading to artificially high donor and acceptor concentrations. However, the concentration of Zn<sub>I</sub> should still be about twice that of  $V_{\rm O}$ , and, moreover, there is abundant evidence that  $V_{\rm O}$  is a deep, not shallow, donor [7–9,26]. Thus,  $Zn_I$  is a much better candidate for the irradiation donor than  $V_{\rm O}$ . However, there also is evidence that isolated  $Zn_I$  is mobile

at room temperature, so that it likely has to form a complex to be stable [27,28].

A search for potential complexing partners for Zn<sub>I</sub> immediately suggests N, which easily substitutes for O in the ZnO lattice and which indeed has a concentration of about 10<sup>17</sup> cm<sup>-3</sup> in ZnO material of the type we are using [29]. Thus, we have examined the formation energy, binding energy, and (0/+) transition energy of the complex Zn<sub>I</sub>-N<sub>O</sub> using first principles calculations. We applied density functional theory (DFT) within the local density approximation (LDA) and used Vanderbilt-type ultrasoft pseudopotentials, as implemented in the VASP code [30]. To obtain defect formation energies, defined elsewhere [31,32], a supercell approach was used, with a ZnO supercell size of 96 atoms. The main result of the calculation is that the binding energy of the Zn<sub>I</sub>-N<sub>O</sub> complex is about 0.9 eV; thus, the complex should be stable at room temperature. The formation energies of the  $N_0$ ,  $Zn_I$ , and Zn<sub>I</sub>-N<sub>O</sub> species in ZnO depend on the Fermi energy and the partial pressures of the elements or, in other words, the chemical potentials of the elements, during growth. The secondary-ion mass-spectroscopy measurements [29] found a N concentration [N] of about  $1 \times 10^{17}$  cm<sup>-3</sup>. Based on our calculated formation energies of N<sub>O</sub>, Zn<sub>I</sub>, and Zn<sub>I</sub>-N<sub>O</sub>, together with the measured N concentration  $([N] = [N_O] + [Zn_I - N_O])$ , we estimate a N chemical potential of 0.92 eV below the N<sub>2</sub> precipitation limit (assuming Zn-rich and charge-neutral growth conditions and a growth temperature of 950 °C). The calculated formation energy [33] shows that, during growth,  $N_0^-$  acts as the dominant acceptor and  $Zn_I^{2+}$  as the dominant donor, with the Fermi energy pinned at about 1.0 eV above the valence band where the two defects have approximately the same energy, about 1.4 eV. The corresponding defect concentrations are on the order of  $10^{17}$  cm<sup>-3</sup>. The concentration of the Zn<sub>I</sub>-N<sub>O</sub> complex is about 2 orders of magnitude lower, as determined from the reaction  $N_0 + Zn_I \rightarrow$  $Zn_I-N_O + 0.9$  eV and the associated detailed-balance relationship  $[N_O][Zn_I]/N_{site}[Zn_I-N_O] = \exp(-E_b/kT)$ . Here we use  $N_{site}(ZnO) = 4.28 \times 10^{22} \text{ cm}^{-3}$  and  $E_b =$ 0.9 eV. At T = 950 °C, we get  $[Zn_I - N_O]/[Zn_I] = 0.012$ , which means that only about 1/100 of the  $Zn_I$  ions take part in formation of the complex. However, during cooldown, it is expected that the formation of the complex will accelerate, assuming a sufficiently low Zn<sub>I</sub> diffusion barrier. As the temperature cools to about 500 °C, the quantity  $[Zn_I - N_O]/[Zn_I]$  approaches unity, which means that about half of the Zn<sub>I</sub> are already bound in the com-

TABLE I. Fitting parameters for mobility and carrier concentration data.

	$E_{D1}$ (meV)	$N_{D1} (10^{16} \text{ cm}^{-3})$	$E_{D2}$ (meV)	$N_{D2} (10^{16} \text{cm}^{-3})$	$E_{D3}$ (meV)	$N_{D3} (10^{16} \text{cm}^{-3})$	$N_A (10^{16} \text{cm}^{-3})$
As-grown	30	0.45	44	3.0	75	2.0	0.13
715 °C	30	0.74			75	3.2	0.7
Irradiated	30	~20			75	0.13	~20
400 °C	30	1.35			75	0.4	1.2

plexes. At room temperature,  $[Zn_I-N_O]/[Zn_I] \approx 10^9$ , so that nearly 100% of the  $Zn_I$  are in complexes. With other impurities (such as  $H_I$ ) in the sample, the above balance conditions would vary somewhat, but the main conclusions should remain the same.

The electronic transition energy of  $Zn_I$ - $N_O$  is somewhat uncertain, due to the well-known LDA gap error. However, our calculations show that the donor level of  $Zn_I$ - $N_O$  is shallower than that of isolated  $Zn_I$ , which itself is argued to be a shallow donor [8,9]. In addition, a wave function analysis of  $Zn_I$  shows delocalization, which is characteristic of a shallow level. In short, although the (0/+) transition energy of  $Zn_I$ - $N_O$  cannot be accurately calculated, it is entirely consistent with the observed value of 30 meV. Further details of these calculations will be published elsewhere.

It is also interesting to compare the 0.9 eV binding energy with the activation energy for irradiation-defect annealing in ZnO, measured previously as 1.7 eV [34]. The difference between these two energies, 0.8 eV, should be the motional energy for  $Zn_I$  and is a reasonable value for an interstitial.

Other evidence for a  $Zn_I$ - $N_O$  complex comes from optically detected magnetic resonance experiments in epitaxial N-doped ZnO [35]. An observed spin-1/2 center was consistent with a Zn interstitial, possibly in association with an N atom, since it was not observed in a sample with lower N content. Besides  $Zn_I$ , other donors, such as H, are also believed to associate with N [14,36]. However, H-N would be neutral, whereas  $Zn_I$ -N has a shallow-donor level.

Finally, other  $Zn_I$ -acceptor complexes that behave as shallow donors are also predicted to be stable. For example, very recently Wardle *et al.* [37] have used DFT to show that  $Zn_I$ -Li<sub>Zn</sub> is bound by 0.7 eV and has a shallow-donor transition. This result further strengthens and generalizes our assertion that  $Zn_I$ -related shallow donors can exist and be important in as-grown ZnO.

In summary, we have carried out extensive lowphotoluminescence temperature and temperaturedependent Hall-effect measurements on irradiated ZnO and have identified a defect-related donor at about 30 meV, which also exists in as-grown ZnO. We have further carried out molecular dynamics simulations, to show that the expected production rate of  $Zn_I$  is consistent with the concentrations of the 30 meV donor after irradiation, and density functional calculations to show that the  $Zn_I - N_O$  defect complex is a shallow donor with a sufficient binding energy to explain the annealing data. Thus, the conclusion is that native-defect-related donors can exist in *n*-type ZnO and contribute to its conductance.

D. C. L. and G. C. F. were supported by U.S. Air Force (F33615-00-C-5402), ARO (W911NF05C0024), SVTA, Inc., and Structured Materials Industries, Inc. (41471-010605-01). P. R. and S. L. were supported by AFOSR/AOARD (FA5209-05-P-0309) and TRF (BRG4880015 and PHD/0203/2546). Work at NREL was supported by DOE/BES and EERE (DE-AC36-99GO10337).

- [1] D.C. Look, Mater. Sci. Eng. B 80, 383 (2001).
- [2] S. J. Pearton et al., Prog. Mater. Sci. 50, 293 (2005).
- [3] P. Wagner and R. Helbig, J. Phys. Chem. Solids 35, 327 (1974).
- [4] D.C. Look *et al.*, Solid State Commun. **105**, 399 (1998).
- [5] F. A. Kröger, *The Chemistry of Imperfect Crystals* (North-Holland, Amsterdam, 1964).
- [6] D. C. Look, J. W. Hemsky, and J. R. Sizelove, Phys. Rev. Lett. 82, 2552 (1999).
- [7] A. F. Kohan et al., Phys. Rev. B 61, 15019 (2000).
- [8] F. Oba et al., J. Appl. Phys. 90, 824 (2001).
- [9] S. B. Zhang, S.-H. Wei, and A. Zunger, Phys. Rev. B 63, 075205 (2001).
- [10] C.G. Van de Walle, Phys. Rev. Lett. 85, 1012 (2000).
- [11] S. F. J. Cox et al., Phys. Rev. Lett. 86, 2601 (2001).
- [12] D.M. Hofmann *et al.*, Phys. Rev. Lett. **88**, 045504 (2002).
- [13] K. Shimomura, K. Nishiyama, and R. Kadono, Phys. Rev. Lett. 89, 255505 (2002).
- [14] N. H. Nickel and K. Fleischer, Phys. Rev. Lett. 90, 197402 (2003).
- [15] K. Ip et al., Appl. Phys. Lett. 82, 385 (2003).
- [16] Y. M. Strzhemechny et al., Appl. Phys. Lett. 84, 2545 (2004).
- [17] ZN Technology, 910 Columbia Street, Brea, CA 92821, USA.
- [18] B. K. Meyer et al., Phys. Status Solidi B 241, 231 (2004).
- [19] D. C. Look et al., Phys. Status Solidi A 195, 171 (2003).
- [20] D. C. Look, Semicond. Sci. Technol. 20, S55 (2005).
- [21] D. C. Look and R. J. Molnar, Appl. Phys. Lett. 70, 3377 (1997).
- [22] J. Nord, K. Nordlund, and J. Keinonen, Phys. Rev. B 68, 184104 (2003).
- [23] P. Erhart, K. Albe, N. Juslin, and K. Nordlund (to be published).
- [24] J. Nord et al., J. Phys. Condens. Matter 15, 5649 (2003).
- [25] F. Agullo-Lopez, C. R. A. Catlow, and P. D. Townsend, Point Defects in Materials (Academic, New York, 1988).
- [26] P. Kasai, Phys. Rev. 130, 989 (1963).
- [27] Yu. V. Gorelkinskii and G. D. Watkins, Phys. Rev. B 69, 115212 (2004).
- [28] C. Coşkun et al., Semicond. Sci. Technol. 19, 752 (2004).
- [29] D.C. Look et al., Appl. Phys. Lett. 81, 1830 (2002).
- [30] G. Kresse and J. Furthmüller, Comput. Mater. Sci. 6, 15 (1996).
- [31] S. B. Zhang and J. E. Northrup, Phys. Rev. Lett. 67, 2339 (1991).
- [32] S. Limpijumnong et al., Phys. Rev. Lett. 92, 155504 (2004).
- [33] See EPAPS Document No. E-PRLTAO-030548 for the calculated defect formation energy. This document can be reached via a direct link in the online article's HTML reference section or via the EPAPS homepage (http:// www.aip.org/pubservs/epaps.html).
- [34] D. C. Look et al., Appl. Phys. Lett. 75, 811 (1999).
- [35] G. N. Aliev et al., Phys. Rev. B 70, 115206 (2004).
- [36] N. Ohashi et al., J. Appl. Phys. 93, 6386 (2003).
- [37] M. G. Wardle, J. P. Goss, and P. R. Briddon, Phys. Rev. B 71, 155205 (2005).

# Identification of Mn site in $Pb(Zr,Ti)O_3$ by synchrotron x-ray absorption near-edge structure: Theory and experiment

Sukit Limpijumnong, a) Saroj Rujirawat, and Adisak Boonchun National Synchrotron Research Center, Nakhon Ratchasima 30000, Thailand and School of Physics, Suranaree University of Technology, Nakhon Ratchasima 30000, Thailand

#### M. F. Smith

National Synchrotron Research Center, Nakhon Ratchasima 30000, Thailand

#### B. Cherdhirunkorn

Department of Physics, Thammasat University, Patum Thani 12121, Thailand

(Received 9 January 2007; accepted 31 January 2007; published online 8 March 2007)

Synchrotron x-ray absorption near-edge structure (XANES) experiments are performed on Mn-doped PbZr $_{1-x}$ Ti $_x$ O $_3$  samples (PZT) and compared with first-principles XANES simulations. The features of the measured Mn K-edge XANES are consistent with the first-principles XANES of Mn on the Ti/Zr site and inconsistent with Mn on other sites. The clear agreement between measured and first-principles theoretical XANES spectra reported here is by far the strongest evidence of Mn substituting for Ti/Zr in PZT. This work illustrates that a first-principles supercell framework, which is popularly used to study impurities in crystals, can be used in conjunction with XANES measurement in order to identify an impurity structure with a high degree of confidence. This approach may thus be broadly applicable to study impurities in other crystals. © 2007 American Institute of Physics. [DOI: 10.1063/1.2711200]

X-ray absorption spectroscopy (XAS) is a very powerful technique for resolving the local structure surrounding a particular (absorbing) atom. Traditionally, XAS is divided into two regions: (1) the low energy region, which covers photon energy up to about 50 eV above the absorption edge, called the x-ray absorption near-edge structure (XANES), and (2) the higher energy region from 50 to ~ 1000 eV above the absorption edge, called the extended x-ray absorption fine structure (EXAFS). While both regions of XAS contain information on the arrangement of the neighboring atoms surrounding the absorbing atom, the theory of the interpretation of EXAFS spectra is better known. Therefore, EXAFS is more frequently utilized than XANES. However, EXAFS suffers from lower sensitivity, which makes it difficult to obtain clear signals for dilute element in crystals. Moreover, since EXAFS is dominated by electron scattering processes, it lacks the ability to distinguish neighbors with similar size, and the dependences on the size and on the number of neighbors are difficult to separate. While the interpretation of XANES is more difficult, the information on the arrangement of neighboring atoms contained in XANES is no less extensive than that contained in EXAFS. It is also strongly sensitive to the chemical and coordination of the neighbors. Starting from the 1990s, first-principles XANES simulation work based on electron wave functions of several binary compounds (including oxides) as well as liquid was calculated and shown to independently reproduce both cation- and anion-XANES features observed for many materials very well (see, e.g., Refs. 2–4). Therefore, the first-principles approach is a feasible way to translate XANES data into a model of the local structure around the absorbing atom.

Despite the success of XANES in compounds, using XANES to probe the location of *an impurity* in a crystal is a much more challenging task both experimentally and

Piezoelectric ceramics are used extensively in a variety of devices, e.g., high-voltage high-power generators and sensors. Ref. PZT has a rich structural phase diagram, which underlies the complex dependence of its electronic properties on chemical doping. There have been many attempts made to modify the piezoelectric response and other properties of PZT using various types of impurities (see, e.g., Refs. 16–19). Typically, donors, when substituting for cation sites, i.e., either Pb or Ti/Zr, tend to increase the piezoelectric coupling constant (as well as affect other electric properties) whereas acceptors tend to reduce this couplingconstant. One dopant that has been the subject of interest is Mn. Ref. The role of Mn (as a donor or acceptor) in PZT is currently unclear. For instance, based on electron paramag-

computationally.5 XANES measurements of impurities generally require both (1) a strong continuous-spectrum x-ray source, which is available only at synchrotron facilities, and (2) a highly sensitive (fluorescence mode) multicomponent detector. Regarding computation, calculations of a diluted impurity system require a supercell containing at least a few tens of host atoms making it so computationally demanding that only in the last decade have such calculations become routine. To simulate XANES, a large number of unoccupied conduction states are also needed, further increasing computational demand. It is very important to note that, while such calculations are clearly feasible by modern standards, simulating XANES of impurities in crystals by this approach is not well known. For example, recent works use the firstprinciples supercell approach to study impurity and obtain accurate atomic structure. However, instead of directly simulating the XANES spectrum from the calculated electron wave functions, a multiple-scattering approach was used.<sup>6,7</sup> Here we illustrate our point by carrying out a combined experimental and theoretical study of the XANES spectrum of an impurity in a host crystal. The system we choose to study is the piezoelectric ceramic  $PbZr_{1-x}Ti_xO_3$  (henceforth PZT) doped with a low concentration of Mn.

a) Electronic mail: sukit@sut.ac.th

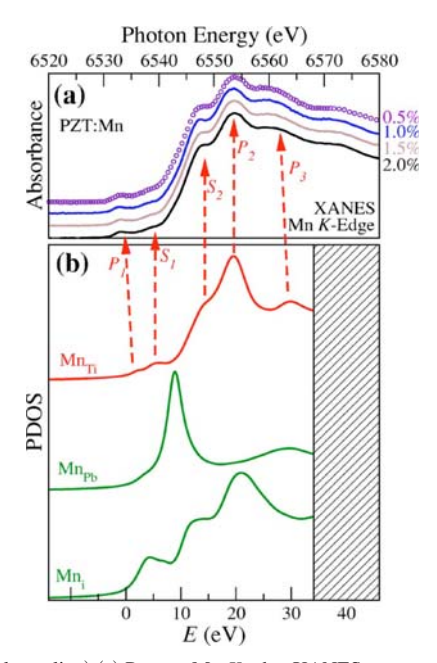


FIG. 1. (Color online) (a) Present Mn K-edge XANES spectra of Mn-doped PZT. (b) Calculated Mn site and angular momentum (l=1) projected PDOSs for Mn<sub>Ti</sub>, Mn<sub>Pb</sub>, and Mn<sub>i</sub>. For Mn<sub>Ti</sub> and Mn<sub>pb</sub>, neutral charge state is assumed whereas 3+ charge state is assumed for Mn<sub>i</sub>. PDOSs are broadened by a Lorentzian with full width at half maximum=2.0+0.15(E-E<sub>F</sub>) eV to account for the lifetime broadening of initial and final states.

netic resonance experiment, He and Li believed that Mn can occupy either Pb site (*A* site) or Ti/Zr site (*B* site) depending on Mn concentration. However, first-principles calculations show, based on energetics, that Mn will predominantly occupy the *B* site in all equilibrium growth conditions. Besides the role of modifying the piezoelectric coupling, the spin properties of Mn could potentially endow PZT with tunable magnetic properties. At this point, it is crucial to identify the site of Mn in the actual sample so that further research can be confidently and correctly carried out.

The PZT samples used in this study were prepared and doped via a conventional method of mixing oxides (see Ref. 23). The samples had a Ti/Zr ratio of 44/56 and had Mn concentrations of 0.5, 1.0, 1.5, and 2.0 mol %.

In this letter, we identify the lattice location of the Mn atom in these PZT samples by both performing XANES experiments and independently calculating first-principles XANES with Mn at different lattice locations. The results show that the measured XANES is clearly consistent with the calculation of Mn on Ti/Zr site and inconsistent with Mn at other lattice locations. XANES of Mn K edge [data shown as Fig. 1(a)] was performed in a fluorescent mode at Station 7.1, Synchrotron Radiation Source (SRS), Daresbury, United Kingdom. X rays were monochromatized by a Si(111) double crystal. The fluorescence detection system consists of an array of nine high-purity germanium diodes mounted in a common cryostat. To do fluorescence measurements, the sample was aligned at 45° to the line of the beam, in order to maximize the solid angle seen by the detector. Because of the high absorbance of the Pb atoms, the multicomponent fluorescent detector was needed to improve the XANES signal.

The XANES spectrum can be simulated using the unoccupied electronic states of the system under study, as described below. For a crystal containing an impurity, it is standard practice to calculate the electronic states of the system Downloaded 08 Mar 2007 to 128.111.119.100. Redistribution subject to AIP license or copyright, see http://apl.aip.org/apl/copyright.jsp

using first-principles methods based on a supercell approach (see, e.g., Refs. 24 and 25). The x-ray absorbance  $\mu(\omega)$  is given by Fermi's golden rule as

$$\mu \propto \sum_{f} |\langle f|D|i\rangle|^2 \delta(E_i - E_f + \omega),$$
 (1)

where  $|i\rangle$ ,  $|f\rangle$ ,  $E_i$ , and  $E_f$  are the initial and final states and their energies, respectively;  $\omega$  and D are the photon frequency and dipole operator. For K-edge, the initial state of the photoelectron is the core 1s state, i.e.,  $|i\rangle = |1s\rangle$ , so the dipole-allowed final states have the symmetry of atomic p states (l=1). Since the initial state is localized at the absorbing atom, only the final state wave function in the vicinity of the absorber is relevant. It thus turns out that the angular-momentum and site projected partial density of empty states, with some broadening, resembles the XANES absorption spectra<sup>26</sup> and has been used frequently to compare with measurements.<sup>27</sup> For simplicity, we calculate the density of final states using full ground state electron occupation.

Figure 1(a) shows the normalized Mn K-edge XANES spectra measured from four PZT:Mn samples with the Mn concentrations of 0.5%, 1.0%, 1.5%, and 2.0%, respectively. The fact that all four spectra contain the same main features implies that the majority of Mn atoms assume the same lattice locations in these samples. The XANES spectra have the preedge peaks at 6533 eV  $(P_1)$  and 6539 eV (the second preedge peak merged into the edge and appears only as an onset in the slope of the edge; labeled as  $S_1$ ). The main feature in the spectra is composed of the main peak at 6553 eV  $(P_2)$ , with a lower energy shoulder at 6547 eV  $(S_2)$ , and followed by another peak at 6361 eV  $(P_3)$  which is smaller and broader. Note that, while the noise is slightly increased in the low concentration cases, the features, even in our lowest concentration spectrum, are still very clear. This emphasizes the high sensitivity of the technique, making it suitable for even lower concentration samples.

To identify the lattice location of the Mn atoms, independent first-principles calculations of Mn at several lattice locations are carried out using the so-called supercell approach with the supercell size of 40 atoms. The converged electron wave functions, obtained from the calculation of Mn at each lattice location (with all atoms in the supercell allowed to relax) are then used to calculate the site (radius=1.3 Å around Mn atom) and angular-momentum (l=1) projected partial density of states (PDOS) that can be directly compared with the measured XANES. Our first-principles framework is based on density functional theory within the local density approximation. We employ (ultrasoft) pseudopotential with a plane wave basis set as implemented in the VASP code. Details of the calculations are the same as in Ref. 22; however, over 400 unoccupied bands are included in the calculations here, so that the PDOS can be reliably generated up to 35 eV above the valence band maximum.

In the PZT perovskite structure, as shown in Fig. 2, there are three potential Mn sites, Mn substituting on the Pb site (Mn<sub>Pb</sub>, also known as A site), Mn substituting on the Ti/Zr site (Mn<sub>Ti/Zr</sub>, also known as B site), and Mn interstital (Mn<sub>i</sub>).<sup>22</sup> Note that we studied Mn in PbTiO<sub>3</sub> and PbZrO<sub>3</sub> (henceforth, PT and PZ) instead of in a random PZT alloy, which would have a much higher computational demand. This is expected to be a good approximation since none of the Mn sites under investigation have Ti/Zr as the nearest neighbor. Mn<sub>Pb</sub> and Mn<sub>Ti/Zr</sub> are surrounded by only O atoms

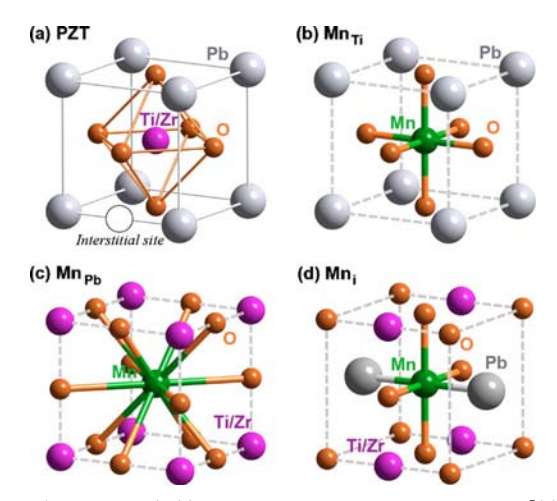


FIG. 2. (Color online) (a) Perovskite crystal structure of PZT. [(b)-(d)] Schematic illustrations of Mn on Ti/Zr site, Mn on Pb site, and interstitial Mn, respectively. Regions shown in (c) and (d) are shifted from that in (a).

[Figs. 2(b) and 2(c)] whereas Mn; is surrounded by O and Pb atoms [Fig. 2(d)]. The calculated PDOSs of Mn in PZ and PT are indeed very similar. Thus, for convenience, we choose to present only the PDOS of Mn in PT. The slight difference in PDOS obtained from Mn in PT and PZ arises mainly from the small difference in the host lattice constants.

The calculated PDOSs for Mn<sub>Ti</sub>, Mn<sub>Ph</sub>, and Mn<sub>i</sub> are shown in Fig. 1(b). It is clear from inspection of the figure that the PDOS of Mn<sub>Ti</sub> matches very well the measured XANES. On the other hand, the PDOS of Mn<sub>Pb</sub> can be clearly ruled out and the Mn<sub>i</sub> simulation bears only a slight resemblance to the measured XANES. All the key features of the measured XANES have counterparts in the Mn<sub>Ti</sub> PDOS, as illustrated by the arrows in the figure. Not only are the overall spectra qualitatively similar but the energy differences between prominent features are in quantitative agreement: the separation between  $P_2$  and  $P_1$  in the measured XANES is  $E(P_2)-E(P_1)=20$  eV, whereas the calculated PDOS gives 17 eV. Reasonable agreement also observed for the separation of  $P_3$  and  $P_2$ , i.e.,  $E(P_3) - E(P_2) = 8$  eV (measured) and 10 eV (calculated).

Looking closely at the region between  $S_1$  and  $S_2$ , one can see that  $S_1$  in the PDOS has a clearer separation from  $S_2$  than is seen in the measured XANES. This difference might be an indication that a small fraction of Mn<sub>Ph</sub>, which has its main peak in this region, is also present in the sample. A small amount of Mn<sub>Pb</sub> will lead to an increase in the absorption around this region, which would tend to blur  $S_1$  into  $S_2$  as observed in the measured XANES.

It should be emphasized that while the evidence for minority occupation of MnPb may be questionable, the conclusion that the majority of Mn in PZT occurs as Mn<sub>Ti/Zr</sub> is solidly supported both by the analysis above and by energetic considerations based on first-principles calculations. Indeed, in agreement with our finding, the formation energy of Mn on the Ti/Zr sites has been found to be lower than that on other sites in all possible equilibrium growth conditions, e.g., Mn<sub>Ti</sub> can be 1.6-4.8 eV lower than Mn<sub>Pb</sub>, depending on growth conditions.2

In conclusion, we have unambiguously identified the lattice location of Mn atoms in PZT by XANES experiment. Our observed Mn K-edge XANES spectrum clearly matches our independent first-principles XANES simulation of a Mn atom substituting for Ti/Zr, indicating that almost all of Mn atoms are occupying the Ti/Zr site (also known as B site). The small differences between the measured and calculated XANESs are compatible with the presence of a small amount of Mn atoms substituting for Pb. This work illustrates that the combination of XANES measurements and firstprinciples supercell simulations is a very powerful way to unambiguously identify structures of an impurity in a crystal, which is a topic of immense interest over a broad range of materials science.

One of the authors (S.L.) acknowledges W. R. L. Lambrecht for constructive suggestions. Another author (B.C.) acknowledges D. A. Hall for his assistance and SRS for the beam time. This work is supported by the Thailand Research Fund (No. BRG4880015) and NANOTEC (No. NN49-024).

<sup>1</sup>D. C. Koningsberger and R. Prins, X-ray Absorption: Principles, Applications, Techniques of EXAFS, SEXAFS, and XANES (Wiley, New York, 1988), Vol. 92, pp. 3-4, 53.

<sup>2</sup>D. Prendergast and G. Galli, Phys. Rev. Lett. **96**, 215502 (2006).

<sup>3</sup>I. Tanaka and H. Adachi, Phys. Rev. B **54**, 4604 (1996); T. Mizoguchi, I. Tanaka, S. Yoshioka, M. Kunisu, T. Yamamoto, and W. Y. Ching, ibid. 70, 045103 (2004).

<sup>4</sup>C. L. Dong, C. Persson, L. Vayssieres, A. Augustsson, T. Schmitt, M. Mattesini, R. Ahuja, C. L. Chang, and J.-H. Guo, Phys. Rev. B 70, 195325

<sup>5</sup>S. Limpijumnong, M. F. Smith, and S. B. Zhang, Appl. Phys. Lett. 89, 222113 (2006).

<sup>6</sup>P. Fons, H. Tampo, A. V. Kolobov, M. Ohkubo, S. Niki, J. Tominaga, R. Carboni, F. Boscherini, and S. Friedrich, Phys. Rev. Lett. 96, 045504 (2006).

<sup>7</sup>G. Ciatto, F. Boscherini, A. A. Bonapasta, F. Filippone, A. Polimeni, and M. Capizzi, Phys. Rev. B 71, 201301 (2005).

<sup>8</sup>S. B. Lang, Phys. Today **58**(8), 31 (2005).

<sup>9</sup>L. E. Cross, Ferroelectric Ceramics: Tailoring Properties for Specific Application (Birkhauser, Basel, 1993).

10J. F. Scott, Ferroelectric Memories (Springer, Berlin, 2000).

<sup>11</sup>B. Jaffe, W. R. Cook, and H. Jaffe, *Piezoelectric Ceramics* (Academic, New York, 1971).

<sup>12</sup>B. Noheda, J. A. Gonzalo, L. E. Cross, R. Guo, S.-E. Park, D. E. Cox, and G. Shirane, Phys. Rev. B 61, 8687 (2000).

<sup>13</sup>B. Noheda and D. E. Cox, Phase Transitions **79**, 5 (2006).

<sup>14</sup>R. Guo, L. E. Cross, S.-E. Park, B. Noheda, D. E. Cox, and G. Shirane, Phys. Rev. Lett. 84, 5423 (2000).

<sup>15</sup>L. Bellaiche, A. Garcia, and D. Vanderbilt, Phys. Rev. Lett. **84**, 5427 (2000).

<sup>16</sup>E. Boucher, D. Guyomar, L. Lebrun, B. Guiffard, and G. Grange, J. Appl. Phys. 92, 5437 (2002).

<sup>17</sup>Z. Xu, X. Dai, and D. Viehland, Phys. Rev. B **51**, 6261 (1995).

<sup>18</sup>J. Frantti, V. Lantto, S. Nishio, and M. Kakihana, Phys. Rev. B 59, 12

<sup>19</sup>I. Franke, K. Roleder, L. Mitoseriu, R. Pitescu, and Z. Ujma, Phys. Rev. B 73, 144114 (2006).

<sup>20</sup>M. D. Glinchuk, T. P. Bykov, V. M. Kurliand, M. Boudys, T. Kala, and K. Nejezchleb, Phys. Status Solidi A 122, 341 (1990).

<sup>21</sup>L. X. He and C. E. Li, J. Mater. Sci. **35**, 2477 (2004).

<sup>22</sup>A. Boonchun, M. F. Smith, B. Cherdhirunkorn, and S. Limpijumnong, J. Appl. Phys. (in press)

<sup>23</sup>D. A. Hall, A. Steuwer, B. Cherdhirunkorn, T. Mori, and P. J. Withers, J. Appl. Phys. 96, 4245 (2004).

<sup>24</sup>C. G. Van de Walle, S. Limpijumnong, and J. Neugebauer, Phys. Rev. B **63**, 245205 (2001).

<sup>25</sup>S. Limpijumnong, S. B. Zhang, S.-H. Wei, and C. H. Park, Phys. Rev. Lett. 92, 155504 (2004).

<sup>26</sup>P. Ravindran, A. Kjekshus, H. Fjellvåg, A. Delin, and O. Eriksson, Phys. Rev. B 65, 064445 (2002).

<sup>27</sup>T. Mizoguchi, I. Tanaka, S. Yoshioka, M. Kunisu, T. Yamamoto, and W. Y. Ching, Phys. Rev. B 70, 045103 (2004).

# Identification of acceptor states in Li-doped p-type ZnO thin films

Y. J. Zeng, Z. Z. Ye, a) J. G. Lu, W. Z. Xu, L. P. Zhu, and B. H. Zhao State Key Laboratory of Silicon Materials, Zhejiang University, Hangzhou 310027, People's Republic of China

#### Sukit Limpijumnong

School of Physics, Suranaree University of Technology, Nakhon Ratchasima 30000, Thailand and National Synchrotron Research Center, Nakhon Ratchasima 30000, Thailand

(Received 1 May 2006; accepted 5 June 2006; published online 25 July 2006)

We investigate photoluminescence from reproducible Li-doped *p*-type ZnO thin films prepared by dc reactive magnetron sputtering. The Li<sub>Zn</sub> acceptor state, with an energy level located at 150 meV above the valence band maximum, is identified from free-to-neutral-acceptor transitions. Another deeper acceptor state located at 250 meV emerges with the increased Li concentration. A broad emission centered at 2.96 eV is attributed to a donor-acceptor pair recombination involving zinc vacancy. In addition, two chemical bonding states of Li, evident in x-ray photoelectron spectroscopy, are probably associated with the two acceptor states observed. © 2006 American Institute of Physics. [DOI: 10.1063/1.2236225]

Research activity on ZnO has increased over the past few years, with particular interest in potential optoelectronic applications. This is because of its large exciton binding energy of 60 meV and the availability of large-area ZnO substrates. However, the realization of p-type ZnO has proven difficult due to the asymmetric doping limitations, and currently is the bottleneck in the development of ZnO-based devices. The optimal choice of acceptor species remains to be determined, with a number of candidates receiving particular attention. N substituting for O appears promising.<sup>2-5</sup> Other group-V dopants with large size mismatches, such as P and As, have also been explored. 6-8 Group-I species substituting for Zn, such as Li<sub>Zn</sub>, are theoretically predicted to have a shallow acceptor level. However, more detailed theoretical calculations give different sentiments toward the outlook of Li-doped ZnO. On a positive side, Lee and Chang proposed that H can help to increase the solubility of Li and subsequent H removal can potentially result in low-resistivity p-type ZnO.<sup>10</sup> On a negative side, Wardle et al. suggested that p-type doping may be limited by the formation of complexes, such as Li<sub>Zn</sub>-Li<sub>i</sub>, Li<sub>Zn</sub>-H, and Li<sub>Zn</sub>-AX. 11 In our previous studies, we have demonstrated the growth of p-type ZnO thin films by Li doping. <sup>12,13</sup> In this letter, we use a combination of photoluminescence (PL) and x-ray photoelectron spectroscopy (XPS) to shed more light on the role of Li in *p*-type ZnO.

Li-doped ZnO thin films were grown on glass substrates by dc reactive magnetron sputtering method. The detailed growth procedures were published elsewhere. <sup>12,13</sup> A series of sputtering targets with different Li contents, namely, 0.1, 0.5, 1, and 2 at. %, was employed in this study, and henceforth the ZnO thin films grown using these sputtering targets will be referred to as ZnO:Li<sub>0.001</sub>, ZnO:Li<sub>0.005</sub>, ZnO:Li<sub>0.01</sub>, and ZnO:Li<sub>0.02</sub>, respectively. All samples were deposited at an optimal substrate temperature of 550 °C. Room temperature Hall-effect measurements were carried out in the van der Pauw configuration (Bio-Rad HL5500PC). Temperature-

dependent PL measurements were performed on a Fluorolog-3-Tau fluorescence spectrometer. The chemical states of Li in ZnO were analyzed by XPS using an Omicron EAC2000-125 hemispherical analyzer.

The results of Hall-effect measurements are summarized in Table I. Low-resistivity p-type conductivity can only be achieved in the  $ZnO:Li_{0.001}$  samples. The optimal results include a resistivity of 16.4  $\Omega$  cm, a Hall mobility of 2.65 cm<sup>2</sup>/V s, and a hole concentration of  $1.44 \times 10^{17}$  cm<sup>-3</sup> with very reproducible characteristics. Samples with high Li contents, i.e., ZnO:Li $_{0.005}$ , ZnO:Li $_{0.01}$ , and ZnO:Li $_{0.02}$  have high resistivity, low carrier concentration, and low Hall mobility. For these high Li-content samples, the electrical properties are insensitive to the magnitude of Li. Note that Halleffect measurements on the high-resistivity samples can result in ambiguous determination of carrier type, due to their low Hall mobility and low carrier concentration. Similar noise signal for ZnO has also been observed and treated as p type. <sup>14</sup> On the other hand, the low-resistivity samples with a hole concentration above 1017 cm-3 always give a definitive p-type signal. In our previous study, the degradation of p-type conductivity in our higher Li-content samples has been tentatively ascribed to the formation of Li, or  $\text{Li}_{Zn}$ - $\text{Li}_i$  complex.<sup>12</sup>

To gain more information on the *p*-type doping mechanism of Li, temperature-dependent PL measurements were performed. Figure 1(a) shows the PL spectrum at 8 K for the low-resistivity ZnO:Li<sub>0.001</sub> sample. The spectrum consists of three bands centered at 3.35, 3.28, and 2.96 eV, labeled as A,

TABLE I. Electrical properties of Li-doped ZnO thin films grown with different Li contents.

Sample	Resistivity $(\Omega \text{ cm})$	Hall mobility (cm²/V s)	Carrier concentration (cm <sup>-3</sup> )	Carrier type
ZnO:Li <sub>0.001</sub>	16.4	2.65	$1.44 \times 10^{17}$	p
ZnO: Li <sub>0.005</sub>	$2.23 \times 10^{3}$	1.08	$1.68 \times 10^{15}$	p
$ZnO:Li_{0.01}$	$3.95 \times 10^{3}$	0.83	$1.23 \times 10^{15}$	p
ZnO:Li <sub>0.02</sub>	$7.05 \times 10^{3}$	0.66	$1.34 \times 10^{15}$	p

a) Author to whom correspondence should be addressed; electronic mail: yezz@zju.edu.cn

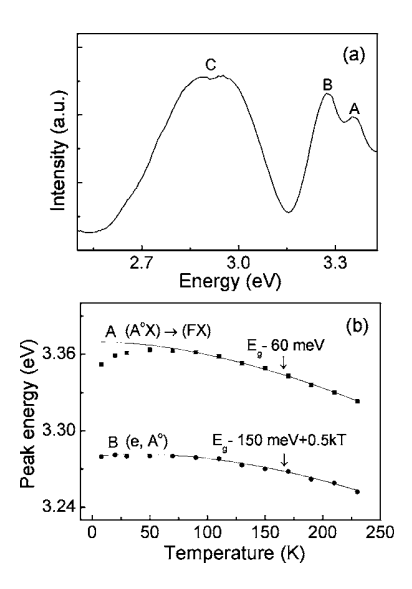


FIG. 1. (a) PL spectrum at 8 K for the ZnO: $\text{Li}_{0.001}$  thin film. (b) Temperature-dependent peak positions and their fitting curves for peaks A and B in (a).

B, and C, respectively. We tentatively assign band A to a neutral acceptor-bound exciton emission  $(A \circ X)$  and band B to a free-to-neutral-acceptor  $(e, A \circ)$  transition.

To support our assignment, we analyze the temperature-dependent peak positions of the two bands [Fig. 1(b)]. For band A, an obvious temperature-dependent blueshift from 3.35 eV at 8 K to 3.36 eV at 70 K is observed. We believed that this blueshift is a result of a transition from bound excition emission to free exciton (FX) emission as temperature increases. A similar transition has also been observed in GaN. <sup>15</sup> In higher temperature range (70–230 K), peak A shows a clear FX characteristic with the typical exciton binding energy of 60 meV. As can be seen in Fig. 1(b), the energy of peak A fits well with a curve of  $E_g(T)$ –60 meV. The temperature-dependent band gap is described according to Ref. 16 as

$$E_{o}(T) = E_{o}(0) - \alpha T^{2}/(T + \beta),$$
 (1)

where  $\alpha$  and  $\beta$  are constants and T is temperature. Note that we cannot totally exclude a possibility that the 3.35 eV emission might be a neutral donor-bound exciton emission  $(D^{\circ}X)$ . However, considering the low background electron concentration of mid- $10^{16}$  cm<sup>-3</sup> (Ref. 12) and the definitive p-type signals for this sample, it is more likely that this peak comes from  $(A^{\circ}X)$  emission.

The temperature dependence of a peak B position fits well in an equation for an  $(e,A^{\circ})$  transition given by

$$E_{eA}(T) = E_g - E_A + k_B T/2,$$
 (2)

where  $E_{eA}(T)$  is the temperature-dependent  $(e,A^\circ)$  transition energy,  $E_A$  is the acceptor energy level, and  $k_B$  is the Boltzmann constant. The acceptor energy level is found to be 150 meV, which is slightly larger than the electrical (Hall) value from our prior work of  $110\pm10$  meV. The higher optical acceptor level (in comparison to the Hall value) is attributed to screening effects (Ref. 17) and can be seen in other semiconductors as well [e.g., GaN (Refs. 18 and 19)]. A perfect match between the experimental values and the fitting curve supports our assignment of the  $(e,A^\circ)$  transition. Note that the  $(e,A^\circ)$  transition is absent in the nomi-Downloaded 26 Jul 2006 to 203.147.33.1. Redistribution subject to

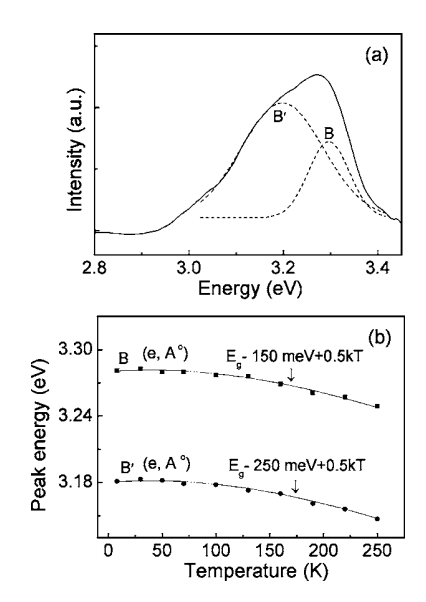


FIG. 2. (a) PL spectrum at 8 K for the  $ZnO:Li_{0.01}$  thin film. The dashed lines show the Gaussian fitting curves. (b) Temperature-dependent peak positions and their fitting curves for peaks B and B' in (a).

nally undoped ZnO sample grown under the same condition without Li doping. It is, therefore, reasonable to assume that this transition is associated with the  $\text{Li}_{\text{Zn}}$  acceptor.

The broad emission centered at 2.96 eV is believed to be a donor-acceptor pair (DAP) recombination due to its typical blueshifts with the excitation energy (data not shown). The acceptor involved in this DAP recombination is likely to be Zn vacancy due to its low formation energy. Several works also assigned emission energy in this range (e.g., 3.028 eV at 20 K<sup>22</sup> and 3.09 eV at 6 K<sup>23</sup>) to Zn vacancy. Based on these available literatures, we attribute our broad 2.96 eV emission to a DAP recombination involving zinc vacancy.

For a high-resistivity ZnO:Li<sub>0.01</sub> sample, the PL spectrum at 8 K can be deconvoluted into two peaks [Fig. 2(a)], centered at 3.28 and 3.18 eV, labeled as B and B', respectively. As shown in Fig. 2(b), both peaks have temperature dependencies fitting well in the  $(e, A^{\circ})$  transitions [Eq. (2)], with the acceptor energy levels of 150 and 250 meV.

The exciton emission and the DAP recombination (that is observed in the low-resistivity  $ZnO:Li_{0.001}$ ) disappear in the high-resistivity  $ZnO:Li_{0.01}$  sample. The absence of the exciton emission is probably due to the degradation of crystal quality in this high Li-content sample. This is consistent with the observation of the low Hall mobility (Table I). The absence of the DAP recombination can be explained by the suppression of Zn vacancy in  $ZnO:Li_{0.01}$ . In high Li-content samples, Zn vacancies are more likely to be occupied by Li, forming  $Li_{Zn}$  or  $Li_{Zn}-Li_i$  complex.

Based on the Hall-effect and PL measurements, it is demonstrated that  $\text{Li}_{\text{Zn}}$  has a shallow acceptor level as theoretically predicted, independent of the Li concentration. The high hole concentration of  $1.44 \times 10^{17}$  cm<sup>-3</sup>, combined with an  $(e, A^{\circ})$  transition located at 150 meV [illustrated both in Figs. 1(b) and 2(b)], confirms its shallow nature. Samples with high Li content, e.g.,  $\text{ZnO:Li}_{0.01}$ , show another deeper acceptor level at 250 meV. The deeper acceptor level is probably associated with complexes containing Li, such as  $\text{Li}_{\text{Zn}}-\text{Li}_i$  and  $\text{Li}_{\text{Zn}}-AX$ . This deeper 250 meV  $(e, A^{\circ})$  transition becomes dominant in the  $\text{ZnO:Li}_{0.01}$  sample, which is AIP license or copyright, see http://apl.aip.org/apl/copyright.jsp

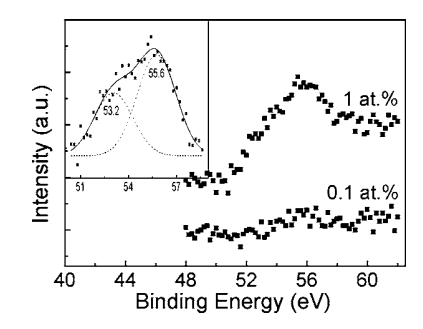


FIG. 3. XPS narrow scan spectra of Li 1s for the ZnO:Li<sub>0.001</sub> and the ZnO:Li<sub>0.01</sub> samples. The inset shows the Gaussian fitting curves for the ZnO:Li<sub>0.01</sub> thin film.

consistent with the lower hole concentration observed.

In addition to PL, the chemical bonding states of Li in ZnO were examined by XPS. Figure 3 illustrates the Li 1s narrow scan spectra for the ZnO:Li<sub>0.001</sub> and the ZnO:Li<sub>0.01</sub> samples. The former spectrum is near the noise level due to the detection limit of XPS. For the ZnO:Li<sub>0.01</sub> thin film, a peak attributed to Li 1s is observed. Gaussian fitting to the spectrum reveals two peaks centered at 53.2 and 55.6 eV, as seen from the inset in Fig. 3. These two chemical bonding states are probably associated with the two acceptor states, in agreement with our PL results in Fig. 2. Further study on their assignment is in progress.

In summary, we have demonstrated reproducible growth of Li-doped p-type ZnO thin films by dc reactive magnetron sputtering. A shallow acceptor level of 150 meV is identified from free-to-neutral-acceptor transitions and assigned to the Li<sub>Zn</sub> acceptor. Another deeper acceptor level of 250 meV, which we tentatively assign to the Li-related complexes, emerges with the increase of Li concentration. We hope that this study, together with other investigations on group-V dopants, will shed light on researches on determination of the optimal choice of acceptor species for ZnO.

This work was supported by the National Natural Sci-

ence Foundation of China under Contract Nos. 50532060 and 50572095 and by the Zhejiang Provincial Natural Science Foundation of China under Grant No. Y405126. One of the authors (S.L.) was supported by the Thailand Research Fund under Contract No. 4880015.

- B. Zhang, S. H. Wei, and A. Zunger, Phys. Rev. B 63, 075205 (2001).
   D. C. Look, D. C. Reynolds, C. W. Litton, R. L. Jones, D. B. Eason, and G. Cantwell, Appl. Phys. Lett. 81, 1830 (2002).
- <sup>3</sup>J. F. Rommeluere, L. Svob, F. Jomard, J. Mimila-Arroyo, A. Lusson, V. Sallet, and Y. Marfaing, Appl. Phys. Lett. **83**, 287 (2003).
- <sup>4</sup>W. Z. Xu, Z. Z. Ye, Y. J. Zeng, L. P. Zhu, B. H. Zhao, L. Jiang, J. G. Lu, H. P. He, and S. B. Zhang, Appl. Phys. Lett. 88, 173506 (2006).
- <sup>5</sup>A. Tsukazaki, A. Ohtomo, T. Onuma, M. Ohtani, T. Makino, M. Sumiya, K. Ohtani, S. Chichibu, S. Fuke, Y. Segawa, H. Ohno, H. Koinuma, and M. Kawasaki, Nat. Mater. 4, 42 (2005).
- <sup>6</sup>K. K. Kim, H. S. Kim, D. K. Hwang, J. H. Lim, and S. J. Park, Appl. Phys. Lett. **83**, 63 (2003).
- <sup>7</sup>D. C. Look, G. M. Renlund, R. H. Burgener, and J. R. Sizelove, Appl. Phys. Lett. **85**, 5269 (2004).
- <sup>8</sup>Y. J. Li, Y. W. Heo, Y. Kwon, K. Ip, S. J. Pearton, and D. P. Norton, Appl. Phys. Lett. 87, 072101 (2005).
- C. H. Park, S. B. Zhang, and S. H. Wei, Phys. Rev. B 66, 073202 (2002).
   E. C. Lee and K. J. Chang, Phys. Rev. B 70, 115210 (2004).
- <sup>11</sup>M. G. Wardle, J. P. Goss, and P. R. Briddon, Phys. Rev. B **71**, 155205
- <sup>12</sup>Y. J. Zeng, Z. Z. Ye, W. Z. Xu, D. Y. Li, J. G. Lu, L. P. Zhu, and B. H. Zhao, Appl. Phys. Lett. 88, 062107 (2006).
- <sup>13</sup>Y. J. Zeng, Z. Z. Ye, W. Z. Xu, L. L. Chen, D. Y. Li, L. P. Zhu, B. H. Zhao, and Y. L. Hu, J. Cryst. Growth **283**, 180 (2005).
- <sup>14</sup>D. C. Look, B. Claffin, Y. I. Alivov, and S. J. Park, Phys. Status Solidi A 201, 2203 (2004).
- <sup>15</sup>C. L. Wu, J. C. Wang, M. H. Chan, T. T. Chen, and S. Gwoa, Appl. Phys. Lett. **83**, 4530 (2003).
- <sup>16</sup>L. J. Wang and N. C. Gilesa, J. Appl. Phys. **94**, 973 (2003).
- <sup>17</sup>D. C. Look, Semicond. Sci. Technol. **20**, S55 (2005).
- <sup>18</sup>B. J. Skromme and G. L. Martinez, MRS Internet J. Nitride Semicond. Res. **5S1**, W9.8 (2000).
- <sup>19</sup>A. K. Rice and K. J. Malloy, J. Appl. Phys. **89**, 2816 (2001).
- A. F. Kohan, G. Ceder, and D. Morgan, Phys. Rev. B 61, 15019 (2000).
   F. Tuomisto, V. Ranki, K. Saarinen, and D. C. Look, Phys. Rev. Lett. 91, 205502 (2003).
- <sup>22</sup>Y. Ma, G. T. Du, S. R. Yang, Z. T. Li, B. J. Zhao, X. T. Yang, T. P. Yang, Y. T. Zhang, and D. L. Liu, J. Appl. Phys. 95, 6268 (2004).
- <sup>23</sup>S. H. Jeong, B. S. Kim, and B. T. Lee, Appl. Phys. Lett. **82**, 2625 (2003).

# Characterization of As-doped, *p*-type ZnO by x-ray absorption near-edge structure spectroscopy: Theory

Sukit Limpijumnonga)

National Synchrotron Research Center, Nakhon Ratchasima 30000, Thailand and School of Physics, Suranaree University of Technology, Nakhon Ratchasima 30000, Thailand

#### M F Smith

National Synchrotron Research Center, Nakhon Ratchasima 30000, Thailand

#### S. B. Zhang

National Renewable Energy Laboratory, Golden, Colorado 80401

(Received 9 September 2006; accepted 19 October 2006; published online 1 December 2006)

Vaithianathan *et al.* [Appl. Phys. Lett. **88**, 112103 (2006)] measured x-ray absorption near-edge structure (XANES) of As-doped ZnO and analyzed it as evidence for  $As_O$  acceptors. However, upon carrying out first principles calculations, we found that the simulated XANES spectrum for  $As_O$  is very different from that observed. Instead, the simulated spectrum for  $As_{Zn}-2V_{Zn}$  defect complex, which is predicted to be an acceptor [S. Limpijumnong *et al.*, Phys. Rev. Lett. **92**, 155504 (2004)], is far more consistent with the XANES data. The combination of our study, with the XANES of Vaithianathan *et al.* might be, until now, the strongest support for the  $As_{Zn}-2V_{Zn}$  model. © 2006 American Institute of Physics. [DOI: 10.1063/1.2398895]

The challenge of doping p-type ZnO is currently attracting wide interest and serious investigation due to the potential for ZnO to be used as a wide gap material in optoelectronic devices.<sup>1,2</sup> Based on the basic idea that a hole can be created by substituting a group-VI oxygen anion with a group-V atom, several research groups have tried to dope ZnO using group-V elements, such as N, P, As, 5,6 and Sb, with limited success. Among all group-V elements, only N has a comparable atomic radius to that of O. N is theoretically predicted to prefer to substitute for O and to have the lowest hole ionization energy in comparison with other group-V elements. Nevertheless, the ionization energy of  $N_0$  is observed to be rather deep, i.e.,  $\sim 170-200$  meV (Ref. 3), resulting in a low hole concentration. Other group-V elements have an atomic radii which is much larger than O, making it difficult for them to substitute for O in ZnO. Indeed, first principles calculations show that larger group-V atoms (P, As, and Sb) prefer to substitute for Zn rather than O. 9,10 Even if they can somehow be forced to substitute for O, their ionization energies (in the order of 1000 meV) are much too large to result in any detectable holes.

In spite of such unpromising theoretical predictions, several recent experiments have shown success in doping p-type ZnO using large-size group-V elements X=(P,As, and Sb). Recently, based on first principles calculations, the puzzling p doping in these cases has been assigned to the  $X_{\rm Zn}-2V_{\rm Zn}$  complexes, which have a calculated hole ionization energy of  $\sim$ 200 meV. The formation of the  $As_{\rm Zn}-2V_{\rm Zn}$  complex occurs because the As energetically prefers to substitute Zn  $(As_{\rm Zn})$  and subsequently induces and binds two Zn vacancies  $(V_{\rm Zn})$  to form an  $As_{\rm Zn}-2V_{\rm Zn}$  complex, which is a moderately shallow single acceptor and likely responsible for p-type conductivity. Recently, there are several experiments that, in various aspects, support this complex model. At this point, it is very beneficial to know whether the observed p-type conductivity is a result of the formation of  $As_{\rm Zn}-2V_{\rm Zn}$ 

X-ray absorption spectroscopy (XAS) can selectively excite core electrons of a particular element (in this case, As) to unoccupied (and symmetry permitted) high energy states. XAS is generally used to obtain information about the arrangement of atoms in the locality of the absorbing atom and is made available by the high x-ray photon flux from synchrotron sources. It is a very powerful technique to directly gain information about the site and neighborhood of the As in ZnO.

XAS can be divided into two regions: the x-ray absorption near-edge structure (XANES) and the extended x-ray absorption fine structure (EXAFS). The XANES region corresponds to the excitation of a core electron to unoccupied bound states or low lying continuum states, typically covering up to 40-50 eV above the absorption edge, whereas the EXAFS region covers the higher energy regime and extends typically to  $\sim 1000$  eV above the edge. <sup>14</sup> In the EXAFS region, the highly energetic excited electron may be treated as a nearly free electron, and its interaction with surrounding atoms included perturbatively. Information about the arrangement of atoms is obtained by analyzing possible scattering processes of the excited electron from nearby ions. This (multiple) scattering theory is rather well developed and can be conveniently used to analyze and interpret EXAFS spectra and thus determine the local atomic arrangement. This fact makes EXAFS the preferred, and more generally used, probe of local structure. However, EXAFS requires a much higher concentration of absorbing atoms than XANES. In many cases of interest, especially those involving samples with dilute impurities like the case at hand, only XANES data can generally be obtained.

In the XANES region, core electrons are promoted into symmetry-allowed unoccupied bound states or low lying continuum states, which are unoccupied defect states and conduction band states in semiconductors. While these states

complex as theoretically predicted or a result of a well known, though theoretically unsupported,  $As_O$  model, so that the optimization of the doping procedure can be planned accordingly.

a) Electronic mail: sukit@sut.ac.th

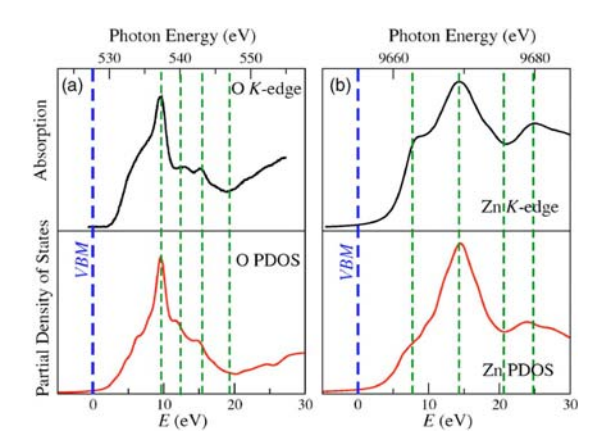


FIG. 1. (Color online) (a) (Top) the O K-edge XANES spectrum of bulk ZnO taken from Ref. 1. (Bottom) our calculated O-site and angular-momentum (l=1) projected PDOSs of bulk ZnO. (b) (Top) the Zn K-edge XANES spectrum of bulk ZnO taken from Ref. 18. (Bottom) calculated Zn-site and angular-momentum (l=1) projected PDOS. The PDOS are broadened by a Lorentzian [full width at half maximum (FWHM)=1.0 +0.05(E- $E_F$ ) eV for O PDOS and FWHM=1.0+0.1(E- $E_F$ ) eV for Zn PDOS] to account for the lifetime broadening of both initial and final states.

are sensitive to the arrangement of atoms around the absorbing atom (so that photon absorption involving these states relates sensitively on detailed local structure), deciphering out the atomic arrangement from XANES is not trivial. To our knowledge, there is no direct way to convert XANES into atomic arrangement. One must compare the observed signal with simulations based on various models of atomic configuration and seek the best match.

For a given atomic configuration, the XANES spectrum can be simulated from the electronic band structures, calculated up to a few tens of eV above the Fermi level  $E_F$ . The x-ray absorbance  $\mu(\omega)$  is given by Fermi's golden rule as

$$\mu \propto \sum_{f} |\langle f | \mathsf{D} | i \rangle|^2 \delta(E_i - E_f + \omega), \tag{1}$$

where  $|i\rangle$ ,  $|f\rangle$ ,  $E_i$ , and  $E_f$  are the initial and final states and their energies, respectively,  $\omega$  and D are the photon frequency and dipole operator. For K-edge XANES, the initial state of the photoelectron is 1s, i.e.,  $|i\rangle = |1s\rangle$ , so the dipole-allowed final states have the symmetry of atomic p states (l=1). Also, since the initial state is localized at the absorbing atom, only the final state wave function in the vicinity of the absorber is relevant. It thus turns out that the angular-momentum and site projected partial densities of empty states (PDOSs), with some broadening, resemble the XANES absorption spectra,  $^{15}$  and has been used frequently to compare with experimental data.  $^{16}$  For simplicity, we calculate the density of final states using the ground state electron occupation.

We find that partial densities of states generated from our first principles calculations bear a resemblance to XANES data. For example, our calculated PDOSs projected on the O and Zn atoms [Figs. 1(a) and 1(b), respectively] in bulk ZnO are in good qualitative agreement with the O *K*-edge (Ref. 17) and Zn *K*-edge XANES spectra. In the figures, dominant corresponding features in the XANES spectra and PDOS are paired by thin dashed lines. The fact that the PDOS of both host atoms agrees well with the XANES data gives us strong confidence that this theoretical approach is reliable over a wide range of photon energy. Hencethe local

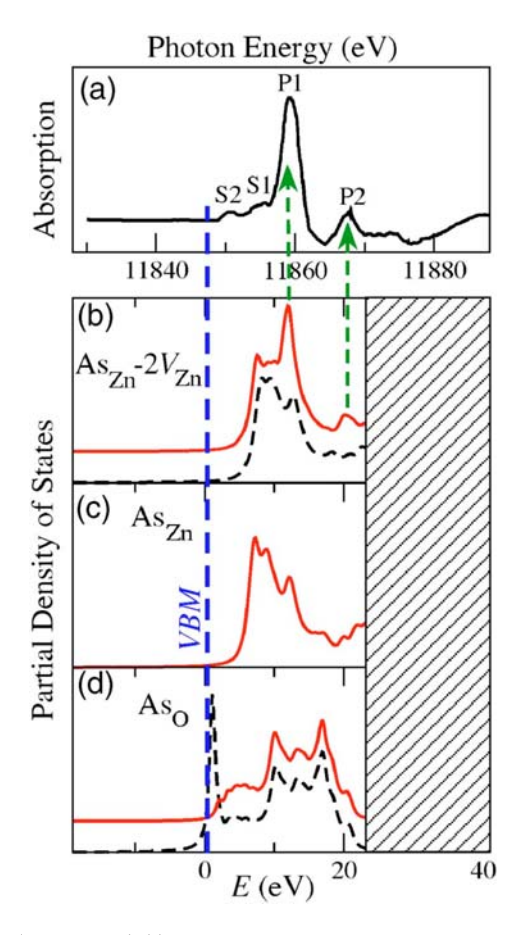


FIG. 2. (Color online) (a) As K-edge XANES spectrum of p-type ZnO:As taken from Ref. 1. [(b)–(d)] Calculated As-site and angular-momentum (l=1) projected PDOSs for  $As_{Zn}$ – $2V_{Zn}$ ,  $As_{Zn}$ , and  $As_{O}$ , respectively. For  $As_{Zn}$ , only PDOS for (3+)-charge state is shown. For  $As_{Zn}$ – $2V_{Zn}$  and  $As_{O}$ , PDOS for both neutral and (1–)-charge states are shown using dashed and solid curves, respectively (when plotted together, solid curves are offset from the dashed curves for clarity). All PDOSs are broadened by a Lorentzian with FWHM=1 eV.

structure of an As defect can be equally well determined by comparing the As PDOS with the As *K*-edge XANES spectra.

Figure 2(a) shows the As K-edge XANES measured from As-doped p-type ZnO by Vaithianathan  $et\ al.^{17}$  In their letter, they interpreted their XANES results in favor of an As substituting an O (As<sub>O</sub>) and concluded that As<sub>O</sub> is the acceptor responsible for the observed p-type conductivity. Here, we will show, based on first principles calculations, that the XANES result in Ref. 17 is actually far more consistent with As<sub>Zn</sub>-2 $V_{Zn}$  complex and quite clearly inconsistent with As<sub>O</sub>.

We have previously calculated As defects in ZnO (Ref. 9) using first principles methods based on a supercell approach (with cell size up to 96 atoms). Here, to compare with the As K-edge XANES spectrum, we use converged electron wave functions to calculate, for each defect configuration, the site and angular-momentum projected PDOS for the As atom (with a radius=1.4 Å and an angular momentum l=1). Sufficient unoccupied states (approximately 400 bands) are included in the calculations to generate the PDOS to  $\sim$ 25 eV above the valence band maximum (VBM).

PDOS are paired by thin dashed lines. The fact that the PDOS of both host atoms agrees well with the XANES data gives us strong confidence that this theoretical approach is reliable over a wide range of photon energy. Hence, the local Downloaded 05 Dec 2006 to 128.111.119.100. Redistribution subject to AIP license or copyright, see http://apl.aip.org/apl/copyright.jsp

p-type conditions (i.e., when the Fermi energy is located near the VBM), the only relevant charge state for As<sub>Zn</sub> (which is a donor) is 3+ whereas the relevant charge states for  $As_{Zn}-2V_{Zn}$  and  $As_{O}$  are neutral and (1-)-charge states. The PDOS for As<sub>O</sub> in both charge states are almost identical except that a prominent sharp peak at 1 eV above VBM in the PDOS for the neutral charge state is absent in the (1 – )-charge state. This peak is a deep localized As<sub>O</sub> acceptor level which becomes occupied in the (1-)-charge state. The PDOSs for  $As_{Zn}-2V_{Zn}$  in neutral and (1-)-charge states are, however, notably different. The PDOS for neutral  $As_{Zn}-2V_{Zn}$  [dashed curve in Fig. 2(b)] is nearly identical to that for  $\mathrm{As}_{\mathrm{Zn}}^{3+}$  [Fig. 2(c)] but clearly differs from that for  $(\mathrm{As}_{\mathrm{Zn}}-2V_{\mathrm{Zn}})^{1-}$ . The ratio between the concentration of  $As_{Zn}-2V_{Zn}$  (or  $As_O$ ) defects in (1-)-charge states (active acceptors) to the concentration of the same defects in neutral charge states (inactive acceptors) depends on the ionization energy and the Fermi energy of the sample. Since the samples of this type are highly compensated and generally show only weak p characteristics, it is likely that majority of the  $As_{Zn}-2V_{Zn}$  are in the (1-)-charge state, i.e., either compensated by donors or being active. On the other hand, if As<sub>O</sub> is formed (calculations show that As<sub>O</sub> is energetically unfavorable), they will be mainly in the neutral charge state in p-type ZnO because calculations show that As<sub>O</sub> is a very deep acceptor.9

We see from Fig. 2 that the PDOS of  $As_{Zn}-2V_{Zn}$  in the (1-)-charge state is far more consistent with the measured XANES than that of As<sub>O</sub>. Indeed, whereas there appears to be little correspondence between features of the As<sub>O</sub> PDOS and the XANES data, the  $As_{Zn}-2V_{Zn}$  PDOS correctly accounts for several qualitative features in the measured spectrum. First, the main XANES peak (P1) at 11 859 eV is approximately 11 eV above the onset of absorption. The corresponding peak of  $As_{Zn}-2V_{Zn}$  is about 12 eV above the VBM. Second, P1 is followed by a sharp drop, and then a slow increase to a much smaller second peak (P2) at around 11 868 eV, with  $E(P2)-E(P1)\approx 9$  eV. An identical feature is observed in the PDOS of  $As_{Zn}-2V_{Zn}$  with a peak separation ≈8 eV. Third, there is a shoulder peak (S1) at about 3 eV below P1, which is also consistent with the shoulder in the PDOS of  $As_{Zn}-2V_{Zn}$ . The origin of the S1 can be traced back to isolated  $As_{Zn}$ , as Fig. 2(c) shows the main feature in the PDOS of As<sub>Zn</sub> is in this energy range. The dominant PDOS peak for neutral charge As<sub>O</sub> is only 1 eV above the VBM (and is thus inside the ZnO band gap), with other peaks being relatively insignificant. In Fig. 2(a) a small shoulder (S2) at 2 eV above the onset of absorption has been observed, which has no correspondence in the  $As_{Zn}-2V_{Zn}$ PDOS. This S2 feature could originate from As<sub>O</sub> and thus give evidence that some Aso defects are present in the sample. However, the small height of S2 relative to the other features in the data would suggest that the concentration of  $As_O$  is much less than that of  $As_{Zn}-2V_{Zn}$ . To summarize, in contradiction to the assignment in Ref. 17, first principles results support the assignment of the measured XANES spectrum to the  $As_{Zn}-2V_{Zn}$  complex.

Note that Vaithianathan *et al.*<sup>17</sup> interpreted their results in favor of As<sub>O</sub> based on an argument about the As oxidation states without any rigorous theory. While XANES peak po-

sitions may occasionally be used to probe the oxidation state of an atom in an organic matrix, such a practice is unlikely to work for crystalline ZnO. In an organic matrix, hybridization between atomic orbitals results in discrete molecular orbitals, so to a large extent each atom maintains its characteristic ionization signature in the XANES spectra. The situation in crystalline materials is, however, qualitatively different since the electronic states must be described in terms of a band structure of itinerating electrons. In such a picture, the valence 4p states of a substituting As strongly intermix with the host states and hence lose their original ionization signature. The only exception may be when the final states are deep inside the band gap, e.g., in the case of  $As_O$ , but the maximum energy separation between the peaks cannot exceed the band gap of 3.4 eV for ZnO.

Based on first principles methods, XANES spectra for As at different sites in ZnO have been simulated. This sheds new light on the interpretation of previous XANES experiments on As-doped p-type ZnO by Vaithianathan  $et\ al.^{17}$  Our results show that the measured XANES is not consistent with As substituting O as previously assigned. Instead, it is far more consistent with the complex acceptor involving As substituting Zn, i.e.,  $As_{Zn}-2V_{Zn}$ .

This work was supported by the Thailand Research Fund, Contract No. BRG4880015. One of the authors (S.B.Z.) is supported by the U.S. DOE/BES and EERE under Grant No. DE-AC36-99G010337. Stimulating discussions with S. Rujirawat and P. Songsiriritthigul are acknowledged.

<sup>&</sup>lt;sup>1</sup>D. C. Look, Mater. Sci. Eng., B **80**, 383 (2001).

<sup>&</sup>lt;sup>2</sup>C. Jagadish and S. J. Pearton, *Zinc Oxide Bulk, Thin Films and Nanostructures* (Elsevier, Oxford, 2006).

<sup>&</sup>lt;sup>3</sup>D. C. Look, D. C. Reynolds, C. W. Litton, R. L. Jones, D. B. Eason, and G. Cantwell, Appl. Phys. Lett. **81**, 1830 (2002).

<sup>&</sup>lt;sup>4</sup>K. Kim, H. Kim, D. Hwang, J. Lim, and S. Park, Appl. Phys. Lett. **83**, 63 (2003).

Guodol.
 Morhain, M. Teisseire, S. Vézian, F. Vigué, F. Raymond, P. Lorenzini,
 J. Guion, G. Neu, and J.-P. Faurie, Phys. Status Solidi B 229, 881 (2002).

R. Ryu, T. S. Lee, and H. W. White, Appl. Phys. Lett. 83, 87 (2003).
 Aoki, Y. Shimizu, A. Miyake, A. Nakamura, Y. Nakanishi, and Y. Hatanaka, Phys. Status Solidi B 229, 911 (2002).

K. H. Park, S. B. Zhang, and S.-H. Wei, Phys. Rev. B 66, 073202 (2002).
 Limpijumnong, S. B. Zhang, S.-H. Wei, and C. H. Park, Phys. Rev. Lett. 92, 155504 (2004).

<sup>&</sup>lt;sup>10</sup>W.-J. Lee, J. Kang, and K. J. Chang, Phys. Rev. B **73**, 024117 (2006); Physica B **376–377**, 699 (2006).

<sup>&</sup>lt;sup>11</sup>U. Wahl, E. Rita, J. G. Correia, A. C. Marques, E. Alves, and J. C. Soares, Phys. Rev. Lett. **95**, 215503 (2005).

<sup>&</sup>lt;sup>12</sup>F. X. Xiu, Z. Yang, L. J. Mandalapu, D. T. Zhao, and J. L. Liu, Appl. Phys. Lett. **87**, 252102 (2005).

<sup>&</sup>lt;sup>13</sup>G. Braunstein, A. Muraviev, H. Saxena, N. Dhere, V. Richter, and R. Kalish, Appl. Phys. Lett. 87, 192103 (2005).

<sup>&</sup>lt;sup>14</sup>D. C. Koningsberger and R. Prins, X-ray Absorption: Principles, Applications, Techniques of EXAFS, SEXAFS and XANES (Wiley, New York, 1988).

<sup>&</sup>lt;sup>15</sup>P. Ravindran, A. Kjekshus, H. Fjellvåg, A. Delin, and O. Eriksson, Phys. Rev. B 65, 064445 (2002).

<sup>&</sup>lt;sup>16</sup>T. Mizoguchi, I. Tanaka, S. Yoshioka, M. Kunisu, T. Yamamoto, and W. Y. Ching, Phys. Rev. B 70, 045103 (2004).

<sup>&</sup>lt;sup>17</sup>V. Vaithianathan, B.-T. Lee, C.-H. Chang, K. Asokan, and S. S. Kim, Appl. Phys. Lett. **88**, 112103 (2006).

<sup>&</sup>lt;sup>18</sup>S. Larcheri, C. Armellini, F. Rocca, A. Kuzmin, R. Kalendarev, G. Dalba, R. Graziola, J. Purans, D. Pailharey, and F. Jandard, Superlattices Microstruct. 39, 267 (2006).

# Carbon-nitrogen molecules in GaAs and GaP

Sukit Limpijumnong, <sup>1,2</sup> Pakpoom Reunchan, <sup>1,2</sup> Anderson Janotti, <sup>1</sup> and Chris G. Van de Walle <sup>1</sup> Materials Department, University of California, Santa Barbara, California 93106, USA <sup>2</sup> School of Physics, Suranaree University of Technology and National Synchrotron Research Center, Nakhon Ratchasima 30000, Thailand (Received 6 February 2008; published 21 May 2008)

A carbon-nitrogen molecule in GaAs and GaP is investigated by using first-principles density functional pseudopotential calculations. The formation energy calculations show that the molecule favors substituting for an anion site (As or P) over being an interstitial under all equilibrium growth conditions. Under *p*-type conditions, the molecule exhibits the characteristic triple bonding and acts as a donor. When the Fermi level is higher (*n* type), the molecule acts as an acceptor by accepting electrons into its antibonding states and exhibits double or single bonding. The bond length and vibrational frequencies for each configuration are calculated and compared to those in recent experiments. Trends in the changes in bond length and vibrational frequencies with respect to the number of electrons in the antibonding states are discussed.

DOI: 10.1103/PhysRevB.77.195209 PACS number(s): 61.72.-y, 71.55.Eq

#### I. INTRODUCTION

Small amounts of nitrogen can strongly affect the electronic properties, such as the band gap and electron effective mass, of GaP and GaAs. This opens up an opportunity to continuously modify the band gap (as well as other properties) of these III-V semiconductors for advanced electronic and optoelectronic devices. This prospect has stimulated substantial research on dilute GaAsN and GaPN alloys both experimentally<sup>1-7</sup> and theoretically.<sup>8-14</sup> It is therefore very important that defects and impurities in these alloys are studied in detail. Carbon is a common impurity in various growth techniques 15,16 and sometimes, it is intentionally used as a p-type dopant; 17-20 complex formations between C and N could therefore be an important issue. Recently, Ulrici and Clerjaud<sup>21</sup> observed a sharp local vibration mode at 2087 cm<sup>-1</sup> (at T=7 K) in GaP and a similar mode in GaAs. They identified it as a CN complex with a triple bond (between C and N) aligned along the [100] direction.

An experimental work<sup>21</sup> rigorously identified the chemical composition and the dipole direction of the complex; however, the actual location of the CN molecule in the lattice is still unclear. Both CN substituting on anion sites (CN<sub>As</sub> in GaAs or CN<sub>P</sub> in GaP) and interstitial CN (CN<sub>i</sub>) are potentially consistent with experiment and were proposed as possible models in Ref. 21. In other semiconductor compounds (such as ZnO, GaN, and ZnSe), small diatomic molecules such as N<sub>2</sub>, O<sub>2</sub>, or CN have been studied both by first-principles calculations and by different experiments and found to prefer substitution on an anion site. <sup>15,22–25</sup> However, the energy difference between the substitutional and interstitial sites varies from material to material; explicit calculations are therefore required to determine which site is more favorable for a given material.

In this paper, we use first-principles calculations to calculate the formation energies of  $CN_{As(or\ P)}$  and  $CN_i$ . We find that, similar to other semiconductor compounds that have been studied before, CN energetically prefers substituting on anion sites of GaAs and GaP over interstitial sites in all thermal equilibrium growth conditions. We also calculate the vibrational frequency of the complex and find reasonable

agreement with the measured value. The CN molecule behaves very similarly in GaAs and GaP, and therefore, we will focus our discussion on CN in GaAs. Numerical results will be reported for both GaAs and GaP.

#### II. COMPUTATIONAL METHOD

Our calculations are performed by using density functional theory with the local density approximation (LDA). We use ultrasoft pseudopotentials, as implemented in the VASP code. The Ga 3d electrons are treated as valence electrons. The cutoff energy for the plane-wave basis set is 262 eV. We use a supercell with 64 atoms for the defect studies, and a  $2 \times 2 \times 2$  shifted Monkhorst–Pack special k-point grid ( $\Gamma$  point not included) is employed for the Brillouin zone integration. The calculated GaAs lattice constant (5.60 Å, which is within 1% of the experimental value) is used. The electronic deep levels introduced by CN are examined by taking averages over the special k points. All the atoms are relaxed by minimization of the Hellmann–Feynman forces until all the forces are less than 0.05 eV/Å.

The formation energies of  $CN_i$  and  $CN_{As}$  are defined, following Refs. 22 and 29, as

$$E_f(CN_i^q) = E_{tot}(CN_i^q) - E_{tot}(bulk) - \mu_C - \mu_N + qE_F,$$

$$E_f(CN_{As}^q) = E_{tot}(CN_{As}^q) - E_{tot}(bulk) - \mu_C - \mu_N + \mu_{As} + qE_F,$$
(1)

where  $E_{\text{tot}}(D^q)$  is the total energy of the supercell with defect D in charge state q.  $E_{\text{tot}}(\text{bulk})$  is the total energy of the supercell without a defect.  $\mu_{\text{C}}$ ,  $\mu_{\text{N}}$ , and  $\mu_{\text{As}}$  are the chemical potentials of a C atom, an N atom, and an As atom, respectively. For convenience,  $\mu_{\text{C}}$  and  $\mu_{\text{As}}$  are referenced to the energy of a C atom in diamond and an As atom in solid As, respectively.  $\mu_{\text{N}}$  is referenced to the energy of an N atom in a free  $N_2$  molecule. Growth conditions for GaAs are close to equilibrium, requiring that  $\mu_{\text{Ga}} + \mu_{\text{As}} = \mu_{\text{GaAs}} = -0.69$  eV (calculated GaAs heat of formation), where  $\mu_{\text{Ga}}$  is a chemical potential of a Ga atom, which is referenced to the energy of a Ga atom in bulk Ga.  $E_F$  is the electron Fermi level with

respect to the valence-band maximum (VBM).

The local vibrational mode frequencies of the molecules are calculated by using the so-called frozen phonon approach,<sup>30</sup> in which we followed a practical methodology described in Ref. 31. Because C and N atoms have similar masses, we equally displaced C and N to calculate the potential energy of stretching and compressing bonds. The mass of the oscillator is taken as the reduced mass:

$$\mu = \frac{m_{\rm C} m_{\rm N}}{m_{\rm N} + m_{\rm C}},\tag{2}$$

where  $m_{\rm C}$  and  $m_{\rm N}$  are the masses of C and N atoms. We find that the (harmonic) stretching vibrational frequencies of the oscillator agree very well with a full dynamic matrix calculation with the matrix constructed by displacing each and every atom in the supercell one at a time in all three principal axes directions. A test calculation (on CN<sub>As</sub>) shows that the agreement between the full dynamic and reduced-mass results is better than 5 cm<sup>-1</sup>. An important benefit of the reduced-mass calculation (besides a significant reduction in computational effort) is that it allows us to calculate the anharmonic part of the vibration, which we found to be on the order of 20 cm<sup>-1</sup>. The potential energy is evaluated at seven values of displacements, with a maximum amplitude of up to 10% of the C-N equilibrium bond distance. To test the accuracy of the approach, we calculated the stretch frequency of a C-N mode in the HCN molecule and obtained the value of 2057 cm<sup>-1</sup>, which is slightly smaller than the experimental value of 2089 cm<sup>-1</sup>.<sup>32</sup> The calculated equilibrium C-N bond distance is fortuitously equal to the experimental value of 1.156 Å. The small underestimation in vibrational frequency, which is by 32 cm<sup>-1</sup>, is expected to be systematic. Therefore, we have added the value of  $\omega_{ER}$ =32 cm<sup>-1</sup> to all of our calculated frequencies as a systematic correction.

# III. RESULTS AND DISCUSSION

We investigated two forms of CN molecules in GaAs: at the substitutional As site and at the interstitial site. If initially the CN molecule is symmetrically placed at the As site (in the form of a split-interstitial configuration) with its principal axis aligned along the [100] direction, due to the symmetry, the orientation of the molecule will remain unchanged even when relaxation is allowed. The resulting symmetric configuration,  $\text{CN}_{\text{As}}(\text{sym})$ , is shown in Fig. 1(a). However, this orientation is not the lowest energy one for all charge states. Breaking the symmetry causes the molecule (in some charge states) to spontaneously rotate, without any barrier, into an asymmetric configuration [Fig. 1(b),  $\text{CN}_{\text{As}}(\text{asym})$  in the 2+ charge state].

For an interstitial CN, there are two possible sites for the zinc-blende crystal: the tetrahedral interstitial sites surrounded by either Ga  $[T_d(Ga)]$  or As atoms  $[T_d(As)]$ . The calculations show that  $CN_i$  energetically prefers the  $T_d(Ga)$  site over the  $T_d(As)$  site. The  $T_d(Ga)$  site is surrounded by four Ga atoms in a tetrahedral configuration similar to the local structure surrounding a substitutional As lattice site. Again, if the molecule is initially placed in a high-symmetry orientation,  $CN_i(sym)$ , the orientation remains fixed by sym-

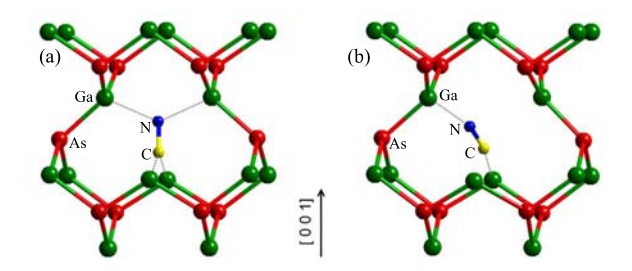


FIG. 1. (Color online) Local atomic geometry of a CN molecule substituting on an As site in GaAs: (a) symmetric configuration,  $\mathrm{CN}_{\mathrm{As}}(\mathrm{sym})$ , and (b) asymmetric configuration,  $\mathrm{CN}_{\mathrm{As}}(\mathrm{asym})$ . Both are shown for the 2+ charge state.

metry, but breaking the symmetry can lead to rotation of the molecule into a lower-energy asymmetric configuration,  $CN_i$  (asym).

### A. Substitutional CN molecules (CN<sub>As</sub>)

The substitutional molecule CN<sub>As</sub> introduces a deep donor level (at approximately 0.25 eV) in the GaAs band gap, as shown in Fig. 2. The charge density (Fig. 3) of these levels resembles the  $pp \pi^*$  molecular orbital of the CN molecule.<sup>22</sup> The molecular orbital theory tells us that the CN molecule has the following molecular orbitals, which are in order of increasing energy:  $ss\sigma$ ,  $ss\sigma^*$ ,  $pp\pi$  (doublet),  $pp\sigma$ ,  $pp\pi^*$ (doublet), and  $pp\sigma^*$ . In the neutral charge state, the CN molecule on an As site has 12 valence electrons: 9 from the CN itself and 3 more contributed from the surrounding Ga atoms. These 12 electrons occupy the CN molecular orbitals up to the lower  $pp\pi^*$  level and leave the higher  $pp\pi^*$  level empty. Because the lower  $pp\pi^*$  level is located deep inside the GaAs band gap, CNAs can donate up to two electrons and become CN<sub>As</sub> when the Fermi level of the system falls below the 0.25 eV donor level. The bonding between the C and N atoms in  $CN_{As}^{2+}$  is a triple bond  $(C \equiv N)$ , with a bond distance of 1.17–1.20 Å (depending on the orientation), which is in good agreement with the known triple-bond length between C and N in HCN of 1.156 Å.33

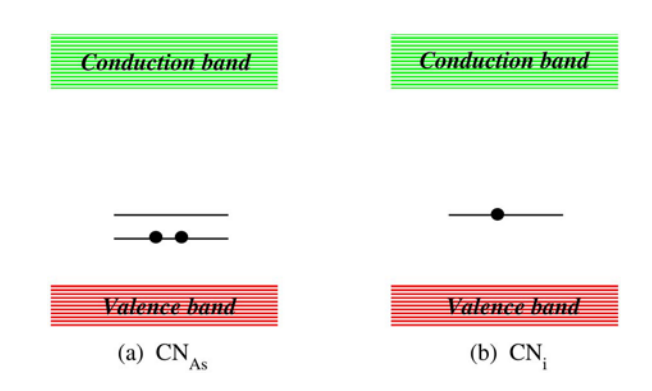


FIG. 2. (Color online) Schematic illustrations of the  $pp\pi^*$  single-particle energy levels of the CN molecule in the GaAs band gap. (a) Substituting on an As site (CN<sub>As</sub>) and (b) CN on an interstitial site (CN<sub>i</sub>). The solid dots show the electron occupation for the neutral charge state.

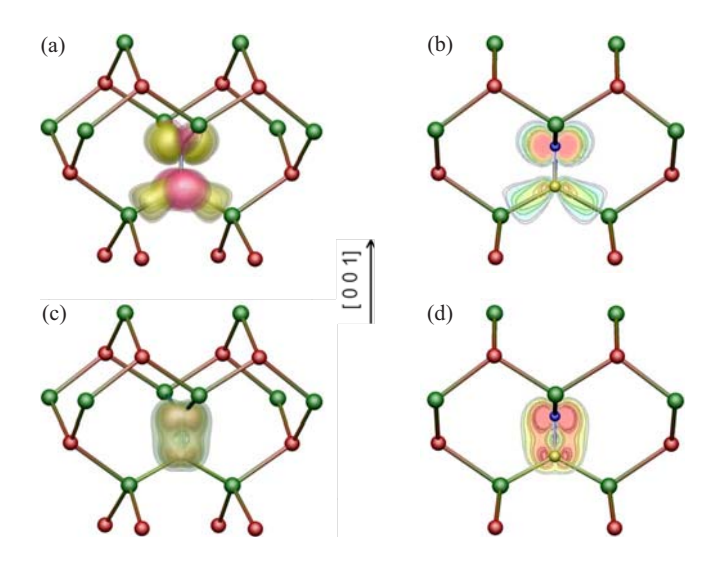


FIG. 3. (Color online) (a) Charge density of the  $pp\pi^*$  states of  $CN_{As}$  that are located in the GaAs band gap. (b) Contour plot of one of the states in (a) in a (001) plane cutting through the CN molecule. (c) Charge density of one of the  $pp\pi$  states of  $CN_{As}$  that resides below the valence-band maximum. (d) The corresponding contour plot of (c).

In the 2+ charge state, the  $pp\pi^*$  level is unoccupied; hence, the  $CN_{As}^{2+}$  has little interaction with the surrounding neighbor. The molecule can therefore rotate quite freely, and it indeed moves away from the symmetric configuration to a new orientation that has a lower energy. Our calculated energy profile for the molecule rotating from the [001] to the (near) [110] direction, which is based on the nudged elastic band (NEB) method,<sup>34</sup> is shown in Fig. 4. We can see that starting from the symmetric [001] orientation, the molecule can rotate without any barrier to a new orientation in which the molecule's principal axis is nearly parallel with the [110] direction, lowering its energy by 0.27 eV in the process. By investigating the charge density (not shown), we found that the asymmetric configuration allows better interactions

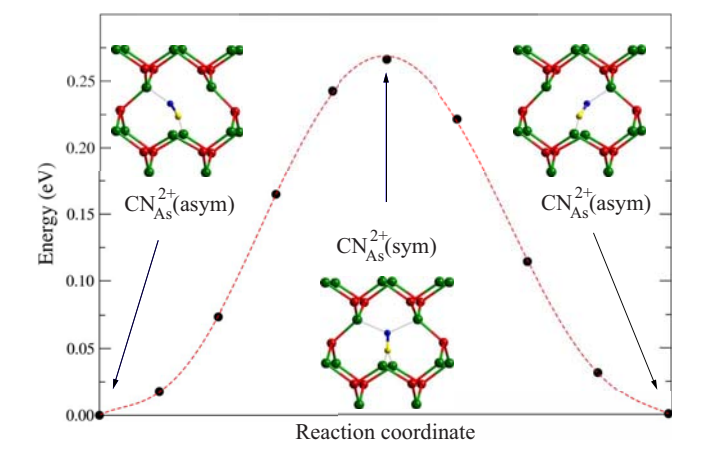


FIG. 4. (Color online) Calculated energy of  $CN_{As}^{2+}$  as the CN molecule rotates from the asymmetric to symmetric and back to an equivalent asymmetric configuration. The symmetric configuration is the saddle point along this path.

TABLE I. Calculated bond lengths  $d_{\text{C-N}}$ , stretching frequencies  $\omega$ , and formation energies  $E_f$  (for the Fermi level at the VBM) of CN molecules in GaAs in the symmetric (asymmetric in parentheses) configurations. For each charge state, the lower-energy configuration is shown in boldface.

Charge state	4		$E_f$ (eV)					
(q)	$d_{ ext{C-N}} \ ( ext{Å})$	$\omega$ (cm <sup>-1</sup> )	Ga rich	As rich				
CN on the As site (CN <sub>As</sub> )								
2+	1.20	1779	2.42	3.11				
	<b>(1.17)</b>	(2052)	<b>(2.15)</b>	<b>(2.84)</b>				
1+	1.25	1481	2.42	3.11				
	(1.22)	(1734)	(2.46)	(3.15)				
0	1.30	1328	2.58	3.27				
	(1.25)	(1345)	(3.08)	(3.77)				
1-	1.35	1173	3.13	3.82				
	(1.31)	(1182)	(3.34)	(4.03)				
2-	1.38	1095	4.03	4.72				
	<b>(1.40)</b>	<b>(1097)</b>	(3.82)	<b>(4.51)</b>				
CN on the interstitial site $(CN_i)$								
1+	1.20	1897	4.41	4.41				
	<b>(1.19)</b>	<b>(1934)</b>	(3.85)	<b>(3.85)</b>				
0	(1.25)	(1519)	(4.37)	(4.37)				

between the bonding pp states of CN and two of the surrounding Ga atoms, resulting in a lower formation energy.

Starting from  $CN_{As}^{2+}$ , when the Fermi level is raised, the defect levels characteristic of  $pp\pi^*$  molecular orbitals become occupied with electrons, and the charge state of  $CN_{As}$  increases from 2+ to 1+, 0, 1–, and 2–. Because these defect states correspond to antibonding orbitals of the free molecule, occupying them leads to an increase in the CN bond length (of approximately 0.05 Å per electron added), as shown in Table I. In addition, the charge density plots [Fig. 3(a) and 3(b)] reveal that the  $pp\pi^*$  states hybridize with the dangling-bond states of the surrounding Ga atoms in the directions in which the density lobes are pointing. For instance, the lower two lobes in Fig. 3(b) clearly show the bond formation between the C atom and two Ga atoms, whereas the upper two lobes still maintain the molecular  $pp\pi^*$  features. Because of the possibility of bond formation with the neighboring Ga atoms,  $CN_{As}^{1+}$ ,  $CN_{As}^{0}$ , and  $CN_{As}^{1-}$  all favor the symmetric configuration. The state of  $CN_{As}^{2-}$ , on the other hand, favors an asymmetric configuration with the neighboring of the possibility of the symmetric configuration.

 $\text{CN}_{\text{As}}^{2-}$ , on the other hand, favors an asymmetric configuration (with a different orientation from that of  $\text{CN}_{\text{As}}^{2+}$ ). Because the  $pp\pi^*$  states are fully occupied, the molecule tries to optimize the Coulombic interaction between these  $pp\pi^*$  states and its four Ga neighbors. Since the charge distribution for the CN molecule is not symmetric (the N atom is more electronegative than the C atom), the asymmetric configuration allows the N side of the molecule to bind with three Ga atoms instead of two, making the configuration more stable.

The formation energies of  $CN_{As}$  are shown in Table I (Table II for CN in GaP) and plots as a function of Fermi level are shown in Fig. 5 for two growth conditions: Ga rich ( $\mu_{Ga}$ =0) and As rich ( $\mu_{As}$ =0). As can be seen from Eq. (1),

TABLE II. Calculated bond lengths  $d_{\text{C-N}}$ , stretching frequencies  $\omega$ , and formation energies  $E_f$  (for the Fermi level at the VBM) of CN molecules in GaP in the symmetric (asymmetric in parentheses) configurations. For each charge state, the lower-energy configuration is shown in boldface.

Charge state	d	ω	$E_f$ (eV)					
(q)	$d_{ ext{C-N}} \ ( ext{Å})$	$(cm^{-1})$	Ga rich	P rich				
CN on the $P$ site $(CN_P)$								
2+	1.20	1734	2.25	3.13				
	<b>(1.18)</b>	(2028)	<b>(2.12)</b>	(3.00)				
1+	1.25	1517	2.40	3.28				
0	1.31	1352	2.75	3.63				
1-	1.36	1197	3.58	4.46				
	(1.33)	(1283)	(3.74)	(4.62)				
2-	1.39	1113	4.77	5.65				
	<b>(1.41)</b>	<b>(1105)</b>	<b>(4.50)</b>	<b>(5.38)</b>				
CN on the interstitial site $(CN_i)$								
1+	1.21	1875	4.43	4.43				
	<b>(1.19)</b>	<b>(1933)</b>	(3.96)	(3.96)				
0	(1.26)	(1511)	(4.82)	(4.82)				

the slope of the plot indicates the charge state of the CN molecule. In our plots, only the lowest energy charge state (at a given Fermi energy) is shown. For example,  $CN_{As}(asym)$  is stable in the 2+ charge state when the  $E_F$  of the system is located between 0.0 and 0.25 eV; therefore, the line has a slope of 2. For 0.25 eV  $< E_F <$  0.70 eV, the symmetric configuration becomes more stable and the neutral and 1- (for a narrow range near  $E_F$ =0.70 eV) charge states are the lowest in energy. At higher  $E_F$ , the asymmetric configuration with the 2- charge state, i.e.,  $CN_{As}^{2-}(asym)$ , becomes the most stable.<sup>36</sup> Therefore, the stable configurations in order of increasing  $E_F$  are as follows:  $CN_{As}^{2+}(asym)$ ,  $CN_{As}^{0}(sym)$ ,  $CN_{As}^{1-}(sym)$ , and  $CN_{As}^{2-}(asym)$ .  $CN_{As}^{1+}$  is never stable. Because CN is substituting on the As site to form CN<sub>As</sub>, its formation energy is lower in the Ga-rich condition than that in the As-rich condition. The plots also show that the formation energy of CNAs is always lower than that of CN; for both the Ga- and As-rich conditions throughout the entire Fermi-energy range, with an energy difference of at least 1 eV. This implies that CNAs is far easier to form than  $CN_i$ .

The trends in bonding discussed above are reflected in our calculated values of vibrational frequencies, which show that the frequency is highest for  $CN_{As}^{2+}$  (2052 cm<sup>-1</sup> for an asymmetric configuration and 1779 cm<sup>-1</sup> for a hypothetical sym-

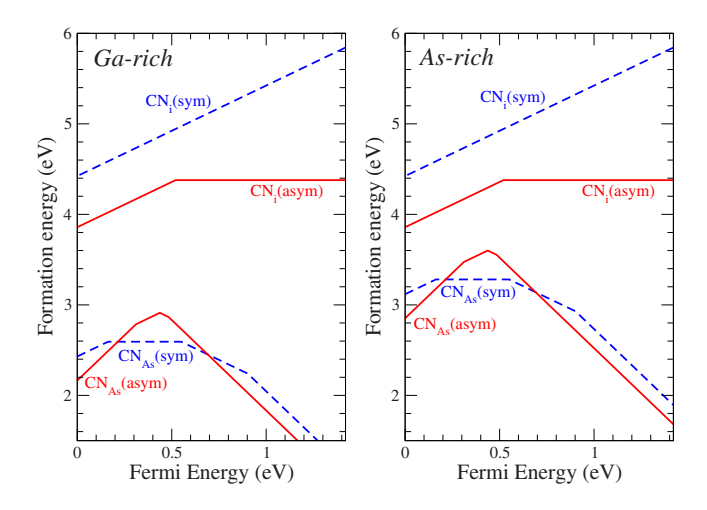


FIG. 5. (Color online) Formation energies of CN molecules in GaAs as a function of the Fermi energy. The solid lines and dashed lines represent the asymmetric and symmetric configurations, respectively.

metric configuration). This is because in the 2+ charge state, the bonding states of the molecule are all occupied and the antibonding states  $(pp\pi^*)$  are all empty. As electrons are added into the antibonding states of  $\text{CN}_{\text{As}}$ , the C-N bond is weakened and the frequency is reduced to 1481, 1328, 1173, and 1097 cm<sup>-1</sup> for  $\text{CN}_{\text{As}}^{1+}$ ,  $\text{CN}_{\text{As}}^{0}$ ,  $\text{CN}_{\text{As}}^{1-}$ , and  $\text{CN}_{\text{As}}^{2-}$ , respectively.

### B. Interstitial CN molecules (CN<sub>i</sub>)

The CN molecule has a total of nine electrons filling its molecular orbitals in the following order:  $ss\sigma$ ,  $ss\sigma^*$ ,  $pp\pi$ (doublet), and with the last electron occupying  $pp\sigma$ . This leaves the  $pp\sigma$  bonding state half-occupied and able to accept one more electron. Due to the strong bonding nature in the CN molecule, this  $pp\sigma$  state has a low energy. When the molecule is placed in GaAs, the  $pp\sigma$  state lies below the VBM and always becomes fully occupied. At the same time, the insertion of CN at an interstitial site also creates strain in nearby Ga-As bonds, leading to Ga-As bond extension (or breaking). The broken Ga-As bonds are shown in dotted lines in Fig. 6. CN<sub>i</sub> is stable in two charge states: 1+ and neutral. We initially used symmetric configurations in our calculations [Fig. 6(a)], but this configuration can spontaneously relax into asymmetric configurations with lower energies [Fig. 6(b) and 6(c)] if symmetry breaking is allowed. The energy change as the CN<sub>i</sub> rotates from the symmetric configuration into the asymmetric one (for 1+ charge state) calculated by using the NEB method is shown in Fig. 7. Figure 7 shows that the asymmetric configuration is favored

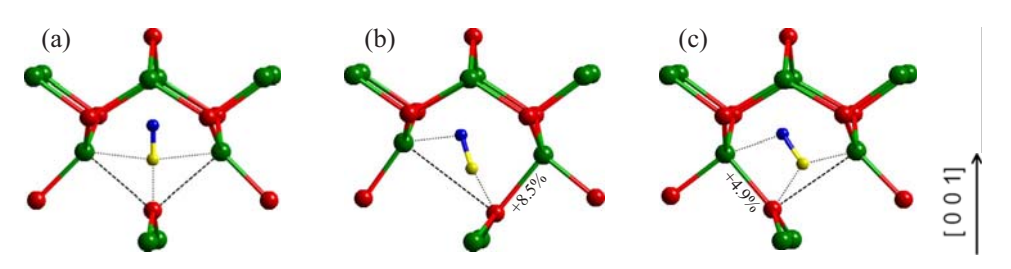


FIG. 6. (Color online) Local atomic geometry of interstitial CN molecules in GaAs: (a)  $CN_i^+(sym)$ , (b)  $CN_i^+(asym)$ , and (c)  $CN_i^0(asym)$ .

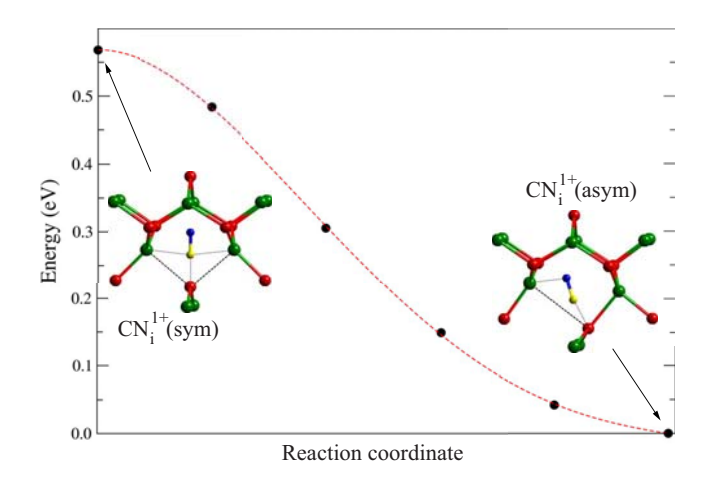


FIG. 7. (Color online) Calculated energy of  $CN_i^{1+}$  as the CN molecule rotates from a symmetric to an asymmetric configuration. The rotation occurs without any barrier and lowers the energy by almost 0.6 eV.

over the symmetric one by  $\sim 0.6$  eV. We can clearly see in the asymmetric configuration [Fig. 6(c)] that only one of the Ga-As bonds is now broken (another bond is extended from a typical Ga-As bond). One of the two electrons released from the broken bond goes to the  $pp\sigma$  state of the CN molecule, whereas another one is removed, resulting in the 1+ charge state. As an additional electron is added (increasing the charge state of the defect from 1+ to neutral), the additional electron goes to the  $pp\pi^*$  level, which is located at approximately 0.5 eV above the VBM (see Fig. 2). This leads to the  $\pm 1/0$  transition level of CN<sub>i</sub> at 0.5 eV above the VBM. The occupation of the  $pp\pi^*$  level leads to the increase in the CN bond to 1.25 Å and is reflected in an enhanced binding between the molecule and its neighbors [Fig. 6(c)] compared to the 1+ charge state [Fig. 6(b)]. Because the electron density of the  $pp\pi^*$  state has four lobes pointing outward, which is similar to Fig. 3(b), when this state is occupied, the molecule can gain energy by turning the lobes to form bonds with the neighboring atoms.

Vibrational frequencies for the stretching modes of  $CN_i$  in GaAs and GaP are shown in Tables I and II. The frequency is higher for the  $CN_i$  in the 1+ charge state, which has all the bonding states occupied and the antibonding states empty. The frequency of 1934 cm<sup>-1</sup> (1897 cm<sup>-1</sup> for a hypothetical symmetric configuration) is comparable to that of  $CN_{As}^{2+}(asym)$ , which has a similar electron occupation on the molecule. For the neutral charge state  $CN_i$ , with an electron occupying the  $pp\pi^*$  state, the C-N bond length increases to 1.25 Å and the vibrational frequency decreases to 1519 cm<sup>-1</sup>.

# C. General trends of the bond length and the vibrational frequency

Our results show that the C-N bond distance becomes larger (and the vibrational frequency becomes lower) as more electrons are added into the  $pp\pi^*$  states. Our investigations of the various configurations of CN molecules in GaAs and GaP allow us to quantitatively study the relation-

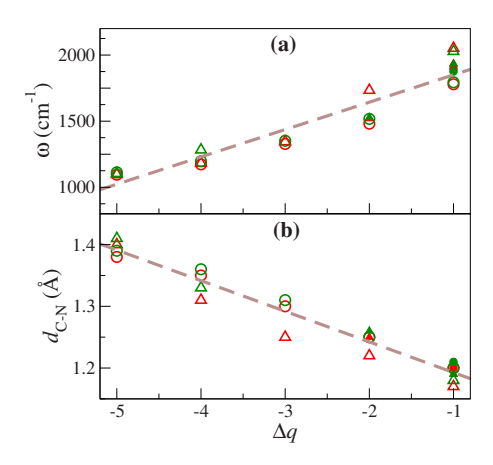


FIG. 8. (Color online) (a) Calculated vibrational frequencies and (b) C-N bond distances for various configurations of a CN molecule in GaAs and GaP as a function of charge  $\Delta q$  inserted into the molecule, which are measured relative to a neutral free CN molecule with nine electrons. The solid symbols are for interstitial CN and the open symbols are for substitutional CN. The colors code the host material (red for GaAs and green for GaP), whereas the symbols are used to distinguish the symmetric (circle) from the asymmetric (triangle) configurations. The CN molecule is characterized as triply, doubly, or singly bonded for  $\Delta q$ =-1, -3, and -5, respectively. The dashed lines are linear fits to all of the data points.

ship between the electron occupation (of the CN molecule) and the bond length as well as the vibrational frequency. To do this, we define  $\Delta q$  as the additional charge being added to the CN molecule relative to the neutral free CN molecule. A free CN molecule has nine electrons, which occupy the molecular states up to half of the  $pp\sigma$  state. Since this state is located below the VBM of GaAs, it is always fully occupied. This means that at least one electron from the host has to be added to the molecule  $(\Delta q = -1)$  and the electron occupation of the molecule becomes the same as that of a free (triplebonded) CN<sup>-</sup> ion. For the CN molecule in GaAs, this occupation corresponds to the lowest charge state, i.e.,  $CN_{As}^{2+}$  and  $CN_i^{1+}$ . As the Fermi energy is raised, electrons are inserted into the antibonding states ( $pp\pi^*$  states) of the CN molecule, thus weakening the C-N bond. When two electrons are inserted into the antibonding state (i.e., CN<sub>As</sub>), making  $\Delta q = -3$ , the C-N bond is reduced to a double bond instead of a triple bond. When four electrons are inserted into the antibonding states (i.e.,  $CN_{As}^{2-}$ ), making  $\Delta q = -5$ , the C-N bond is reduced to a single bond. Our calculations thus show that CNAs can have its bond strength varied from a triple bond down to a single bond depending on the electron occupation. CN<sub>i</sub>, on the other hand, can only exhibit the bond strength of a triple bond (CN<sub>i</sub><sup>1+</sup>) or a triple bond with one electron in the antibonding state  $(CN_i^0)$  (which can be considered as halfway between a double bond and a triple bond).

A plot of the C-N bond distance as a function of  $\Delta q$  is shown in Fig. 8(b). The bond distance, especially of the symmetric configurations, clearly show a linear trend with  $\Delta q$ . The deviations from the linear trend in the case of some of the asymmetric configurations can be attributed to the interaction with neighboring host atoms. A linear fit between the bond distance and  $\Delta q$  for all data points yields

$$d_{\text{C-N}} = -0.0496\Delta q + 1.143,\tag{3}$$

where  $d_{\text{C-N}}$  is the bond distance between C and N in Å. The bond length increases by approximately 0.05 Å for every electron inserted.

The vibrational frequency decreases as the bond is extended. The relationship between the frequency and  $\Delta q$  is shown in Fig. 8(a). Again, a linear trend is seen. A linear fit yields

$$\omega = 207\Delta q + 2057,\tag{4}$$

where  $\omega$  is the vibration frequency in cm<sup>-1</sup>, i.e., the frequency is redshifted by approximately 200 cm<sup>-1</sup> for every electron that is inserted. Deviations from the fit (on the order of 100 cm<sup>-1</sup>) occur because the actual frequency also depends on other factors such as the detailed local geometry. Still, the linear fit in Eq. (4) nicely highlights the general trend, even if it does not provide a completely accurate prediction of the frequency.

# D. Discussion and comparison with experiment

Ulrici and Clerjaud<sup>21</sup> performed a polarized infrared absorption spectroscopy on C-doped dilute-nitride GaAs and GaP. They observed a sharp local vibrational mode at 2087.1 cm<sup>-1</sup> (at T=7 K) in GaP and a similar mode (2088.5 cm<sup>-1</sup>) in GaAs. They identified it as a CN complex with a triple bond (between C and N) aligned along three equivalent  $\langle 100 \rangle$  directions. Their C and N assignments were based on their observation of additional weak peaks at 2031 and 2048 cm<sup>-1</sup>, which exhibit an intensity ratio and frequency shift that match the natural abundance and predicted frequency shift for C<sup>13</sup> and N<sup>15</sup> isotopes. The orientation of the molecule was confirmed by polarized IR absorption under different types of uniaxial stress.

An inspection of Tables I and II shows that the measured frequency of 2087 cm<sup>-1</sup> is most consistent with our calculated frequencies for triply bonded CN molecules with  $\Delta q$ =-1. A more detailed identification runs into some complications, however. There are four configurations with triple bonds covered in our study:  $CN_{As}^{2+}(asym)$ ,  $CN_{As}^{2+}(sym)$ ,  $CN_i^{1+}(asym)$ , and  $CN_i^{1+}(sym)$ . (1)  $CN_{As}^{2+}(asym)$  provides the best matching frequency to the experiment (lower by 36 cm<sup>-1</sup>, which is well within the computational error bar). However, the molecule does not align along (100) but, instead, prefers to align in a direction close to  $\langle 110 \rangle$ . (2) CN<sub>As</sub><sup>2+</sup>(sym) has the correct orientation; however, its frequency is too low (by 309 cm<sup>-1</sup>), and, even more importantly, it is not energetically stable and spontaneously rotates to  $CN_{As}^{2+}(asym)$ , lowering the energy by 0.27 eV. Therefore, we can rule out  $CN_{As}^{2+}(sym)$ . (3)  $\underline{CN_i^{1+}(asym)}$  is a possible candidate. Its calculated vibrational frequency is not too far from the observed value (lower by 154 cm<sup>-1</sup>). However, its orientation also deviated from (100) by 16°. In addition, the interstitial configurations are energetically unfavorable compared to those of  $CN_{As}^{2+}(asym)$ . (4)  $CN_i^{1+}(sym)$  is an unlikely candidate because it is not energetically stable. It can spontaneously rotate to the asymmetric configuration and gain 0.6 eV. In addition, its vibrational frequency is even lower than

that of the asymmetric configuration, widening the disagreement with experiment to 191 cm<sup>-1</sup>.

Our first-principles calculations of vibrational frequencies for CN molecules in various configurations in GaAs and GaP therefore generally support Ulrici and Clerjaud's<sup>21</sup> assignment of the 2087 cm<sup>-1</sup> mode to a triply bonded CN molecule. However, our calculations also show that the triply bonded CN molecule (in either the substitutional or interstitial configurations) does *not* symmetrically align in a tetrahedral site surrounded by four Ga atoms. As a result, neither  $\text{CN}_{\text{As}}$  nor  $\text{CN}_i$  have the C-N axis aligned in the  $\langle 100 \rangle$  direction, as proposed by Ulrici and Clerjaud.<sup>21</sup> However, given a rather low rotation barrier of only 0.27 eV (Fig. 4), it is possible that  $\text{CN}_{\text{As}}^{2+}(\text{asym})$  is constantly rotating, resulting in an average orientation in the  $\langle 100 \rangle$  direction observed in the experiment.

#### IV. CONCLUSIONS

We have presented first-principles results for CN molecules in GaAs and GaP. The study covered two possible lattice locations: (1) CN molecules substituting for anions  $(CN_{As(or\ P)})$  and (2) interstitial CN molecules at the  $T_d$  site surrounded by four Ga atoms (CN<sub>i</sub>). All possible charge states and various orientations were considered. The calculated formation energies show that the molecule favors substituting for the anion site over the interstitial configuration for all equilibrium growth conditions with a margin of at least 1 eV. The calculations predict the CN molecule to produce a level with a strong  $pp\pi^*$  molecular orbital characteristic at approximately 0.5–0.8 eV above the VBM. In p-type conditions, where the Fermi level is located below this  $pp\pi^*$ level, the molecules are triply bonded and form donor defect centers (double donor  $\mathrm{CN}_{\mathrm{As}}^{2+}$  and single donor  $\mathrm{CN}_{i}^{1+}$ ). The calculations with full relaxation show that triply bonded  $CN_{As}^{2+}$  and  $CN_{i}^{1+}$  do not symmetrically orient in the Ga tetrahedron but, instead, are tilted in order to gain better interactions with neighboring Ga atoms. The calculated vibration frequencies of the triply boned  $CN_{As}^{2+}$  and  $CN_i^{1+}$  are in reasonable agreement with the measurement by Ulrici and Clerjaud supporting their identification that the bonding is triplebond type. Although neither CN<sub>As</sub> nor CN<sub>i</sub> have the C-N bond oriented along the (100) directions, as proposed by Ulrici and Clerjaud,<sup>21</sup> the low rotation barrier of CN<sub>As</sub> makes it possible that the molecule might be constantly rotating, leading to an average orientation in the  $\langle 100 \rangle$  direction. At higher Fermi levels, the  $CN_i^{1+}$  can accept an electron and becomes  $CN_i^0$ , whereas  $CN_{As}^{2+}$  can accept one, two, three, or four electrons (depending on the Fermi level) and becomes  $CN_{As}^{1+}$ ,  $CN_{As}^{0}$  (metastable),  $CN_{As}^{1-}$ , or  $CN_{As}^{2-}$ , respectively. We found that the C-N bond length and vibrational frequency linearly change (to a good approximation) with the number of electrons added into the antibonding states of the molecule.

# ACKNOWLEDGMENTS

This work was supported in part by the MRSEC Program of the National Science Foundation under Award No.

DMR05-20415, by the NSF IMI Program under Award No. DMR 04-09848, and by the UCSB Solid State Lighting and Display Center. This work also made use of the CNSI Computing Facility under NSF Grant No. CHE-0321368. S.L.

and P.R. thank the Thailand Research Fund (Grants No. BRG5180001 and No. PHD/0203/2546), AOARD/AFOSR (Grant No. FA4869-08-1-4007), and the California NanoSystems Institute for the hospitality.

- <sup>1</sup> K. M. Yu, W. Walukiewicz, J. Wu, D. E. Mars, D. R. Chamberlin, M. A. Scarpulla, O. D. Dubon, and J. F. Geisz, Nat. Mater. 1, 185 (2002).
- <sup>2</sup>W. Shan, W. Walukiewicz, J. W. Ager, E. E. Haller, J. F. Geisz, D. J. Friedman, J. M. Olson, and S. R. Kurtz, Phys. Rev. Lett. **82**, 1221 (1999).
- <sup>3</sup>I. A. Buyanova, M. Izadifard, W. M. Chen, H. P. Xin, and C. W. Tu, Phys. Rev. B **69**, 201303(R) (2004).
- <sup>4</sup>N. Q. Thinh, I. P. Vorona, I. A. Buyanova, W. M. Chen, S. Limpijumnong, S. B. Zhang, Y. G. Hong, C. W. Tu, A. Utsumi, Y. Furukawa, S. Moon, A. Wakahara, and H. Yonezu, Phys. Rev. B **70**, 121201(R) (2004).
- <sup>5</sup>G. Pettinari, F. Masia, A. Polimeni, M. Felici, A. Frova, M. Capizzi, A. Lindsay, E. P. O'Reilly, P. J. Klar, W. Stolz, G. Bais, M. Piccin, S. Rubini, F. Martelli, and A. Franciosi, Phys. Rev. B 74, 245202 (2006).
- <sup>6</sup>G. Pettinari, A. Polimeni, F. Masia, R. Trotta, M. Felici, M. Capizzi, T. Niebling, W. Stolz, and P. J. Klar, Phys. Rev. Lett. **98**, 146402 (2007).
- <sup>7</sup>G. Ciatto, F. Boscherini, A. A. Bonapasta, F. Filippone, A. Polimeni, and M. Capizzi, Phys. Rev. B **71**, 201301(R) (2005).
- <sup>8</sup>P. R. C. Kent and A. Zunger, Phys. Rev. B **64**, 115208 (2001).
- <sup>9</sup>M.-H. Du, S. Limpijumnong, and S. B. Zhang, Phys. Rev. Lett. 97, 075503 (2006).
- <sup>10</sup>M.-H. Du, S. Limpijumnong, and S. B. Zhang, Phys. Rev. B 72, 073202 (2005).
- <sup>11</sup> K. Kim and A. Zunger, Phys. Rev. Lett. **86**, 2609 (2001).
- <sup>12</sup> A. M. Teweldeberhan and S. Fahy, Phys. Rev. B **72**, 195203 (2005).
- <sup>13</sup>A. Amore Bonapasta, F. Filippone, and P. Giannozzi, Phys. Rev. B 68, 115202 (2003).
- <sup>14</sup> A. Janotti, S. B. Zhang, S.-H. Wei, and C. G. Van de Walle, Phys. Rev. Lett. **89**, 086403 (2002).
- <sup>15</sup> X. Li, B. Keyes, S. Asher, S. B. Zhang, S.-H. Wei, T. J. Coutts, S. Limpijumnong, and C. G. Van de Walle, Appl. Phys. Lett. 86, 122107 (2005).
- <sup>16</sup>R. E. Welser, R. S. Setzko, K. S. Stevens, E. M. Rehder, C. R. Lutz, D. S. Hill, and P. J. Zampardi, J. Phys.: Condens. Matter 16, S3373 (2004).
- <sup>17</sup>W. Songprakob, R. Zallen, W. K. Liu, and K. L. Bacher, Phys. Rev. B **62**, 4501 (2000).
- <sup>18</sup> K. H. Tan, S. F. Yoon, Q. F. Huang, R. Zhang, Z. Z. Sun, J. Jiang, W. Feng, and L. H. Lee, Phys. Rev. B **67**, 035208 (2003).
- <sup>19</sup> J. R. L. Fernandez, F. Cerdeira, E. A. Meneses, M. J. S. P. Brasil, J. A. N. T. Soares, A. M. Santos, O. C. Noriega, J. R. Leite, D. J. As, U. Köhler, S. Potthast, and D. G. Pacheco-Salazar, Phys. Rev. B 68, 155204 (2003).
- $^{20}\,B.\text{-H.}$  Cheong and K. J. Chang, Phys. Rev. B  $\,\textbf{49},\,17436$  (1994).
- <sup>21</sup>W. Ulrici and B. Clerjaud, Phys. Rev. B **72**, 045203 (2005).
- <sup>22</sup>S. Limpijumnong, X. N. Li, S. H. Wei, and S. B. Zhang, Appl.

- Phys. Lett. 86, 211910 (2005).
- <sup>23</sup>E.-C. Lee, Y. S. Kim, Y. G. Jin, and K. J. Chang, Phys. Rev. B 64, 085120 (2001).
- <sup>24</sup>P. Fons, H. Tampo, A. V. Kolobov, M. Ohkubo, S. Niki, J. Tominaga, R. Carboni, F. Boscherini, and S. Friedrich, Phys. Rev. Lett. **96**, 045504 (2006).
- <sup>25</sup> A. Janotti and C. G. Van de Walle, Phys. Rev. B **76**, 165202 (2007).
- <sup>26</sup>LDA provides a lattice constant of bulk GaP that is slightly in better agreement with that of experiment. On the other hand, generalized gradient approximation (GGA) provide a slightly better lattice constant for GaAs. Test calculations show that the choice of LDA/GGA only slightly affects the numerical value of energy and vibration frequency but does not change the main conclusions.
- <sup>27</sup>D. Vanderbilt, Phys. Rev. B **41**, 7892 (1990).
- <sup>28</sup>G. Kresse and J. Furthmüller, Comput. Mater. Sci. **6**, 15 (1996).
- <sup>29</sup>S. B. Zhang and J. E. Northrup, Phys. Rev. Lett. **67**, 2339 (1991).
- <sup>30</sup>J. Ashkenazi, Phys. Rev. B **26**, 1512 (1982).
- <sup>31</sup>S. Limpijumnong, J. E. Northrup, and C. G. Van de Walle, Phys. Rev. B **68**, 075206 (2003).
- <sup>32</sup> K. Kim and W. T. King, J. Chem. Phys. **71**, 1967 (1979).
- <sup>33</sup>G. Herzberg, Molecular Spectra and Molecular Structure: Electronic Spectra and Electronic Structure of Polyatomic Molecules (Van Nostrand, New York, 1966).
- <sup>34</sup>H. Jónsson, G. Mills, and K. W. Jacobsen, in *Classical and Quantum Dynamics in Condensed Phase Simulations*, edited by B. J. Berne, G. Ciccotti, and D. F. Coker (World Scientific, Singapore, 1998), p. 385.
- <sup>35</sup>CN<sub>AS</sub> in the +1 and 0 charge states is stable in the symmetric configuration. Test calculations for 1+ showed that a dimer initially tilted by as much as 15° away from the symmetric direction, i.e., the [001] direction, spontaneously rotated back after relaxations. The asymmetric configurations are only metastable. The (higher-energy) metastable asymmetric configuration for each charge state is found by initially aligning the CN molecule along the [110] direction and allowing relaxation of its neighbors before letting the molecule itself relax. The metastable asymmetric configurations are higher in energy than the symmetric ones by 0.1 and 0.5 eV for the 1+ and neutral charge states, respectively. The dimer qualitatively behaves the same in GaP except that none of the metastable asymmetric configurations exists.
- $^{36}$ Although the calculated LDA band gap (at the  $\Gamma$  point) for GaAs is only 0.6 eV, our calculations are performed at special k points wherein the lowest conduction band occurs at 1.08 eV above the VBM. Any defect levels that lie below 1.08 eV are therefore accounted for and can be properly occupied.